Title
Numerical and Experimental Investigation of Bridges with Columns Supported on Rocking Foundations

Author
Antonellis, Grigorios

Publication Date
2015

Peer reviewed|Thesis/dissertation

Numerical and Experimental Investigation of Bridges with Columns Supported on Rocking Foundations

By

Grigorios Antonellis

A dissertation submitted in partial satisfaction of the

requirements for the degree of

Doctor of Philosophy

in

Engineering – Civil and Environmental Engineering

in the

Graduate Division

of the

University of California, Berkeley

Committee in charge:

Professor Marios A. Panagiotou, Chair

Professor Stephen A. Mahin

Professor John Strain

Spring 2015

Abstract

Numerical and Experimental Investigation of Bridges with Columns Supported on Rocking Foundations

by

Grigorios Antonellis

Doctor of Philosophy in Civil and Environmental Engineering

University of California, Berkeley

Professor Marios A. Panagiotou, Chair

The objectives of this dissertation is to investigate the use of rocking foundations in bridges for enhanced seismic design and performance and the reduction of post-earthquake damage. The seismic response of bridge systems was studied numerically using three-dimensional nonlinear models, whereas bridge columns with rocking foundations and superstructure mass were studied both numerically and experimentally. The experimental part consisted of the shake-table testing of large scale bridge columns with shallow rocking foundations using physical modeling of the underlying soil. Using the data from these tests, a three-dimensional model with Winkler springs was modified and validated for rocking shallow foundations designed with high factors of safety against vertical loads. The proposed model was then used on a parametric study to investigate the seismic demand on a large variety of bridge piers with rocking shallow foundations.

The numerical three-dimensional seismic response of six reinforced concrete bridges hypothetically located in Oakland, California, 3 km from the Hayward fault, is presented first. Three of the bridges were 17 m tall and three were 8 m tall. Three types of column-foundation designs were studied: (a) columns that form flexural plastic hinges, which are conventionally designed according to Caltrans seismic design criteria; (b) columns on rocking pile foundations that are designed to remain elastic; and (c) columns designed to remain elastic that are supported on rocking shallow foundations. The bridges with rocking foundations used lead-plug rubber bearings at the abutments to enhance strength, stiffness and hysteretic energy dissipation. Three-dimensional nonlinear response history analyses were performed, using two components of horizontal excitation, for two seismic hazard levels with return periods of 975 and 2475 years, respectively. At both levels of shaking the conventionally designed bridges experienced substantial inelastic deformations and damage in the columns, while the bridges with rocking foundations resulted in essentially elastic response.

The results of a series of shake table tests of two 460-mm-diameter columns supported on 1.5-m-square shallow rocking foundations are presented then. The tests were conducted

using the Large Outdoor High-Performance Shake Table of the Network for Earthquake Engineering Simulation at the University of California at San Diego. The first specimen was aligned with the uniaxial direction of shaking while the second specimen was positioned on a skew configuration. The specimens were placed inside a 10.1-m-long by 4.6-m-wide soil-confining box with 3.4 m height of clean sand compacted at 90% relative density. Three series of tests were performed; each test had different ground water table and backfill conditions. The test protocols included up to six historical ground motions, and resulted in peak drift ratios of up to 13.8%. For peak drift ratios up to 6.9%, the rocking foundations performed very well with residual drift ratios between 0.5% and 0.9%, depending on the backfill conditions, and with minimal settlements and no structural damage.

The next chapter presents a modified numerical modeling scheme for rocking shallow foundations designed with large A/A_c factors. The numerical model is based on traditional Winkler-springs models that use nonlinear vertical springs to represent the soil response beneath the footing. Current models are designed to match both the initial (elastic) vertical and rocking stiffness, and are calibrated using data mainly from centrifuge tests of rocking foundations designed with small A/A_c ratios. The proposed model is designed to match only the secant rocking stiffness at a point where 50% of the foundation moment capacity is mobilized. This stiffness is shown by other researchers to be easily related to the moment capacity of the footing. Additionally, the numerical scheme explicitly models the critical contact area A_c, and the soil capacity on that area so that great accuracy is achieved on the overall foundation moment capacity. The remaining model parameters, such as the capacity and the stiffness of the Winkler springs under the middle section of the footing are calibrated using the data from large scale shake-table tests.

Finally, a parametric three-dimensional seismic analysis of bridge columns supported on rocking shallow foundations is presented. This study uses the modified numerical scheme that was calibrated against the large scale shake-table tests. A total of 44 foundation-column-inertia block units were subjected to two sets of forty ground motions using biaxial horizontal excitation. The first set of ground motions included a broadband set of records which result in mean linear spectral demands similar to those expected at a site 10 km from the fault plane of a magnitude M7 earthquake event. The second set consisted of only near-fault pulse-like records, including the ones with the highest peak ground velocity and spectral demands at "long" periods ever recorded. The parameters under investigation were the column height, H_c, the ratio of bridge column height to foundation length ($1 \leq H_c/B_f \leq 2.8$), the ratio between the "initial" rocking stiffness and the foundation moment capacity (K_{init}/M_r) and the weight of the superstructure (W_s). The absolute nonlinear displacement response as well as the ratio of nonlinear displacement to the linear demand is presented. The conditions that lead to overturn are also discussed. For the pulse-like ground motions, only 12 occasions of overturn were reported. They were only caused by the TCU068 and TCU065 records and for models with C_r values less than 0.17. For the pulse-like motions the nonlinear displacement ratio, r_N, increases rapidly with decrease of the first period, $T_{1,s}$, for $T_{1,s} < 0.75$ s. For the near-fault motions,

the demand as well as the number of overturns was related well with pulse energy and pulse area. No overturn was computed for the broadband set of ground motions.

To my parents and my beautiful wife, Ishita

Table of contents

List of figures

List of tables

Acknowledgments

First and foremost I want to thank my advisor Professor Marios Panagiotou for his guidance and support during the past six years. It was through his persistence and funded research opportunity that I was able to pursue my graduate studies at UC Berkeley. His vision and determination also gave me the opportunity to work on an exciting experimental project on the largest shake table laboratory in USA, a dream come true for any aspiring structural engineer. His accessibility and hard work inspired me to push forward all these years and I am looking forward to our continued collaboration in the future.

I am also very grateful to the members of my thesis committee, Professor Stephen A. Mahin and Professor John Strain. Professor Mahin, through his graduate course, increased my passion for earthquake engineering and inspired me to look at the problems from different perspectives. He was also very supportive and informative during my academic job hunt and I am grateful for his help all these years. The graduate course on advanced matrix calculations (Math 221) by Professor Strain was one of the best courses I attended at UC Berkeley. His unique lecturing style and his humor during the office hours balanced out the countless hours spent working on his challenging assignments.

During my involvement in the experimental investigation of bridge columns with rocking foundations I had the opportunity to work closely with Professor Bruce L. Kutter, Jose I. Restrepo and Patrick J. Fox. I am thankful to all of them for their guidance and support over the past two years. I am also grateful to Professor Ioannis Koutromanos who helped me out with various practical issues regarding the numerical modeling in OpenSees.

This thesis would not have been possible without the financial support from the Transportation Research Program of the Pacific Earthquake Engineering Research Center and the California Department of Transportation (Caltrans). I would like to thank especially Thomas Shantz, Fadel Alameddine, and Mark Desalvatore from Caltrans for their constructive comments all these years. I am also thankful to the “Triantafyllidis” Institution, the “A. Mentzelopoulos” foundation and the “Gerondelis” foundation for providing partial financial support throughout my graduate studies.

The shake table tests were completed in a timely manner due to the hard work of the staff at the NEES lab at UCSD Dan Radulescu, Paul Greco, Alex Sherman, Hector Vicencio, Raymond Hughey, Robert Beckley, Lawton Rodriguez and Darren McKay. I am also very grateful to Andreas G. Gavras, Gabriele Guerrini and Andrew Sander for their personal effort, time and sweat during the construction of the test specimens and experimental setup at UCSD. Their contribution was instrumental to the successful completion of the test. I feel especially lucky that my collaboration with Andreas has continued over the past two years and I am still amazed at his talent and deep understanding of soil mechanics.

My life inside and outside Davis Hall with the windowless offices was brightened by the numerous friends and colleagues I met at Berkeley. I especially want to thank Pano, Eleni, Dimitri, Marco, Ahmet, Tea, Yuan, Mohammed, Simon, Houfu, Niko, Michali, Konstantino (x2), Candice and Thodori.

Finally, I cannot be thankful enough to my parents, Aggelos and Vasiliki, for their sacrifice and support all these years. The phone calls to them and to my siblings, Pano, Yanni, Dimitri, Christina and Eleni, made my life far from home significantly easier. Last but not least, I want to thank my beautiful wife Ishita for her continuous support all these years, and I am looking forward to the next chapter of our life together!

Chapter 1: Introduction

1.1 Studies on Rocking Foundations

1.1.1 Analytical and numerical studies

Traditional design of fixed-base bridges includes ductile details that permit bridges to develop the substantial inelastic deformations expected when subjected to severe earthquakes. While bridges designed in this manner may be safe from collapse, they are susceptible to considerable damage and permanent lateral displacements that can impair traffic flow and necessitate costly, time consuming, dangerous, and disruptive inspections and repairs (and perhaps even demolition). As an alternative design, bridges with columns supported on foundations allowed to uplift can undergo large deformations but suffer far less damage, with the added bonus of re-centering following large earthquakes. Compared to fixed-base bridges, bridges supported on rocking foundations may have additional economic benefit because fixed-base bridges require larger spread foundations as well as larger and/or more piles.

The rocking behavior of structures has been investigated numerically and experimentally since the nineteenth century (Milne and Omori 1893) and early in the twentieth century by Kirkpatrick (1927). For forty years rocking of structures has been considered an effective mechanism of resisting lateral forces and developing deformations expected during earthquake excitation. In 1960 Muto et al. studied numerically the overturning vibration of slender structures, while in 1963 Housner studied numerically the rocking behavior of rigid blocks supported on a rigid base subjected to sinusoidal excitation. Beck and Skinner (1974) studied the rocking response of a step bridge pier, a system later used in the design of the South Rangitikei Railway Bridge, New Zealand, constructed in 1981. Rocking of structures was extensively studied thereafter, both numerically and experimentally. The rocking behavior of rigid blocks on a rigid base has been studied considering harmonic (Spanos and Koh 1984; Tso and Wong 1989), broadband (Ishiyama 1983), and pulse-type ground excitations (Makris and Roussos 2000; Makris and Zhang 2001; Makris and Konstantinidis 2003). Other studies have considered the rocking response of rigid blocks on elastic (Psycharis and Jennings 1983) and inelastic bases (Apostolou et al. 2007). The rocking response of flexible structures supported on rigid (Meek 1978; Chopra and Yim 1985), flexible (Chopra and Yim 1985), and inelastic bases (Apostolou et al. 2007) has also been studied. Finally, Cremer et al. (2001, 2002) studied numerically the nonlinear two-dimensional (2D) response of rocking shallow foundations. Foundation rocking has been numerically identified as a mechanism that may explain why some engineered structures did not suffer as severe damage during earthquakes (Rutenberg et al. 1982). In contrast, overturning of equipment or structures due to rocking during earthquakes has also been reported (Anooshehpoor et al. 1999; Shi et al. 1996).

Rocking foundations have been utilized in the design of major bridges like the Rion Antirion Bridge, Greece (Pecker 2006), and the retrofit of bridges, like the Golden Gate Bridge, San Francisco, California, (Ingham et al. 1995), the Carquinez Bridge, Vallejo,

California (Jones et al. 1997) and the Lions Gate Bridge, Vancouver, British Columbia (Dowdell and Hamersley 2000). They have also been proposed in as a retrofit scheme (Astaneh et al. 1993).

1.1.2 Experimental studies on rocking foundations

The experimental response of rocking structures has been investigated as follows: (i) shake-table tests of structures supported on rigid or flexible bases; (ii) large-scale static cyclic tests of foundations or simple structures in large soil-boxes; and (iii) centrifuge tests.

Shaking table tests of buildings using rocking foundations supported on a rigid base (Kelly and Tsztoo 1977; Clough and Huckelbridge 1977) and simple single-mass structures supported on a rigid or flexible base (Priestley et al. 1978) were first conducted in the 1970s. Shake table tests with either of single bridge columns or two-column subassemblies supported on rocking foundations (Saidi et al. 2002; Chen et al. 2006; Sakellaraki and Kawashima 2006; Espinoza and Mahin 2008) were conducted thereafter. Large-scale experimental studies involving geotechnical aspects of rocking of shallow foundations have also been performed (Bartlett 1976; Wiessing 1979; Georgiadis and Butterfield 1988; Pecker and Pender 2000; Faccioli et al. 2001; Paolucci et al. 2007).

Numerous centrifuge tests of simple piers supported on rocking shallow foundations (Kutter et al. 2006; Gajan et al. 2008; Ugalde et al. 2010) and rocking pile-foundations (Deng and Kutter 2012) as well as of simple bridge models (Deng et al. 2012a) with columns supported on rocking foundations have been conducted. The latter study considered model columns with different heights, footing widths, and skews relative to the axis of shaking.

1.2 Thesis Outline

This thesis consists of five additional chapters, excluding this introduction.

Chapter 2 presents a three-dimensional numerical study on the seismic response of bridge systems with columns supported on rocking foundations, compared to traditionally designed bridges with "fixed-base" columns. Two different designs of rocking foundations are investigated, a rocking shallow foundation and a rocking pile cap foundation. This numerical study demonstrates the efficacy of rocking foundations, along with other structural details, into minimizing the post-earthquake damage even after strong ground shaking.

Chapter 3 describes a large scale shake-table study of bridge columns with rocking shallow foundations which was performed at the NEES facility at UC San Diego. This study, which was funded by Caltrans, involved two specimens, one placed on an aligned and a second on a skewed configuration with respect to the direction of loading. Three different tests were performed with varying underground water elevations and foundation backfill conditions. This study showed the effect of the backfill conditions into the overall response of the rocking foundations. When the surrounding of the rocking shallow foundations are specially detailed, the rocking systems can experience large peak drift ratios with minimal residual drifts and settlements and no structural damage.

Using the collected data from the experimental tests, a modified numerical modeling scheme is proposed on Chapter 4. This scheme utilizes the commonly used QzSimple1 Winkler springs to model the behavior of the soil beneath the footing with distributed strength and stiffness calibrated to capture the foundation moment rotation and settlement characteristics of rocking shallow foundations designed with high factors of safety.

The improved modeling scheme is then used on a parametric numerical study of bridge columns with rocking foundations which is presented on Chapter 5. The purpose of this study

is to identify the structural and ground motion characteristics which trigger instability (overturn). Additionally, a three-dimensional demand model, in terms of nonlinear response ratio, is also developed for these columns.

Finally, Chapter 6 summarizes the conclusions of this thesis and presents some recommendations for future research.

Chapter 2: Numerical Analyses of Bridges with Rocking Foundations at a Near-Fault Site

2.1 Introduction

Conventionally designed bridges rely on the concept of ductility, whereby the column reinforcement is detailed to ensure the development of flexural plastic hinges at the base and the top of the columns. While bridges designed in this manner may be safe from collapse, they are susceptible to considerable damage and permanent lateral displacements that can impair traffic flow and necessitate costly, time consuming, dangerous, and disruptive inspections and repairs. As an alternative design, bridges with columns supported on rocking foundations may develop large nonlinear deformations when subjected to strong shaking but experience far less damage in the columns, with the added bonus of these columns that re-center following a high-intensity earthquake ground motion.

The rocking behavior of structures has been investigated numerically and experimentally since the nineteenth century (Milne and Omori 1893). In 1960 Muto et al. studied the rocking response of slender structures both numerically and through shake table tests, while in 1963 Housner studied numerically the rocking behavior of rigid blocks supported on a rigid base and subjected to ground excitation. Beck and Skinner (1974) conducted the first analytical study to investigate the use of a rocking step pier as an earthquake-resistant structural system for bridges. This system was later used in the design and construction of the South Rangitikei Railway Bridge, New Zealand (Cormack 1988). Rocking foundations or rocking piers have been utilized in the design (Pecker 2006) and retrofit (Astaneh-Asl and Roberts 1996) of other major bridges or have been proposed for the design and retrofit of bridges (Priestley et al. 1978 and 1996, Pollino and Bruneau 2007).

Over the last four decades, a number of numerical studies of the seismic response of rocking structures have been conducted, including: (1) seismic soil-structure interaction of foundations that uplift (Wolf 1976); (2) rocking flexible structures supported on a flexible base (Chopra and Yim 1985); (3) rigid blocks on a rigid base subjected to pulse-type ground excitation (Makris and Zhang 2001); and, rigid blocks on an inelastic base (Apostolou et al. 2007).

Extensive studies on the numerical investigation of the seismic response of single bridge piers supported on rocking foundations have also been performed, including three-dimensional (3D) (Mergos and Kawashima 2005) and two-dimensional (Deng et al. 2012) response history analysis and use of nonlinear-Winkler-foundation models. Sakellaraki and Kawashima (2006) studied the 3D response of a bridge with columns supported on rocking shallow foundations. This study used a 3D model with fiber section nonlinear beam elements for the columns, nonlinear Winkler-type model for the shallow foundations, elastic beam elements for the deck, and springs modeling the behavior of the abutments in the longitudinal direction. In that study a single near-fault ground motion record was used in the 3D analysis of the bridge models.

Some of the first experimental shake table studies of rocking buildings (Kelly and Tsztoo 1977) and of single rocking piers (Priestley et al. 1978) were conducted in the 1970s. Extensive experimental studies of the rocking response of single bridge columns or two-column subassemblies supported on rocking shallow foundations followed, with shake table tests performed by Saiidi et al. (2002), Chen et al. (2006), and Espinoza and Mahin (2008). Large-scale experimental studies involving geotechnical aspects of rocking of shallow foundations with static loading (Bartlett 1976; Wiessing 1979; Negro et al. 2000, Paolucci et al. 2007) or dynamic (Paolucci et al. 2007) have also been performed. Finally, numerous centrifuge tests of rocking structures including that of single piers and simple bridge models with columns supported on rocking shallow foundations (Gajan et al. 2005, Deng et al. 2012a) and piers supported on rocking pile-foundations (Pecker 2006, Allmond and Kutter 2012) have been performed.

This study investigates the 3D seismic response of bridges with columns supported on rocking foundations and compares their response to that of conventional bridges of similar geometry designed according to current Caltrans Seismic Design Criteria (SDC) (Caltrans 2010). Both rocking shallow foundations and rocking pile foundations are studied. The bridges with rocking foundations use larger diameter lead-plug rubber bearings at the abutments to enhance strength, stiffness, and hysteretic energy dissipation compared to the laminated (no lead-plug) rubber bearings used in the fixed-base bridges. All bridges are located 3 km from the Hayward fault in Oakland, California. Three-dimensional numerical models of the bridges including the foundations, the columns, the deck, and the abutments were developed and subjected to bi-axial horizontal excitation using a set of 14 ground motions scaled to two different seismic hazard levels, with return period equal to 975 and 2475 years, respectively.

2.2 Site and Seismic Hazard Description

The bridges in this study are hypothetically located at the intersection of the I-580 and Highway 24, in Oakland, California, 3 km from the Hayward fault, in a site with an average shear wave velocity V_s = 400 m / s in the top 30 m of soil. The site seismic hazard and corresponding design spectra were determined (USGS 2013) for two hazard levels: (a) 5% probability of exceedance in 50 years (975-year return period); and (b) 2% probability of exceedance in 50 years (2475-year return period), corresponding to the design earthquake (DE) and maximum considered earthquake (MCE), respectively. Figure 2.1 shows the design acceleration and displacement spectra at the two seismic hazard levels. Bi-axial horizontal excitation and one set of 14 historical near-fault pulse-like ground motions were used in this 3D numerical study, see Table 2.1. For each ground motion the fault-normal (FN) and fault-parallel (FP) horizontal component of the original record was used. The vertical component of the ground motions is not used here. The ground motions were linearly scaled such that the average spectrum of the fault-normal components for 5% damping ratio, ζ, matched (approximately) the design spectra at the corresponding hazard level. The corresponding scale factors for each motion are shown in Table 2.1. For each of the 14 ground motions the same scale factor was applied in the fault-normal and fault-parallel component. The mean acceleration and displacement spectra of the fault-normal components are shown in Figure 2.1(a), and (b) respectively. The corresponding spectra of the fault-parallel components scaled to the DE are also shown in this figure.

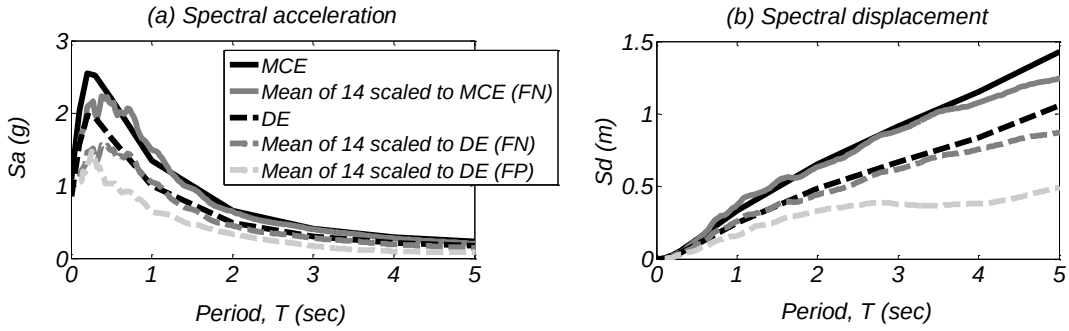

Figure 2.1. Design linear acceleration and displacement spectra for the DE and MCE seismic hazard levels compared to the corresponding mean spectra at 5% damping ratio, of the 14 ground motions scaled at the corresponding hazard level.

Table 2.1. Set of the fourteen ground motions and their individual scale factors for the DE and MCE level.

No.	Record	Earthquake name, Location, Year	Scale factors	
			DE	MCE
1	LGPC	Loma Prieta, CA, 1989	1.11	1.58
2	RRS	Northridge, CA, 1994	1.06	1.52
3	TCU052	Chi-Chi, Taiwan, 1999	0.70	1.00
4	PACOIMA DAM	San Fernando, CA, 1971	1.41	2.02
5	NEWHALL	Northridge, CA, 1994	1.31	1.87
6	TABAS	Tabas, Iran, 1978	0.87	1.24
7	DUZCE	Duzce, Turkey, 1999	0.82	1.17
8	ELCEN6	Imperial Valley, CA, 1979	0.42	0.60
9	LUCERNE	Landers, CA, 1992	0.74	1.06
10	TCU074	Chi-Chi, Taiwan, 1999	1.09	1.55
11	CHY028	Chi-Chi, Taiwan, 1999	1.31	1.87
12	SCS	Northridge, CA, 1994	1.10	1.57
13	ELCEN DIFF	Imperial Valley, CA, 1979	0.92	1.32
14	TCU079	Chi-Chi, Taiwan, 1999	1.10	1.57

2.3 Description and Design of the Bridges

Figure 2.2(a) shows a side view of the bridges while Table 2.2 summarizes the main characteristics. All six bridges had five spans, single column bents, and the deck section shown in Figure 2.2(b). The height of the bridges, *H*, is defined as the distance from the ground surface to the top of the deck; see Figure 2.2(a) and (b). Three designs were investigated in terms of foundation-column design: (1) columns supported on fixed pile foundations and designed to form flexural plastic hinges at their ends (according to Caltrans

SDC), referred to herein as fixed-base (FB); (2) columns designed to remain elastic and supported on rocking pile foundations with the pile caps designed to uplift in respect to the piles, referred to herein as rocking pile foundation (RPF); and (3) columns designed to remain elastic supported on shallow foundations designed to uplift with respect to the soil, referred to herein as rocking shallow foundation (RSF). Bridges FB17, RPF17, and RSF17 were 16.5 m tall and bridges FB8, RPF8, and RSF8 were 8 m-tall. The three different designs are discussed in the following three sections. The number after the design description FB, RSF, and RPF refers to the bridge height.

The area of the deck section for all bridges is 6 m^2 and is post-tensioned, with high-strength low-relaxation Grade 270 (ultimate strength $f_{ps,u}$ =1860 MPa) tendons. In all bridges the total area of strands used is A_{ps} = 31080 mm^2 and the initial after losses post-tensioning stress of the strands $f_{ps,i}$ = 1000 MPa (initial strain of strands after losses $\varepsilon_{ps,i}$ = 0.56%). The losses were assumed to be constant along the deck. The deck section has a longitudinal bonded steel ratio of 0.4%. All reinforced concrete components of the six bridges are designed with concrete to a specified compressive strength f_c' = 41 MPa and steel with a specified yield strength of f_y = 413 MPa. The seismic weights, *W*, given in Table 2.2 include 3.1 MN live load and three quarters of the weight of the columns.

For the FB bridges the deck at the abutments is supported on two 0.6 m diameter laminated rubber bearings [see Table 2.2 and Figure 2.2(c)], consisting of seventeen 12 mm thick rubber layers, with a shear modulus of rubber G_r = 0.6 MPa. For the bridges with rocking foundations the deck at the abutments is supported on two circular laminated 1.26 m diameter lead-plug rubber bearings (LPRB), consisting of twenty six 12 mm thick rubber layers with G_r = 0.6 MPa, and a 340 mm lead-plug with shear modulus of lead G_L = 150 MPa and yield stress of lead τ_L = 10 MPa. The shear keys of the abutments in the transverse direction are the same for all six bridges and designed to have a lateral strength of 660 kN. The expansion joints at the abutments are identical for all six bridges and have a deformation capacity of 0.10 m; see Figure 2.2(d). The next three sections describe each of the column-foundation designs.

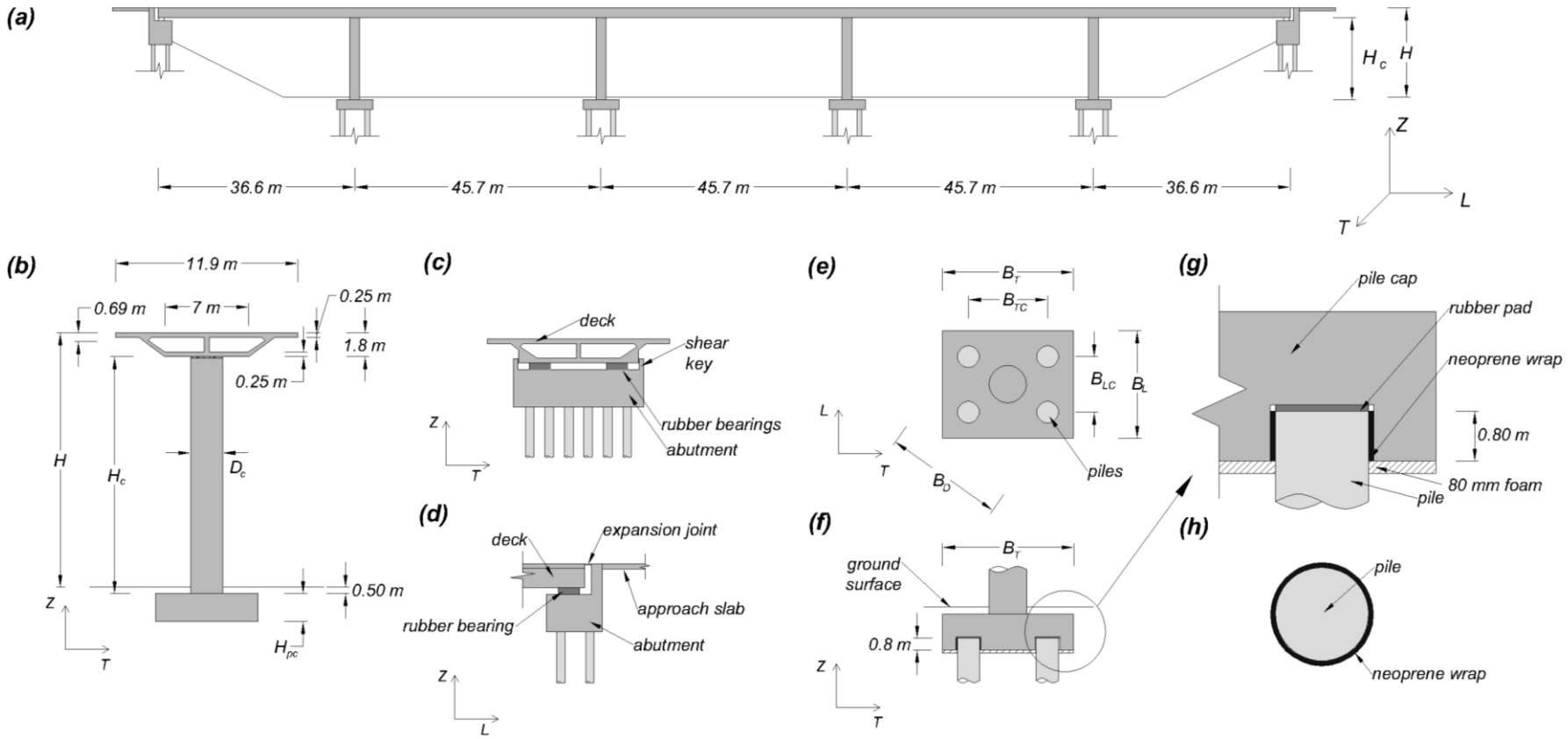

Figure 2.2. Geometric characteristics of the bridges: (a) side view of the whole bridge; (b) elevation view of the foundation-column and deck of bridge RSF17; (c) elevation section view of abutment, bearings, and deck of the bridges; (d) side elevation view of abutment, bearing, deck and expansion joint of all bridges; (e) plan view of the pile foundations; (f) elevation section view of the rocking pile foundations; (g) elevation section view of pile cap to pile connection of the rocking pile foundations; and (h) section view of pile and neoprene wrap of the rocking pile-foundations.

Table 2.2. Main characteristics of the six bridges.

	Bridge name	FB17	FB8	RPF17	RPF8	RSF17	RSF8
	Type of foundation	Fixed pile foundation		Rocking pile foundation		Rocking shallow foundation	
	Seismic weight above ground, W (MN)	47.7	46.1	50.2	47.2	50.2	47.2
Foundation	Height of pile cap or of shallow found., H_{pc} (m)	2.0		2.4	2.4	2.0	
	Width B_T (m) / B_{TC} (m)	7.0 / 3.8		8.8 / 5.3	8.5 / 5.0	8.0	
	Length B_L (m) / B_{LC} (m)	7.0 / 3.8		7.2 / 3.7	7.0 / 3.5	8.0	
	Number of piles	4		4		N/A	
	Pile diameter (m) / Pile length (m)	1.5 / 20		1.5 / 25		N/A	
Column	Height, H_c (m)	15.2	6.7	15.2	6.7	15.2	6.7
	Diameter, D_c (m)	1.8	1.8	2.5	2.5	2.5	2.5
	Base axial force interior col., (MN)	10.6	10.3	11.1	10.4	11.2	10.4
	Long. reinforcing steel ratio, ρ_l (%)	2	2	3	3	3	3
	Connection with deck	Fixed	Fixed	Pin	Pin	Pin	Pin
Bearing	Diameter (m)	0.6		1.26			
	Total height of rubber, t_r (mm)	200		312			
	Diameter of lead plug (m)	N/A		0.34			

2.3.1 Fixed-base (FB) bridges

In general, the majority of inelastic deformations in these bridges are expected to develop in flexural plastic hinges near the two ends of the columns, especially near the base. For the FB bridges the columns were designed to be fixed at both ends. Figure 2.3 shows the expected deformation pattern of the FB bridges responding in the transverse direction. These bridges are designed based on the Caltrans SDC (2010). The column diameter for bridges FB17 and FB8 is 1.8 m and have longitudinal steel ratio ρ_l = 2%. Based on the moment-curvature section analysis using expected material properties (described in Numerical Model section), the flexural strength of the columns at 1%, and 5% tensile strain of the longitudinal reinforcement and for axial compression force equal to 10.6 MN was computed equal to 24.8 MN-m, and 28.1 MN-m, respectively. The FB bridges use a pile-foundation for the columns with a 7 m square and 2 m deep pile cap fixed to 4 RC piles, each pile being 1.5 m in diameter and 20 m long.

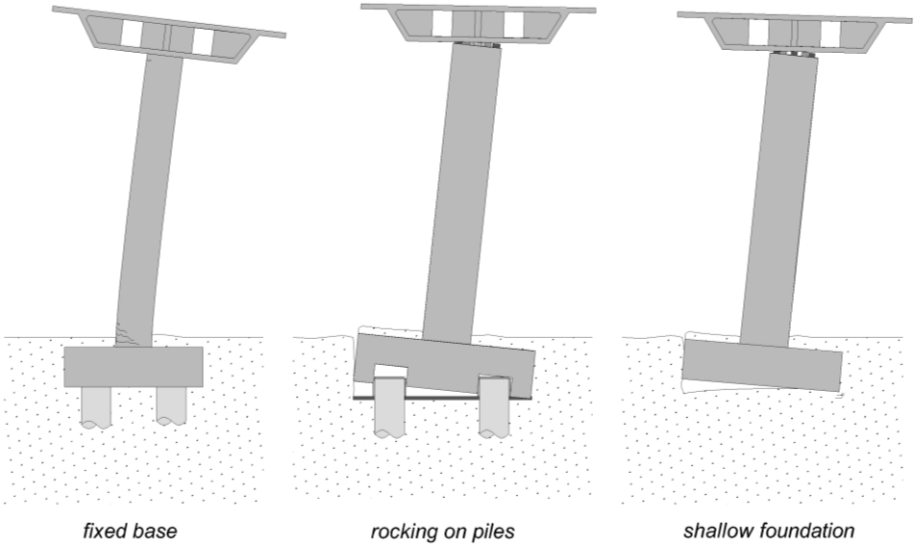

Figure 2.3. Schematic of foundation, column and deck in a deformed state at a 5% transverse drift ratio for the three designs studied (displacements are drawn magnified by 2).

2.3.2 Bridges with rocking pile foundations (RPF)

The majority of deformations in the bridges with a RPF are due to rocking of the pile cap with respect to the piles, see Figure 2.3; the deck, columns, pile cap, and piles are designed to remain nominally elastic at the MCE level of shaking without exceeding 5% drift ratio and 0.5% residual drift ratio; This design can be used in lieu of a RSF design because the soil properties near the ground surface are such that they cannot achieve the above design objectives.

In the RPF design the rectangular pile cap is simply seated on top of four 1.5 m diameter RC piles, which protrude into the pile cap [see Figure 2.2(e), (f) and (g)], and is practically free to rotate with respect to the piles. Each pile has 1.5% longitudinal steel ratio. The connection between the piles and the pile cap is described later in this section. This design uses a pin connection between the columns and the deck to prevent the formation of a flexural plastic hinge at the top of the column. To achieve similar level of displacements comparable to the FB bridge, the RPF design must incorporate a significant increase of the design strength because the RPF design results in significantly smaller hysteretic energy dissipation than that of the FB bridge. Furthermore, the use of pin connections between the columns and the deck used in the RPF designs reduce the stiffness and strength of the bridge compared to the FB design, especially in the longitudinal direction. Additional strength and stiffness was achieved using larger foundations and columns as well as stiffer and stronger bearings at the abutments. Hysteretic energy dissipation was provided by using LPRBs in the abutments.

In this design the columns are designed to remain elastic for the maximum moment resistance of the foundation at the top of the piles. This resistance can be approximated to be equal to $W_{tot}B_D/2$, where W_{tot} is the vertical force at the top of the piles and B_D the distance between the outer face of the two piles along the diagonal [see Figure 2.2(e)]. The bending moment resistance due to friction between the vertical sides of the pile-cap

and the soil was ignored. The pile cap is 8.8 m × 7.2 m × 2.4 m and 8.5 m × 7.0 m × 2.4 m for the RPF17 and RPF8 bridges, respectively. The piles—1.5 m in diameter and 25 m long—protrude 0.8 m into the pile cap, see Figure 2.2(f) and (g).

The protruding part of the piles into the pile cap is wrapped with a 60 mm thick neoprene sheet with shear modulus of neoprene used here G_n = 0.03 MPa. The pile cap seats on the piles without any tension force transfer connection other than the shear force that can be transferred from the pile cap to the neoprene wrap. A 30 mm thick 1.5 m diameter rubber pad with G_r = 0.6 MPa is used between the top of the piles and the pile cap, see Figure 2.2(g) and (h). Neoprene wraps are used to achieve a smoother contact and normal force transfer between the pile cap and the piles while allowing nearly free uplift and rotation of the pile cap. The rubber pads at the top of the piles are used in order to achieve small horizontal displacements of the pile cap in respect to the piles and help engage all four piles in shear. Both the neoprene wraps and the rubber pads are glued to the piles. In addition, an 80 mm-thick foam layer is used at the base of the pile cap to prevent unintended overstrength due to vertical resistance of the soil underneath the pile cap.

Each pile is designed to resist the entire gravity force the pile cap caries by utilizing the shaft resistance, Q_s, of the pile and about 20% of base resistance, Q_b. For sand with representative angle of friction $\varphi' = 39^o$ and the pile geometry used here, Q_s = 6.6 MN and Q_b = 39 MN (Fleming et al. 2009). The water table was assumed to be 11 m below the ground surface. Based on lateral capacity analysis (Fleming et al. 2009), each pile for zero and 14.5 MN axial load can resist 2.5 MN and 2.8 MN of lateral force, respectively. The lateral capacity was calculated at the point where the longitudinal tension strain in the pile reaches 0.5%. The column in the RPF bridges was 2.5 m in diameter with 3% longitudinal steel ratio along the entire column height. For 11.1 MN axial load, the nominal flexural strength of the column was computed based on moment curvature section analysis equal to 54 MN-m.

2.3.3 Bridges with rocking shallow foundations (RSF)

The soil near the ground surface for bridges RSF17 and RSF8 is assumed to have $\varphi' = 37^o$ and specific weight γ = 18.6 kN / m^3. The response objectives in this case were identical to those for the RPF designs. The length and the depth of the square footings are equal to 8.0 m and 2.0 m, respectively, for both RSF17 and RSF8 bridges, while the embedment depth is 0.5 m. For these soil properties and geometry of the footings and 13.9 MN vertical force the bearing stress capacity is q_{bl} = 2.6 MPa (Meyerhof 1963), resulting in a vertical force factor of safety FS_v = 12. The maximum moment capacity of the footing is calculated to be M_{max} = 52 MN-m; the corresponding length of the contact area between the soil and the footing at M_{max} is $0.17B_T$. The columns of bridges RSF17 and RSF8 are identical to those of bridges RPF17 and RPF8, respectively.

2.4 Numerical Model

The analyses were conducted using the Open System for Earthquake Engineering Simulation (OpenSees, 2012) computer software. Figure 2.4(a) shows the 3D model. Nonlinear fiber-section Euler Bernoulli beam-column elements were used to model the

columns and the deck. For each of the columns, two beam elements of equal length were used, with 5 and 4 integration points each for the 17 m and 8 m tall bridges, respectively. Two beam elements, with three integration points each, modeled each span of the deck. The material models Concrete03 and Steel02 were used to model the concrete and reinforcing steel, respectively, in each of the nonlinear beam-column elements. Expected values of material properties were used. The expected compressive strength of the concrete used was $f_{c,e}$ = 62 MPa, and the yield stress of the steel was f_y = 455 MPa with a 2% hardening ratio. The expected compressive strength of the confined concrete of the columns was $f_{cc,e}$ = 80 MPa. The initial post-tensioning force of the deck was modeled using the initial strain material. The strands were modeled with fibers having the Steel02 material behavior and yield strength $f_{ps,y}$ = 1670 MPa. Linear elastic stiff elements connected the top and bottom of the columns with the centroid of the deck and the foundation centroid, respectively, as well as the centroid of the foundation to the bottom of the foundation, see Figure 2.4(b). At the interface of column with the top of the foundation and the base of the deck, a zero-length-section element modeled the strain penetration of the longitudinal reinforcement of the column in the foundation and the deck, respectively. The sections of these zero-length elements were identical to these of the beam elements of the columns and used the same materials, but the tangent modulus of the materials was 17 times smaller. The P-Δ geometric transformation was used for all the beam elements. The columns of the FB bridges were modeled as fixed at their base.

Spring elements modeled the rubber bearings at the abutments. For each bearing, two horizontal springs (one in the longitudinal and another in the transverse direction) and one vertical spring were used. The rubber bearings of the FB bridges were modeled as linear in the horizontal directions with stiffness K_h = 0.85 MN /m. In the vertical direction, the bearings were modeled to have a linear behavior with stiffness $K_{v,c}$ = 795 MN/m, and $K_{v,t}$ = 79.5 MN/m in compression and tension, respectively. The LPRBs were modeled to have a bilinear force-displacement (F-Δ) relation with initial stiffness of 30.8 MN / m, post-yield stiffness equal to 2.4 MN/m, and a yield force equal to 0.9 MN. For these bearings $K_{v,c}$ = 8750 MN/m and $K_{v,t}$ = 875 MN/m.

The combined behavior of the expansion joint, the abutment wall and the backfill soil were modeled in the longitudinal direction using a spring with zero tensile strength and a bi-linear behavior with gap in compression [see Figure 2.5(a)]. The shear keys were modeled using spring elements in the transverse direction with the tri-linear force-displacement relationship shown in Figure 2.5(b).

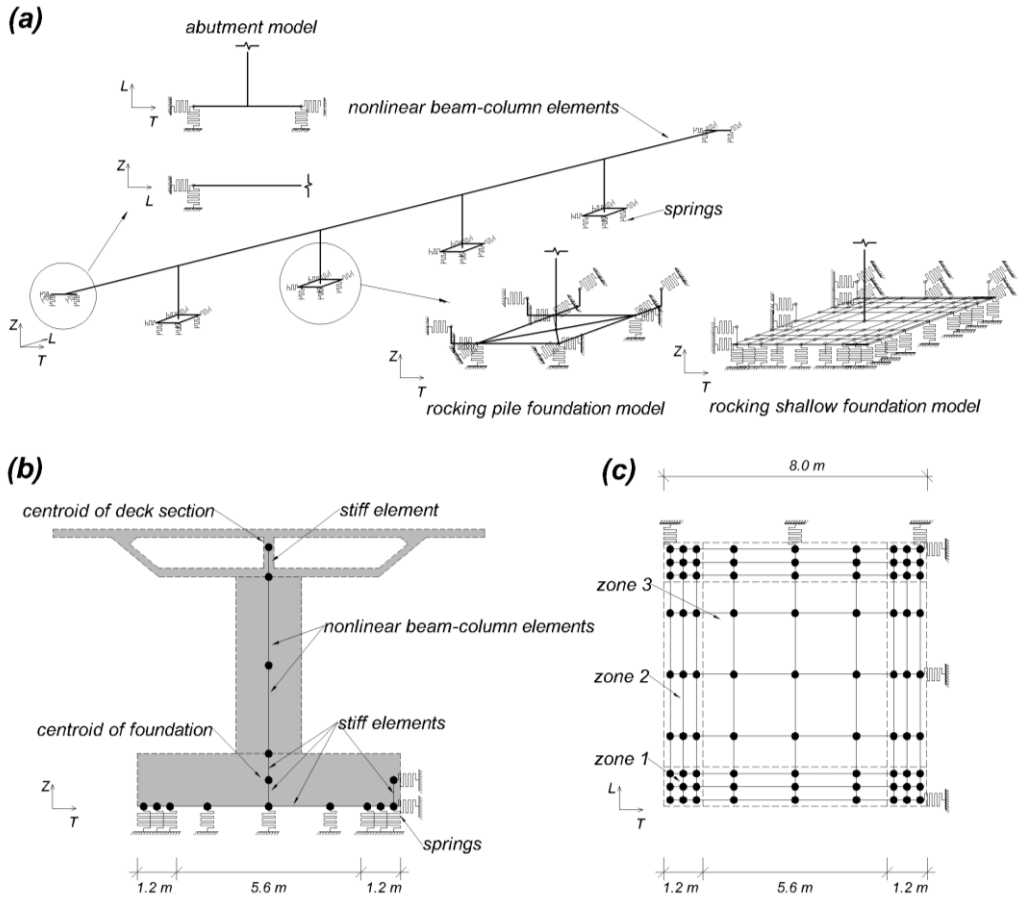

Figure 2.4. Schematic of the numerical model: (a) three dimensional view; (b) elevation section view of the foundation, column and deck of bridge RSF8; and (c) plan view of the model of the rocking shallow foundations.

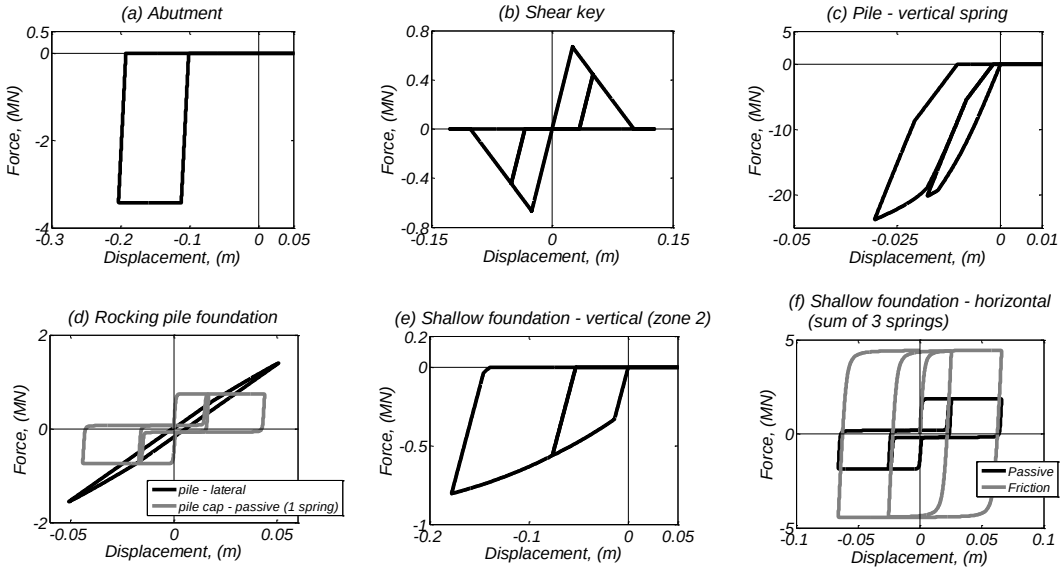

Figure 2.5. Force-displacement relations of the different springs used in the bridge models for different components.

The behavior of each pile of the rocking pile foundations in the vertical direction was modeled using a spring located at the centroid of the pile. This spring had zero tensile strength and the nonlinear F-Δ behavior shown in Figure 2.5(c), the result of using in parallel *QzSimple1* the *TzSimple1* materials (OpenSees, 2012) to model the bearing and shaft behavior, respectively, of the pile. Springs having the *PySimple1* nonlinear F-Δ relation shown in Figure 2.5(d) were used to model the lateral F-Δ behavior of each pile. The passive pressure from the soil to the sides of the pile cap was modeled with two springs, see Figure 2.4(a), in each of the longitudinal and transverse direction, with the nonlinear *PySimple1* F-Δ relation shown in Figure 2.5(d). The friction between the four vertical sides of the pile cap and the soil was ignored in the model. The neoprene wraps around the top of the piles as well as the rubber pads at the top of the piles were also not modeled.

The soil underneath each shallow foundation was modeled using 81 springs; see Figure 2.4(b) and (c). The vertical force-displacement relation was modeled using the *QzSimple1*-type 2 *F-Δ* relation shown in Figure 2.5(e). In terms of *F-Δ* relation of these springs, three zones were distinguished [see Figure 2.4(c)]. The control parameters of the *F-Δ* relation for these springs in each of the three zones are listed in Table 2.3 as follows: (a) the area each spring represents; (b) the ultimate soil stress, q_u; and (c) the secant stiffness, K_z, at 50% of ultimate force of the spring. The q_u of the springs of zones 1 and 2 is determined accounting for the contact area between the foundation and the soil (Meyerhof 1963) at maximum moment resistance of the foundation. The K_z was determined according to the recommendations of Harden and Hutchinson (2009). The passive resistance of the soil on the vertical sides of the foundation was modeled using three springs, in each of the longitudinal and transverse directions, see Figure 2.4(a) and (c), having the *PySimple1* F-Δ relation shown in Figure 2.5(f). The friction resistance at the base of the shallow foundation was modeled using three springs, in each of the longitudinal and transverse directions, having the *Tzsimple1* nonlinear F-Δ relation [see Figure 2.5(f)]. For both the shallow foundations and the pile caps a grid of linear stiff beam elements modeled the perimeter and connected it with the centroid. For all six bridge models studied, aspects of the soil-foundation-superstructure interaction—such as radiation damping as well as the response of the soil beyond that in the immediate vicinity of the shallow foundations—were ignored.

Translational and rotatory masses were lumped at the nodes of the deck, the nodes at the mid-height of the columns, and the nodes at the centroid of the foundations. Uniformly distributed gravity forces were assigned along the deck. Point gravity forces were assigned at the middle and base of the columns and the centroid of the foundations. Mass and initial stiffness proportionate Rayleigh damping was used with 2% damping ratio in the following two modes: the first mode with the predominant translational component in the transverse direction and the first mode with the predominant translational component in the longitudinal direction.

Table 2.3. Main characteristics springs modeling the soil beneath the shallow foundations. Zones 1 to 3 are shown in Figure 2.4(c).

	Area (m^2)	Ultimate stress, q_{bl}, (MPa)	Secant stiffness per unit area at 50% of ultimate stress, K_z, ($MN/m/m^2$)
Zone 1 (end-end)	0.16	1.47	11.6
Zone 2 (mid-end)	0.75	1.47	11.5
Zone 3 (mid-mid)	3.48	2.59	0.27

2.5 Analysis Results

2.5.1 Modal analysis and monotonic static analysis results

Table 2.4 shows the two modal periods of the six bridges with the most predominant translational component in the transverse ($T_{1,T}$) and longitudinal ($T_{1,L}$) direction, respectively, computed using initial stiffness properties for all the elements. Figure 2.6 plots the results of the monotonic static analysis in the transverse and the longitudinal direction in terms of total force versus column drift ratio in the corresponding direction for all six bridges using the corresponding modal force vector computed with the modal analysis described above. The column drift ratio is defined here as the relative displacement in a specific direction of the node at the deck centroid above the column of interest to the height of this node from the top of the foundation for the FB bridges, from the top of the piles for the RPF bridges and from the bottom of the foundation for the RSF bridges.

Table 2.4. Modal periods for the main mode in transverse and longitudinal direction of the six bridges.

	FB17	RPF17	RSF17	FB8	RPF8	RSF8
$T_{1,T}$, (s)	1.25	0.83	1.15	0.45	0.40	0.62
$T_{1,L}$, (s)	0.71	0.88	0.94	0.31	0.54	0.61

The monotonic static analysis results indicate the expected major differences in initial stiffness and strength of the bridges in the transverse direction. At 4% column drift ratio in the transverse direction, bridge RPF17 and RSF17 have 1.7 times the strength bridge FB17; Note the significantly higher initial stiffness of bridge RPF17 compared to that of bridges FB17 and RSF17. Regarding the 8 m tall bridges, bridges RPF8 and RSF8 have 1.5 and 1.6 times, respectively the strength of bridge FB8 at 3% drift ratio while the initial stiffness of bridge RPF8 is significantly higher than that of bridges FB8 and RSF8.

The pushover analysis in the longitudinal direction shows that the three 17 m tall bridges have similar behavior up to 4% drift ratio. For the 8 m tall bridges, bridge FB8 has the highest initial stiffness as well as strength for any drift ratio.

Based on the pushover analysis results, the column axial compression force increase in the exterior column at 4% column drift ratio in the transverse direction was less than 0.4 MN for all bridges. As described in the next section, this value is significantly smaller than the level of column compression force increase computed with response history analysis. This is because the static pushover analysis does not account for the vertical inertia effects. Note that the vertical component of the excitation is not used here.

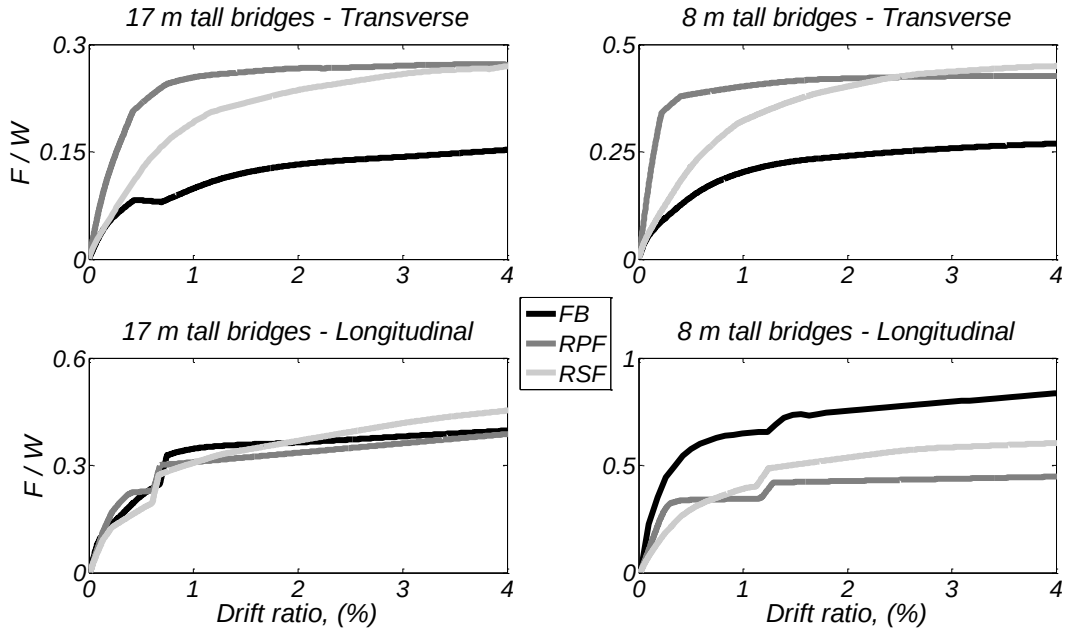

Figure 2.6. Force-displacement response of the six bridges based on a pushover analysis: (top row) in the transverse direction; (bottom row) in the longitudinal direction. Left column shows the results for the 17 m tall bridges and right column for the 8 m tall bridges.

2.5.2 Mean response history analysis results

Presented below are the results of nonlinear response history analysis to the sets of 14 ground motions. For each set of ground motions scaled at the DE and MCE level of shaking, two analyses cases were performed: (1) the first analysis considered the fault-normal and fault-parallel component parallel to the transverse, and longitudinal direction, respectively, of the bridges, termed as the FNT case; and (2) the second analysis considered the fault-normal and fault-parallel component parallel with the longitudinal and transverse axis, respectively, of the bridges, termed as the FNL case. The arithmetic mean results of specific response parameters for the FNT and FNL analyses are listed in Table 2.5 and 2.6, respectively.

Results for both the DE and MCE level of shaking are presented in each of these tables. The displacement response parameters listed in these tables are as follows: (a) the column (peak among all four columns) drift ratio at any horizontal direction; (b) the residual column drift ratio (only for the FNT analysis case); (c) the displacement of the expansion joint in the longitudinal direction; (d) the peak displacement of the bearings at the abutments in any horizontal direction; (e) the peak settlement in any of the piles of the rocking pile-foundations; and (f) the peak settlement computed in any of the springs

under the shallow foundations. Other response parameters provided are the tension strain of the longitudinal reinforcement at the base and at the top of the exterior and interior columns as well as the peak longitudinal tension strain of the deck along its entire length. As reported, the tensile strain of the deck is the total strain. Lastly, these tables list the compression axial force increase $\Delta P_c/P_g$ in both the columns where ΔP_c is the difference between the peak axial compression force computed in a column and the compression force due to gravity P_g. The compression axial force increase of the columns is calculated after filtering out the computed axial force history to eliminate spurious spikes related to the type of the nonlinear material and F-Δ relations used here (Wiebe and Christopoulos 2010). A low-pass finite impulse response filter in MATLAB of order equal to 5000 is used. The ΔP_c for two different cut-off frequencies—10 Hz and 5 Hz—are reported.

Table 2.5. Mean response parameters for the six bridges subjected to the 14 ground motions scaled at the DE and MCE, in parenthesis, level of shaking for case FNT.

		FB17	RPF17	RSF17	FB8	RPF8	RSF8
	Column drift ratio, (%)	2.81 (4.89)	2.29 (4.07)	2.54 (3.99)	2.28 (3.60)	3.10 (4.56)	3.43 (4.96)
	Residual drift ratio, (%)	0.08 (0.15)	0.01 (0.01)	0.06 (0.17)	0.06 (0.07)	0.03 (0.07)	0.08 (0.16)
	Expansion joint displ., (m)	0.20 (0.30)	0.20 (0.33)	0.19 (0.29)	0.05 (0.08)	0.13 (0.25)	0.14 (0.25)
	Bearing displ., (m)	0.44 (0.72)	0.24 (0.39)	0.23 (0.39)	0.22 (0.31)	0.18 (0.32)	0.19 (0.31)
	Pile settlement, (mm)	N/A	17 (21)	N/A	N/A	27 (38)	N/A
	Foundation settlement, (m)	N/A	N/A	0.12 (0.17)	N/A	N/A	0.16 (0.22)
Longitudinal reinforcement tensile strain	Interior column base (%)	3.29 (5.01)	0.18 (0.21)	0.11 (0.13)	3.55 (5.18)	0.21 (0.32)	0.09 (0.11)
	Exterior column base (%)	3.44 (5.30)	0.16 (0.18)	0.09 (0.12)	3.96 (5.57)	0.15 (0.20)	0.08 (0.10)
	Interior column top (%)	1.63 (2.83)	N/A	N/A	1.56 (2.93)	N/A	N/A
	Exterior column top (%)	1.63 (2.83)	N/A	N/A	1.47 (2.71)	N/A	N/A
Column axial compression force increase	Interior col., (10 Hz)	0.16 (0.21)	0.64 (0.88)	0.36 (0.40)	0.34 (0.44)	1.57 (1.80)	0.84 (1.02)
	Exterior col., (10Hz)	0.17 (0.21)	0.39 (0.56)	0.24 (0.32)	0.42 (0.48)	1.06 (1.37)	0.61 (0.78)
	Interior col., (5 Hz)	0.16 (0.21)	0.50 (0.65)	0.34 (0.39)	0.33 (0.42)	1.06 (1.29)	0.79 (0.96)
	Exterior col., (5Hz)	0.17 (0.21)	0.33 (0.48)	0.22 (0.31)	0.40 (0.47)	0.79 (0.96)	0.58 (0.74)
	Deck tensile strain, (%)	0.02 (0.05)	0.16 (0.23)	0.16 (0.22)	0.05 (0.08)	0.17 (0.25)	0.18 (0.27)

Table 2.6. Mean response parameters for the six bridges subjected to the 14 ground motions scaled at the DE and MCE, in parenthesis, level of shaking for case FNL.

		FB17	RPF17	RSF17	FB8	RPF8	RSF8
	Column drift ratio, (%)	2.17 (3.24)	2.15 (3.56)	2.16 (3.29)	1.92 (3.16)	3.01 (4.44)	3.38 (4.99)
	Expansion joint displ., (m)	0.26 (0.42)	0.28 (0.49)	0.27 (0.46)	0.09 (0.16)	0.26 (0.37)	0.25 (0.37)
	Bearing displ., (m)	0.35 (0.53)	0.30 (0.51)	0.29 (0.48)	0.17 (0.27)	0.27 (0.38)	0.26 (0.38)
	Foundation settlement, (m)	N/A	N/A	0.11 (0.17)	N/A	N/A	0.16 (0.23)
Longitudinal reinforcement tensile strain	Interior column base (%)	3.19 (4.68)	0.19 (0.22)	0.12 (0.12)	4.31 (6.37)	0.16 (0.21)	0.09 (0.11)
	Exterior column base (%)	3.24 (4.74)	0.16 (0.19)	0.10 (0.12)	4.56 (6.60)	0.14 (0.17)	0.08 (0.10)
	Interior column top (%)	2.65 (4.23)	N/A	N/A	3.43 (5.44)	N/A	N/A
	Exterior column top (%)	2.65 (4.23)	N/A	N/A	3.38 (5.43)	N/A	N/A
Column axial compression force increase	Interior col., (10 Hz)	0.25 (0.26)	0.59 (0.73)	0.34 (0.43)	0.50 (0.60)	1.18 (1.47)	0.82 (1.06)
	Exterior col., (10Hz)	0.26 (0.29)	0.38 (0.57)	0.25 (0.35)	0.50 (0.61)	0.92 (1.18)	0.61 (0.85)
	Interior col., (5 Hz)	0.23 (0.25)	0.46 (0.58)	0.33 (0.41)	0.43 (0.54)	0.82 (1.08)	0.78 (0.99)
	Exterior col., (5Hz)	0.24 (0.28)	0.33 (0.46)	0.24 (0.32)	0.44 (0.55)	0.64 (0.91)	0.60 (0.82)
	Deck tensile strain, (%)	0.02 (0.03)	0.13 (0.20)	0.11 (0.18)	0.05 (0.08)	0.12 (0.20)	0.14 (0.23)

2.5.2.1 Results for the case with fault-normal component in the transverse direction (FNT)

First the response of the 17 m tall bridges (FB17, RPF17, RSF17) is discussed. The drift ratio of the FB, RPF, and RSF bridges was 2.81%, 2.29%, and 2.54%, respectively, at the DE level of shaking. The corresponding values at the MCE level of shaking were 4.89%, 4.07%, and 3.99%, respectively. Note that the rocking foundation designs for the 17 m tall bridges resulted in drift ratios about 0.81 to 0.90 times that of the FB bridge for both levels of excitation. The expansion joint displacement of bridge FB17 was 0.20 m and 0.30 m at the DE and MCE levels of shaking, respectively. In the longitudinal direction (at both these levels of displacement) the expansion joint displacement capacity was exceeded and the passive resistance of soil in the abutment was fully mobilized; the approach slab has possibly been completely damaged. Similar was the level of response of the expansion joints and of backfill in the abutments in bridges RFP17 and RSF17. Bridge FB17 developed 0.44 m and 0.72 m displacement of the bearings at the DE and MCE level of shaking, respectively. Bridges RPF17 and RSF17 experienced displacement of the rubber bearings less than 0.39 m at the MCE level of shaking, remaining undamaged. The significantly larger stiffness and strength of the LPRBs were instrumental in reducing the displacement of the bearings in bridges RPF17 and RSF17 compared to bridge FB17.

Figure 2.7 (a) and (b) plot the instantaneous displacement, in the transverse direction, of the 17 m tall and 8 m tall bridges, respectively, for the FNT analysis case when the interior column drift ratio was 4%. The profiles reported are the arithmetic mean profiles for the ground motions where the column drift ratio reached 4%. The displacement profiles of the bridges with rocking foundations was significantly different than that of the fixed-base bridges having a more curved shape due to the smaller displacements in transverse displacement in the abutments. This difference in displacement in the transverse directions between the abutments and the columns results in bending of the deck and should be explicitly considered during the design to prevent damage of the post-tension strands. Here the characteristics of the columns and of the LPRBs were designed so that the deck remained nominally elastic and the post-tensioned strands elastic and undamaged.

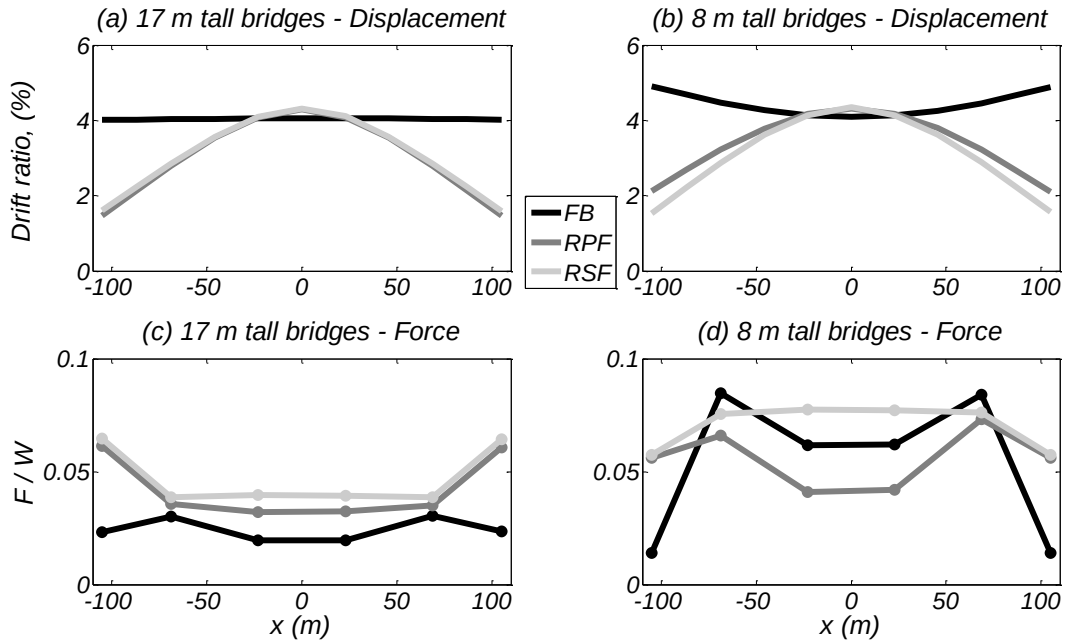

Figure 2.7. Instantaneous profile of drift ratio and total lateral resisting force in the transverse direction of the bridges at 4% drift ratio of the interior column (when the column experiences it for first time). The profiles are the arithmetic mean profiles computed for the ground motions (6 to 10 motions out of the 14 for the FNT analysis case) where interior column drift ratio reaches 4%. At the mid-length of the deck x = 0 m.

Figure 2.7(c) and (d) plot the shear force in the transverse direction along the length of the bridges at the same instants to those described in Figure 2.7(a) and (b), respectively. The shear force along the bridge is more uniform for bridge FB17 compared to the profile of shear force in bridges with the rocking foundations. This is because of the effect of the LPRBs in bridges RPF17 and RSF17, which resulted in larger shear force at the abutments.

The bridges with rocking foundations resulted in elastic response of the columns, with the tension strain less than 0.21% at the MCE level of shaking. The deck remained nominally elastic with longitudinal tension strain equal to 0.23% at the MCE. The total

strain in the strands for this level total deck strain is 0.8%. For this level of tensile strain the strands remain elastic and undamaged (Veletzos and Restrepo 2011). For bridge RSF17, the settlement of the shallow foundations was 0.12 m, and 0.17 m at the DE and MCE level of shaking. Figure 2.8(a) and (b) show the computed moment versus rotation, M-θ, of the shallow foundation in the transverse direction of bridge RSF17 and RSF8, respectively, for one of the 14 ground motions used scaled at the MCE level of shaking. The M-θ for both these bridges shows less than 0.7% rotation when passing from zero moment up to 6.6% foundation rotation. While the column residual drift ratio bridges RPF17 was practically zero, bridge RSF17 experienced 0.17% residual drift ratio at the MCE level of shaking. The vertical displacement of the piles of bridge RPF17 reached 38 mm at the MCE level of shaking, as shown in Table 2.5.

Bridge FB17, however, developed significant inelastic deformations in the columns, especially at their base, with the strains that reached 3.44%, and 5.30% at the DE and MCE level of shaking, respectively. At both these levels of inelastic deformation extensive spalling of concrete in the flexural plastic hinges should be expected while longitudinal reinforcement bar buckling may occur at the MCE level of shaking. The residual drift ratio of bridge FB17 was small and equal to 0.15% at the MCE levels of shaking.

The difference in the level of inelastic response between bridges FB17 and RPF17 is shown in Figure 2.9, which plots the total shear force in the transverse direction of the bridges versus column drift ratio for one of 14 ground motions scaled to the MCE level of shaking. This figure shows the smaller extent of inelastic response that occurs in bridge RPF17, mainly due to inelastic behavior of the lead-plug of the LPRBs.

The axial compression force increase, ΔP_c, (for a 10 Hz cut-off frequency) in the columns of the FB17 and the RSF17 reached 0.21 and 0.40, respectively, at the MCE hazard level of shaking. This increase is due to framing between the columns the deck and the abutment, and vertical inertia effects. The axial compression force variation was significantly higher in bridge RPF17, reaching 0.64 and 0.88 at the DE and MCE levels of shaking, respectively. This larger magnitude of axial compression force increase is due to the greater regain of stiffness that occurs in the RPF bridges upon contact of the pile cap to the piles compared to the other two bridge designs.

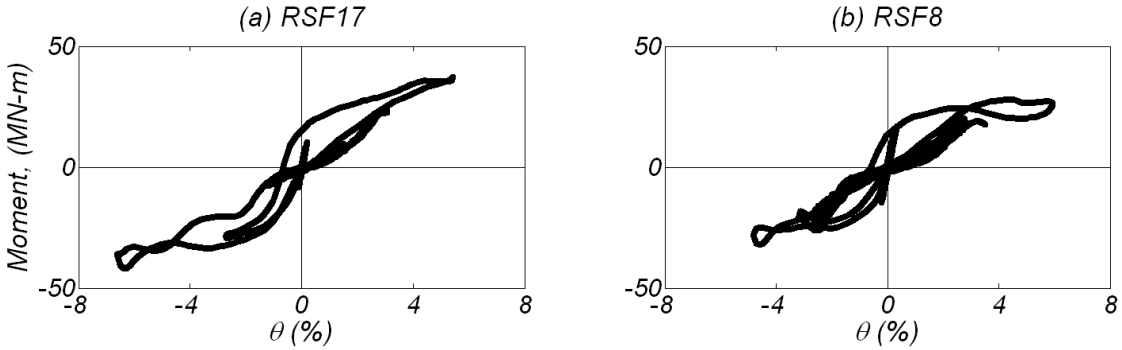

Figure 2.8. Moment-rotation response of shallow foundation of interior column of bridges RSF17 and RSF8 for one of the 14 ground motions scaled at MCE.

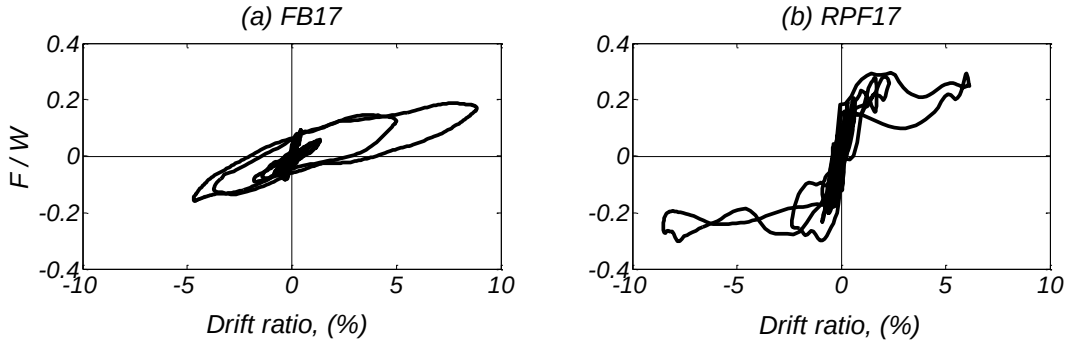

Figure 2.9. Total resisting force (columns, bearings, shear keys) in the transverse direction versus column drift ratio for bridges FB17 and RFP17 for one (different for each bridge) of the 14 ground motions scaled at the MCE.

Next, the response of the 8 m tall bridges (FB8, RPF8, and RSF8) is discussed. In contrast to the behavior of the 17 m tall bridges, bridges RPF8 and RSF8 experienced significantly higher levels of displacements compared to bridge FB8 at both the DE and MCE levels of shaking. While the drift for bridge FB8 was 2.28% and 3.60% at the DE and MCE level of shaking, respectively, for bridges RPF8, and RSF8 the drift ratio ranged between 3.10% and 3.43%, respectively, at the DE .The corresponding numbers for the MCE level were 4.56% and 4.96%. This is because the effect of reduced hysteretic energy dissipation (elastic columns on rocking foundations) on the level of increase of nonlinear displacement compared to that of columns that develop plastic hinges, increases with decrease of the structural period (Antonellis and Panagiotou 2013a) for initial periods 0.5 to 2 s.

Despite the larger drift ratio, the bridges with rocking foundations (RSF8 and RPF8) did not experience inelastic deformations in the columns, with tensile longitudinal strain less than 0.32% at the MCE level of shaking. Bridge RSF8 resulted in soil settlements equal to 0.16 m and 0.22 m at the DE and MCE level of shaking, respectively. Figure 2.8(b) shows the computed moment rotation of the shallow foundation of bridge RSF8 for one ground motion. The deck remained nominally elastic for both bridges RPF8 and RSF8, with less than 0.27% tension longitudinal strain at the MCE level of shaking. The corresponding total strain in the strands was 0.8%. Bridge FB8 however, experienced significant inelastic deformations in the columns, especially at their base, with longitudinal tension strains reaching 3.96%, and 5.57% at the DE and MCE level of shaking, respectively. The residual drift ratio at MCE level of shaking of bridges FB8, RP8, and RS8 were small and less than 0.16%.

The 8 m tall bridges experienced about two times the axial compression force increase, ΔP_c, of the 17 m tall bridges due to larger vertical inertia effects. The column axial force compression increase in bridges FB8 and RSF8 reached 0.42, and 0.84, respectively, at the DE level of shaking. The corresponding values at the MCE level of shaking were 0.48, and 1.02, respectively. Bridge RPF8 experienced significantly higher ΔP_c, which was 1.57 and 1.80 at the DE and MCE level of shaking, respectively. Note that the corresponding values for 5 Hz cut-off frequency reduced to 1.06 and 1.29, indicating that this increase in axial load increase is significant in frequencies between 5

and 10 Hz. For the FB and RSF bridges negligible differences in ΔP_c occurred for the 5 Hz and 10 Hz cut-off frequencies demonstrating that ΔP_c was rich in frequencies lower than 5 Hz.

2.5.2.2 Results for the FNL analysis case

Compared to the FNT case, the FNL analysis case resulted in larger responses for the expansion joint displacements, the displacement of the bearings of the bridges with rocking foundations, the column tension strains for bridge FB8, especially at the top, and in some cases for the column axial compression force increase for the fixed-base bridges. Bridge FB17 reached 0.26 m, and 0.42 m displacement of the expansion joints at the DE and MCE level of shaking, respectively. The corresponding values for bridges RPF17 and RSF17 were 0.28 m and 0.49 m. Both bridges FB17 and FB8 developed significant inelastic response in the columns with the tension strain of the longitudinal reinforcement reaching 3.24%, and 4.56%, respectively at the DE level of shaking. The corresponding values of strain at the MCE level of shaking were 4.74%, and 6.60%. Note that the tensile strains at the top of the columns are significantly higher for the FNL case for bridges FB17 and FB8, reaching 4.23% and 5.44% at the MCE level, respectively. For bridges FB17 and FB8 the column axial compression force increase ΔP_c was up to 1.38 times (bridge FB17) that of the FNT case.

2.6 Conclusions

In this chapter the numerical investigation of the seismic response of six reinforced concrete bridges was presented. All bridges were 210 m long, linear, and had 5 spans. Three of the bridges analyzed were 17 m tall and three were 8 m tall. For each bridge height, three designs of columns and foundations were studied: (a) a conventional bridge designed according to Caltrans seismic design criteria that is expected to develop flexural plastic hinges in columns fixed to pile foundations and the foundation fixed to the ground; (b) columns designed to remain nominally elastic and fixed on rocking pile foundations; and (c) columns designed to remain nominally elastic and fixed to rocking shallow foundations.

The columns used in the bridges with rocking foundations were 2.5 m in diameter with a 3% longitudinal steel ratio, ρ_l; the fixed-base bridges had 1.8 m diameter columns with ρ_l = 2%. The pile cap of the rocking pile foundations had a volume 1.6 times that of the pile cap used in the fixed-base bridges. The columns of the bridges with rocking foundations used a pin connection between the column and the deck. In addition, the bridges with rocking foundations used 1.26 m diameter lead-plug rubber bearings at the abutments compared to 0.6 m diameter laminated rubber bearings used in the fixed-base bridges. Bridges RPF17 and RSF17 at 4% drift ratio in the transverse direction had 1.7 times the lateral strength of the fixed-base bridge. Bridges RPF8 and RSF8 at 4% drift ratio in the transverse direction had about 1.6 times the lateral strength of the fixed-base bridge. Three-dimensional nonlinear response history analyses were performed, using two components of horizontal excitation for a set of ground motions scaled to two seismic hazard levels with return periods of 975 [design earthquake (DE)] and 2475 years [maximum considered earthquake (MCE)], respectively. In one analysis case the fault-

normal component of the motions was parallel to the transverse direction of the bridges (FNT case) and in the other case parallel to the longitudinal axis of the bridge (FNL case). Based on the results of the study the following conclusions are drawn:

1. The conventionally designed fixed-base bridges experienced significant inelastic deformations at both the DE and MCE levels of shaking. At the DE level of shaking the column drift ratio of bridges FB17 and FB8 was 2.81% and 2.28%, respectively. The corresponding values at the MCE level of shaking were 4.89% and 3.60%, respectively. At the DE level of shaking the tension strain of the longitudinal reinforcement of the columns of bridges FB17 and FB8 reached 3.44% and 4.56%, respectively. The corresponding values at the MCE level of shaking were 5.30% and 6.60%, respectively. For this level of inelastic deformation, extensive spalling of the concrete and possibly extensive yielding of the transverse reinforcement and buckling of the longitudinal rebars should be expected. The residual drift ratio at the MCE level of shaking of bridges FB17 and FB8 was small and less than 0.15%. The 17 m tall fixed-base bridge experienced 0.26 m, and 0.42 m of displacement in the longitudinal direction at the DE and MCE levels of shaking, respectively. This level of displacement exceeds the 0.1 m of displacement of the expansion joints and resulted in failure of the backwall in the abutments and the approach slab. The displacements of the bearings at the abutments were 0.44 and 0.72 m at the DE and MCE levels of shaking, respectively, with the latter to possibly exceed the deformation capacity of the bearings.

2. Both the 17 m tall and 8 m tall bridges with rocking foundations resulted in nominally elastic response of the columns and the deck, while the post-tensioned strands remained elastic at both levels of shaking. Bridges RPF17 and RSF17 developed column drift ratios up to 0.83 times that of bridge FB17 in the FNT case. Bridges RPF8 and RSF8 developed drift ratios up to 1.4 times those of bridge FB8. The level of increase of nonlinear displacements for a bridge with columns on rocking foundations compared to that of a bridge designed to develop flexural plastic hinges in the columns should be expected to increase with decrease of structural period (for periods between 0.5 and 2 s). The residual column drift ratio of the bridges with rocking pile foundations was less than 0.07% and that of the bridges with rocking shallow foundations less than 0.17%. Inelastic response of the soil occurred at the ends of the rocking shallow foundations. For bridge RSF17 soil settlement reached 0.12 m, and 0.17 m (0.021 times the length of the foundation), respectively, at the DE and MCE level of shaking. The corresponding values for bridge RSF8 were 0.16 m and 0.23 m. The peak pile settlement of RPF was less than 40 mm at the MCE level of shaking. Bridges with rocking foundations developed displacements in the longitudinal direction which reached 0.49 m at the MCE level of shaking.

3. The use of two large LPRBs at each abutment of these bridges was very effective in enhancing stiffness and strength, providing hysteretic energy dissipation, and thus controlling the level of displacements these bridges experienced. Differences in the strength and stiffness of the abutments and the columns resulted in bending of the deck in the transverse direction which should be explicitly considered in the analysis and design to ensure that the deck remains nominally elastic and that the strands do not yield.

4. The bridges with rocking foundations experienced higher levels of column axial compression force increase, ΔP_c, than the fixed-base bridges. This increase is primarily due to vertical inertia effects and secondarily due to framing effects between the columns,

the deck, and the abutments. The columns on rocking pile foundations experience the highest ΔP_c. This is because sudden regain of stiffness upon contact of the pile cap to the piles excites significant vertical oscillation and vertical inertia effects. Independent of the type of design ΔP_c of the 8 m tall bridges was 2 to 2.4 times that of the corresponding 17 m tall bridges. For bridge RPF8, ΔP_c reached 1.57 and 1.80 at the DE and MCE levels of shaking, respectively. The corresponding values for axial force histories filtered at 5 Hz were 1.06 and 1.29 indicating that these axial force histories were rich in high frequencies ranging between 5 Hz and 10 Hz. The ΔP_c of the fixed-base and RSF bridges was dominated by frequencies lower than 5 Hz. This axial compression force increase should be explicitly considered in the design of the columns and the foundations.

Chapter 3: Large-Scale Shake-Table Test of Bridge Columns with Rocking Shallow Foundations

3.1 Introduction

Traditional seismic design of bridges in California is predicated on inelastic behavior of the columns with the formation of plastic hinges (Caltrans SDC 2010). Although bridges designed in that matter are usually safe from collapse, may require expensive and time consuming repairs after a seismic event. For example, residual drifts of bridge columns resulted into demolition and replacement of over 100 bridges after the 1995 Kobe earthquake (Jeong et al. 2008). Even in columns that remain functional, residuals drifts larger than 1% are usually repaired for aesthetic reasons and public safety perception. Additional casting of concrete and enlargement of the cross sections along the height of the columns is done so that they appear straight. Minor concrete cracking and spalling in the columns can result in such repairs, possibly costing up to 20% of the initial construction cost (Antonellis and Panagiotou 2013a). For other column repairs that require bridge closure, the downtime translates into additional indirect costs.

The peak and residual drift demands on bridge columns tend to be higher for near-fault pulse-type excitations (Phan et al. 2007; Schoettler et al. 2012; Antonellis and Panagiotou 2014). For this type of motion, it is not unusual for the peak drift ratio, Θ_r, of bridge columns to be in the range of 6% to 10%, where Θ_r is defined as the lateral displacement of the centroid of the superstructure with respect to the column base, divided by the height of that point from the base.

An alternative seismic design for bridge columns involves the use of rocking foundations that are allowed to uplift during the seismic excitation preventing damage at the base of the columns (Anastasopoulos et al. 2010; Pecker 2006). Such a design can allow the column to remain nominally elastic when combined with a pin connection between the column and the overlying deck (Deng et al. 2012a; Antonellis and Panagiotou 2014).

The merits of the rocking isolation approach have been extensively studied analytically in the recent years by various researchers (Sakellaraki and Kawashima 2006; Apostolou et al. 2007; Deng et al. 2012b; Gelagoti et al. 2012; Antonellis and Panagiotou 2014). Sakellaraki and Kawashima (2006) analyzed a bridge with columns on rocking foundations under a single near-fault ground motion record demonstrating the damage resistance of such columns. In the previous chapter it was demonstrated that hypothetical bridges located 3 km from the Hayward fault can be designed using rocking foundations

to eliminate column damage after the Maximum Considered Earthquake (MCE) level of seismic excitation.

The seismic response of rocking foundations has been studied experimentally using large-scale pseudo-static cyclic tests (Negro et al. 2000), shake-table tests with (Paolucci et al. 2008; Shirato et al. 2008) and without (Saiidi et al. 2002; Espinoza and Mahin 2008) physical modeling of the soil, and small-scale shake table tests including physical modeling of the soil (Anastasopoulos et al. 2013), as well as in centrifuge tests (Deng et al. 2012a; Loli et al. 2014; Kim et al. 2014). Saiidi et al. (2002) and Espinoza and Mahin (2008) used relatively thin elastic pads to represent soil, whereas centrifuge tests do not model physically the reinforced concrete members. For example, Deng et al. (2012a) used notched aluminum sections for modeling the plastic hinges of reinforced concrete columns and Loli et al. (2014) used small scale modeling for the reinforced concrete elements. Each of these studies has one or more shortcomings, including the small size of test specimen, static excitation, idealized backfill soil and specimen preparation conditions, and lack of groundwater in subsurface soils. As such, large-scale shaking table tests of rocking bridge foundations constructed using realistic materials and construction methods, and tested under dynamic excitation with and without groundwater in the underlying foundation soils, represents a significant advancement in available test data for this type of foundation design.

Large-scale experimental studies of 1-m-square rocking foundations with FS_v up to 5 on top of 3 m of sand and placed inside a 1-m-deep trench were performed by Negro et al. (2000). Pseudo-static cyclic loading was used in these tests. The factor of safety for vertical loading, FS_v, is equal to the ultimate bearing capacity of the foundation soil divided by the applied vertical load. Two levels of sand compaction were studied: one with a relative density D_r = 45% and the other with a relative density of D_r = 85%. For D_r = 85% tests, the foundations developed peak rotations θ_f = 2.3%, with rotations at zero moment equal to 0.5% and settlements less than 0.02B, where B is the length of the foundation in the direction of loading.

Shake table tests of 0.5-m-square rocking foundations on top of well-compacted soil (FS_v = 29) were performed by Paolucci et al. (2008) and Shirato et al. (2008). The specimens were placed on top of 2.1 m clean dry sand of D_r = 85% with embedment depths ranging from 0 to 0.1 m. For the largest embedment depth and a peak θ_f equal to 5%, the residual rotation was 1% and the settlement was 0.012B. Anastasopoulos et al. (2013) conducted shake table tests of a 0.55-m-long strip foundation supporting a cantilever column. For these specimens with FS_v = 3.3, residual drift ratios of more than 3% developed after peak drift ratios reached between 11% and 16%.

Despite the obvious advantages of close-to-real-scale testing, centrifuge tests are also useful because they have the advantage of significantly smaller cost and enable more accurate modeling of the effective stresses in the soil. Centrifuge tests of single bridge columns under dynamic excitation (Gajan and Kutter 2008) have demonstrated that rocking shallow foundations exhibit a reliably predicted, non-deteriorated moment-rotation behavior. They have also shown that re-centering, energy dissipation and settlement behavior of rocking footings are better correlated to the critical contact area ratio, A/A_c, where A is the area of the footing and A_c is the minimum soil-footing contact area that supports the vertical load during rocking. Deng and Kutter (2012) and Deng et al. (2012a) conducted centrifuge tests of single bridge columns, or 2-span 2-column bent

bridge models under earthquake excitation with A/A_c ranging from 8 to 45. They have concluded that rocking shallow foundations can develop Θ_r up to 5% with small residual rotations and settlements less than $0.01B$ for up to 0.15 rad cumulative rotation.

This chapter presents the shake table test results of two 460-mm-diameter bridge columns supported on 1.52-m-square shallow rocking foundations on top of clean, well-compacted sand, subjected to unidirectional seismic excitation. The tests were conducted in May 2013 at the outdoor shake table of the Network for Earthquake Engineering Simulations (NEES) at the University of California at San Diego (UCSD) using the largest stiff soil confinement box in the U.S. Three series of test were performed; each series had different ground water table elevation and backfill conditions. The objective of these tests was to demonstrate, based also on accumulated knowledge from previous tests, that bridge columns on rocking foundations can be successfully designed to develop drift ratios of the order of 7% with limited rotations and settlements. These are the largest shake table tests ever conducted on rocking shallow footings with foundation soil. The tests also produced the largest level of dynamic lateral displacements that have ever been reported for similar scale specimens.

3.2 Test Specimens and Test Setup

The test setup involved the use of the NEES@UCSD Large High-Performance Outdoor Shake Table (LHOPST) and Large Soil Confinement Box (LSCB). The LSCB is a very stiff confinement structure composed of high-strength precast concrete panels and an exterior steel support frame (Sander et al. 2013, Fox et al. 2014). The LSCB was post-tensioned to the shake table platen with internal dimensions equal to 10.1-m-long × 4.6-m-wide × 7.6-m-high; see Figure 3.1 and 3.2(a-b). Uniaxial excitation was applied by the shake table along the East-West direction.

The geometry of the specimens was determined based on the full-scale fixed-base 1.2 m diameter column supporting a seismic weight, W, of 2.32 MN tested by Schoettler et al. (2012). Appropriate structural scaling laws (Espinoza and Mahin 2008) were applied to maintain similar working stress at the base of the column. A length scale factor, $1/S$, where $S = 3$, was used, resulting in 0.46 m column diameter with a seismic weight of 0.25 MN on top. All quantities reported in this paper are in model scale.

The test specimens were placed in the LSCB that included soil up to 3.35 m high. The geometry of the two specimens within the LSCB is shown in Figure 3.1. The columns were supported on 1.52-m-square foundations that were 0.51 m tall and had 0.66 m of embedment. The height, h, from the base of the foundation to the center of gravity of the mass blocks was 3.03 m, resulting to moment-to-shear ratio $h/B = 2$, indicating a rocking-dominated foundation with very little sliding (Gajan and Kutter 2009). One specimen had its foundation aligned with the direction of excitation, while the foundation of the second specimen was 30^o askew.

Three different tests were conducted in terms of underground water elevation and backfill conditions: (a) Test Day 1 configuration consisted of no underground water with moist ($w_c \approx 5\%$) and well-compacted backfill sand; (b) Test Day 2 configuration consisted of a water level 1.2 m below the foundations with almost dry ($w_c \approx 2\%$) loose backfill sand; and (c) Test Day 3 configuration consisted of a water level 0.6 m below the foundations and weak concrete casted around the footings. Figure 2.1(a) shows the plan

view of the test setup with the location of the aligned and skewed specimens inside the LSCB. Figure 3.1(b) shows the elevation view of the test configuration depicting the soil, the water elevation for the different test days, and the elevation of the specimens.

The longitudinal reinforcing steel in each column consisted of 16 No. 6 A706 Grade 60 steel bars, corresponding to longitudinal steel ratio of 2.8%. The transverse reinforcement consisted of a No. 3 A706 Grade 60 spiral with a pitch of 0.051 m. The cross section near the top of the column was enlarged into a square cross section with a side dimension equal to 0.61 m. This part of the column is termed here as load stub.

Steel beams were placed, using post-tensioned steel rods, in the four sides of the load stub. Three mass blocks were then placed on top of the steel beams and the load stub of each specimen, and were post-tensioned to the steel beams near their ends. To prevent possible overturning of the specimens that could damage the LSCB, a restraining system (of 10 kN weight) was constructed for each footing. It consisted of hollow square steel structural tubing cast and grouted into near each corner of each footing, extending upwards above the footing. The tubing was rigidly connected to steel beams extending horizontally outwards from the footings. Wood beams of tapered thickness were fixed to the steel beams [Figure 3.2 (b)]. The taper was sized so that the restraining system would touch the sand surface when the footing rotation was 10 to 15%, depending on the soil elevation, footing settlement, and precision of sand leveling beneath the tapered wood beams. The restraining system was activated only for the skewed specimen on Test Day 3, motion 9.

Additional design details and construction drawings and photos of the test specimens are presented by Antonellis et al. (2014b). Figure 3.2(b) shows a crane placing the assembled aligned specimen inside the LSCB.

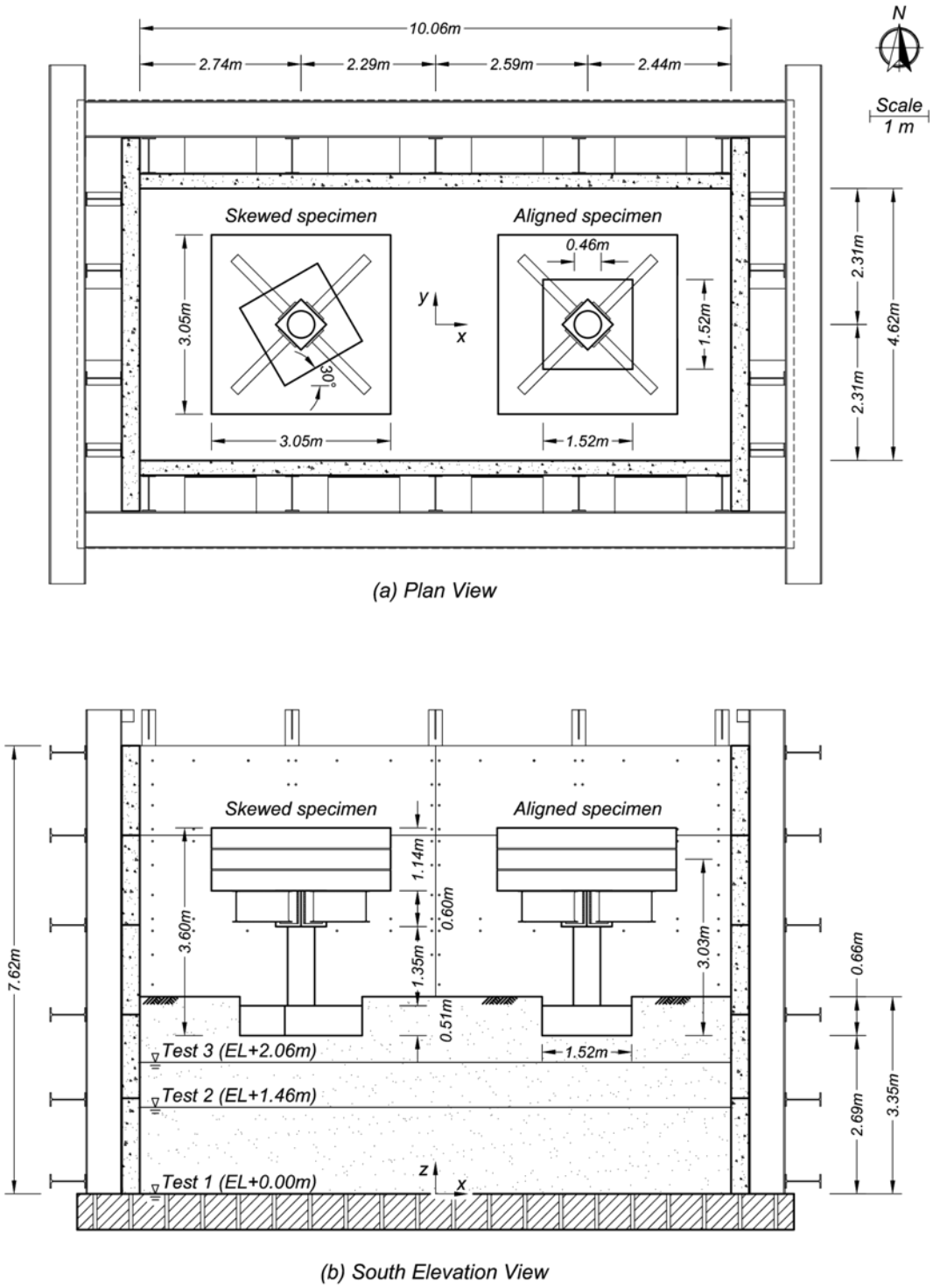

Figure 3.1. (a) Plan and (b) south elevation view of the test setup and basic geometric characteristics of the LSCB, the soil, and the bridge column specimens. The direction of shaking is along the East-West direction.

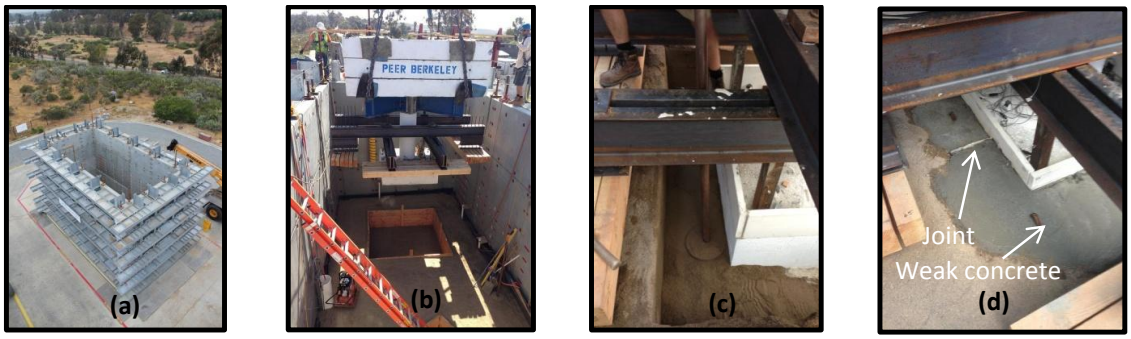

Figure 3.2. Photos of (a) the large soil confinement box (empty), (b) the placement of the aligned specimen before Test Day 1, (c) the backfilling and hand compaction of the sand in the vicinity of the foundation (Test Days 1 and 2), and (d) construction details around the footings for Test Day 3 only.

3.3 Design Objectives and Control Design Parameters

The design specifications for the specimens were as follows: (a) nominally elastic response of the column; (b) less than 1% residual drift ratio for peak drift ratio of 7%; (c) base shear coefficient C_r = 0.25; and (d) residual settlements of the foundation less than 0.01B. The base shear coefficient, Cr, is equal to the foundation base shear that mobilizes the moment capacity of the foundation divided by the weight of the specimen.

The design of the foundations was based on the perspective guideline by Deng and Kutter (2012) that when the critical contact area ratio, A/A_c, is larger than 8, residual rotations are small and settlements are less than 0.01_B for cumulative rotations up to 0.15 rad. The critical contact area, A_c, was determined following the iterative procedure described by Deng and Kutter (2012), neglecting the effect of apparent cohesion in the sand due to moisture. Classical equations have been used for the estimation of ultimate bearing pressure and bearing capacity factors (Salgado 2008), depth factors (Brinch Hansen 1970), shape factors (Vesic 1973) and inclination factors (Meyerhof 1963). Peak friction angle was estimated from Bolton's (1986) empirical equation for triaxial compression conditions with assumed fitting parameters of Q = 10 and RQ = 1. The representative mean effective stress is determined from De Beer (1965), and relative density and constant volume friction angle values are as described in the material properties section below. For the skewed footing, the triangular shape of the critical contact area and its rectangular idealization for bearing capacity estimation was based on Highter and Anders (1985) equations for two-way eccentricity. The critical contact area ratios, A/A_c, before Test Day 1 were equal to 11.3 and 13.5 for the aligned and skewed foundations, respectively. For both cases, the corresponding peak friction angles are practically same and equal to 44.3°. The ratio of the bearing capacity for purely vertical loading to the static vertical load, FS_v, was equal to 23.9 for both specimens based on a peak friction angle of 42.1°.

The moment capacities of the two foundations were determined based on the resistance provided by the underlying soil (Gajan and Kutter 2008) and the passive and frictional resistance at the leading side(s) of the footings. For the aligned footing, moment capacity is determined as

$$M_{c,foot} = \frac{QB}{2}\left(1 - \frac{A_c}{A}\right) + P_p\frac{D}{3} + kP_p\frac{B}{2} \quad (1)$$

where Q is the applied vertical load at the base of the footing, B is the side dimension of the footing parallel to excitation axis, P_p is the passive earth force, D is the embedment depth and k is the concrete-soil friction coefficient, corresponding here to two-thirds of the constant volume friction angle, φ_{cv}.

The calculated moment capacity of the aligned foundation was 229 kN-m, with 201 kN-m provided by the underlying soil resistance, and 252 kN-m for the skewed footing, corresponding to C_r equal to 0.26 and 0.29, respectively. The calculated flexural strength of the column, based on section moment-curvature analysis and as built material properties for axial load equal to 251 kN, was equal to 365 kN-m, ensuring elastic response of the concrete column during rocking. For this calculation, the tensile strain of the outer steel reinforcement was limited to 0.5%.

3.4 Construction Sequence

The LSCB was filled with clean sand up to a height of 3.4 m from the platen of the shake table. Two layers of PVC geomembrane liner and protection nonwoven geotextile were placed in the bottom and along the sides of the LSCB to allow for the addition of water for Test Days 2 and 3. The sand was loaded into the LSCB using a crane and a concrete hopper, and was spread around in loose lifts 0.2 m thick and subsequently was compacted to about 0.15 m. Compaction was performed using a compact skid-steer loader with a vibratory roller attachment and a smaller hand-held vibratory compactor for the area near the walls of the LSCB, as well as for the majority of the soil above the foundation elevation. During compaction the sand was wetted to achieve a target relative density (D_r > 80%).

The specimens were assembled outside the LSCB and were transferred into place by a crane. For construction reasons, the backfilling and compaction of the soil in the vicinity of the footings was done by hand [Figure 3.2 (c)]. After each test day, the soil near the footings was excavated, the specimens were extracted, and the soil surface was re-leveled and compacted by hand before placing the specimens back in place. This construction sequence resulted into moisture loss in the sand used to backfill the footings before Test Day 2, compared to Test Day 1. The water content at the sand in the vicinity of the footings on Test Day 2 was measured immediately after the completion of the tests and was found to be about 2% as opposed to 5% measured for Test Day 1. This affected the overall behavior of the rocking foundations for large rotations due to the sand falling in the gap that formed between the soil and the footing during rocking; this occurred largely during Test Day 2. As a result, on Test Day 3 weak concrete was cast around the perimeter of the footings [Figure 3.2(d)]. This successfully prevented the flow of sand under the footing but also introduced a modest increase in the moment capacity of the rocking foundation.

3.5 Material Properties

The concrete used in the footings and the columns had a specified compressive strength of 41.3 MPa and maximum aggregate size of 9.5 mm. For construction purposes and due to the high congestion of the steel reinforcement throughout the height of the columns, concrete with a higher slump was used for the columns and the load stubs. The slump for the concrete of the foundations and the columns were 140 and 220 mm, respectively. During Test Day 1, the concrete of the foundations had a compressive strength of 42.1 MPa, whereas the concrete used in the columns had a compressive strength equal to 30.3 MPa. The yield stress of the longitudinal steel reinforcement of the column was 495 MPa.

The soil used for this test was Carroll Canyon type II ASTM C33 washed concrete sand, classified as poorly-graded medium sand. Grain sizes D_{50} and D_{10} were 737 and 186 μm, respectively, while the coefficients of uniformity, C_u, and curvature, C_c, were 5.3 and 0.9, respectively. The minimum and maximum dry unit weights of the sand were determined to be 14.4 and 17.7 kN/m^3, respectively. In order to estimate the relative density of the built soil profile, a total of 16 sand cone tests were performed at different stages of the construction. Based those sand cone tests (Antonellis et al. 2014b), the relative density, D_r, of the as-built soil is estimated to be about 90%. A constant volume friction angle value of 33^o has been assumed based on the angularity of the sand.

3.6 Instrumentation

A total of 141 sensors, including 80 accelerometers, and 21 cameras were used (Antonellis et al. 2014a, 2014b). Three accelerometers were placed at the shake table platen, 12 on the LSCB, 31 in the soil, 15 on the footings, 3 on the restraining system, and 16 on the mass blocks. A total of 32 string potentiometers were used to measure displacements relative to the LSCB: 12 to measure the displacement of the footings; 12 for the mass blocks; and 8 in the vicinity of the foundations to measure the settlements of the soil at the foundation level. Eight pore pressure transducers were placed in the soil to monitor pore water pressures. At selected locations, colored sand was placed on the sides and in some cases under the footings to help identify the sand that was falling into the gap under the rocking footing. A video with clips obtained from the different cameras that summarizes the response for selected ground motions can be found online (Antonellis and Panagiotou 2013b).

3.7 Test Sequence

The test protocol included six historical earthquake ground motion records. Table 3.1 describes the ground motions used including the associated amplitude scale factors. The time of the ground motions was scaled by $\sqrt{1/3}$ = 0.577 to account for the effect of length scale factor of the test specimens. The Pacoima Dam (motion 4), Takatori (motions 5 and 6), and Parachute Test Site (motions 7, 8, and 9) were recorded at a distance equal to 7.0, 1.5, and 1.0 km from the fault rupture plane and included strong pulses. A targeted drift ratio of 3% and 6% was chosen for the Design Earthquake (DE) and MCE levels of shaking, and the amplitude scale factors were determined accordingly for motions 3 (DE

level) and 5 (MCE level). Numerical models using a nonlinear Winkler type model for the foundations (Antonellis and Panagiotou 2014) were used to predict of the results prior to the test to help in selection of the amplitude of the desired ground motions. The Pacoima Dam record was filtered with a low-pass, 5 Hz cut-off frequency to reduce the peak possible force that the LSCB would have to resist; numerical analysis showed that this filter had negligible effect on the performance of the rocking foundation systems. For system identification purposes, white-noise motions were also used before and after every earthquake ground motion. The white-noise input motion had a duration of 300 s and 0.05-g-root-mean-square (RMS) amplitude of acceleration. Motions 7, 8, and 9 were used only in Test Day 3. Figure 3.3 plots the linear acceleration and displacement spectra (3% damping ratio) for Test Day 3 of the recorded soil acceleration at a location near the center of the LSCB and at the foundation base elevation. The recorded motions showed less than 10% difference (in a comparison of the test days) and were in very good agreement with the input motions. The sign convention is as follows: positive horizontal accelerations are towards West and North, and positive vertical accelerations are downwards.

Table 3.1. Ground motions used in the experimental program.

No.	**Station**	**Earthquake location, year**	M_w	R_{rup}, **(km)**	**Amplitude scale factor**	**Recorded peak ground acceleration[§], (g)**
1	Gilroy #1	Loma Prieta, CA, 1989	6.9	9.6	1.0	0.66
2	Corralitos	Loma Prieta, CA, 1989	6.9	3.9	0.8	0.47
3[*]	El Centro #6	Imperial Valley, CA, 1979	6.5	1.4	1.1	0.41
4[†]	Pacoima Dam	Northridge, CA, 1994	6.7	7.0	0.8	0.60
5[‡]	Takatori	Kobe, Japan, 1995	6.9	1.5	0.5	0.40
6	Takatori	Kobe, Japan, 1995	6.9	1.5	1.0	0.95
7[§]	Parachute Test Site	Superstition Hills(B), CA, 1987	6.5	1.0	1.0	0.43
8[§]	Parachute Test Site	Superstition Hills(B), CA, 1987	6.5	1.0	-1.0	0.46
9[§]	Parachute Test Site	Superstition Hills(B), CA, 1987	6.5	1.0	1.1	0.47

[*]Design earthquake, [†]filtered at 5 Hz (low-pass)
[‡]Maximum considered earthquake, [§]Test Day 3.

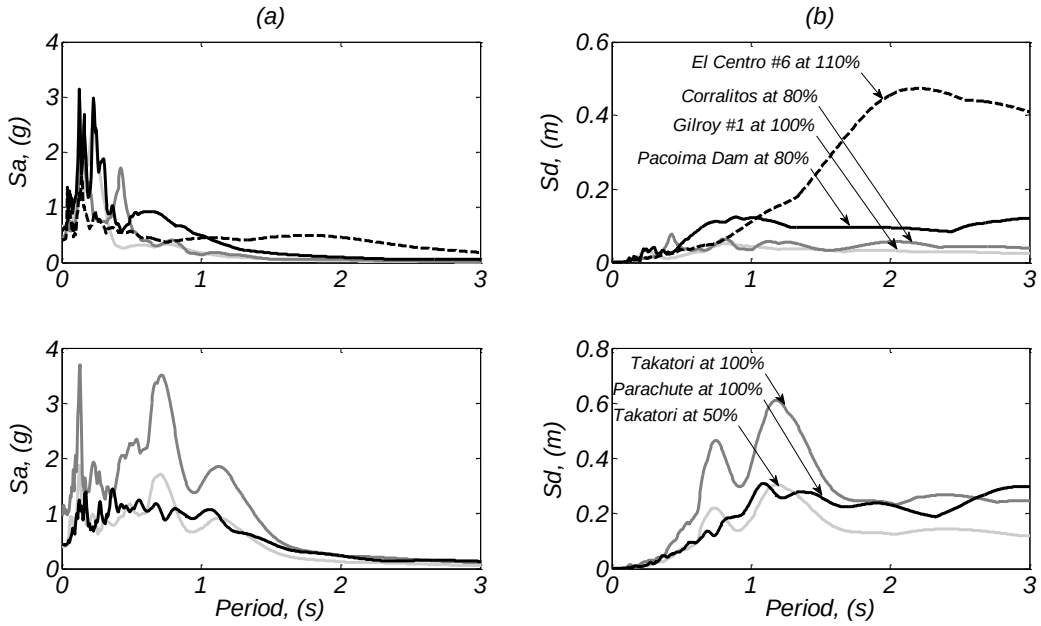

Figure 3.3. Linear elastic (a) acceleration and (b) displacement spectra for the recorded soil free-field acceleration at the elevation of the base of the foundation in the direction of shaking (damping ratio $\zeta = 3\%$).

3.8 Measured and Observed Response

3.8.1 Periods of vibration

Using data compiled from the white noise events before and after each motion, the fundamental period of each specimen was calculated as the period at which the amplification ratio of the acceleration response spectrum (ARS) of horizontal acceleration at the centroid of the mass in the direction of excitation to the ARS of the soil free-field acceleration was maximized. The resulting periods are shown in Figure 3.4. The theoretical fixed base fundamental period of the test specimens is 0.14 s (for uncracked concrete). Increased initial periods of the two specimens in Test Day 2 are attributed to the reduced achieved compaction of the footing backfill soil compared to Test Day 1 due to less moisture in the soil on Day 2. Minor concrete cracking along the height of the column due to the shaking of Test Day 1 also contributes slightly to the same phenomenon. Note that for Test Days 1 and 3, the fundamental period tended to increase after each shake due to rounding of the soil surface (i.e. concave down) under the footing during the rocking mechanism (Deng and Kutter 2012); this eventually reduced the effective contact area at the end of each record. For Test Day 2, the period remained almost constant because sand fell under the footings as it was looser and drier, and helped retain the soil-footing contact area near the edges that mainly contribute to the rocking stiffness of the foundation. The resulting soil surfaces under the aligned specimen after Test Days 1 and 2 are shown in Figure 3.5. Note that the falling sand near the East edge of the foundation during Test Day 2 created a gap between the footing and the soil near the center of the footing.

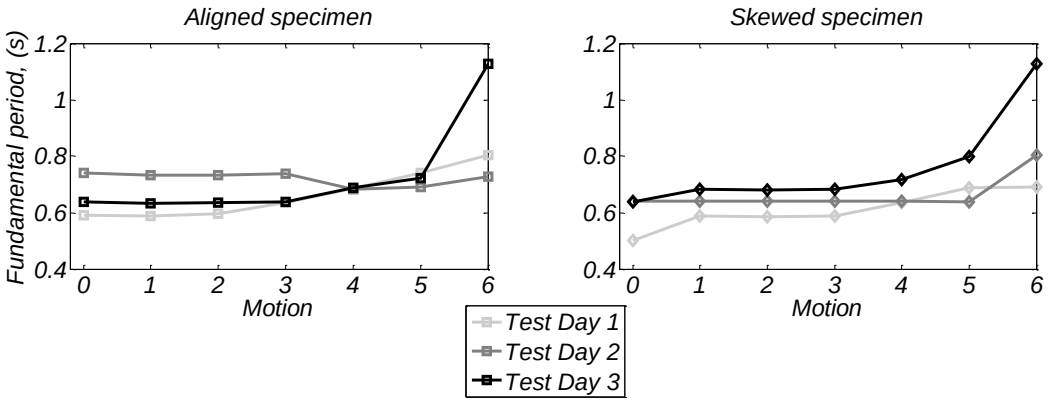

Figure 3.4. Fundamental period of specimens measured using white noise after each events (motion 0 refers to initial period).

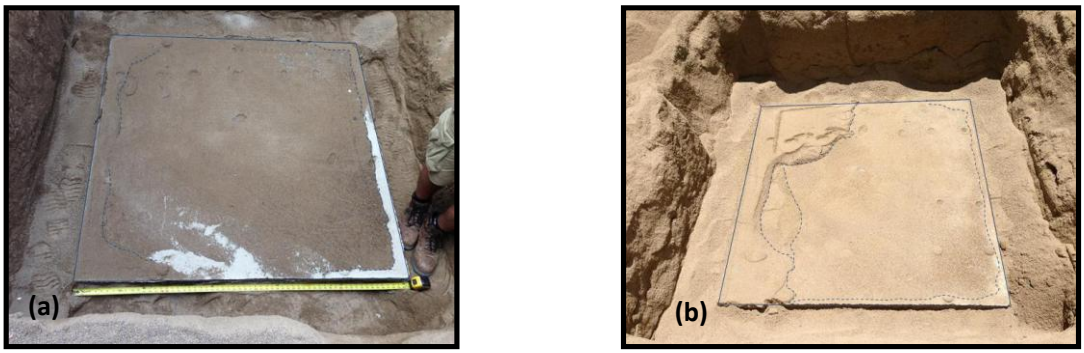

Figure 3.5. Falling sand area under aligned foundation after (a) Test Day 1; and (b) Test Day 2 (dotted lines were added for clarity). The North direction is at the bottom of these photos.

3.8.2 Lateral displacement response

Error! Reference source not found. summarizes peak responses for each of the ground otions in each of the three test days for the two specimens and includes: the peak drift ratio, $\Theta_{r,peak}$, defined as peak displacement (in any direction) at the centroid of the mass blocks divided by the height to the base of the footing, the cumulative residual drift ratio, $\Theta_{r,res}$, (in any direction), and the cumulative residual settlements, Δ_{res}, at the center of the base of the footings.

Figure 3.6 plots the drift ratio response histories in the direction of shaking for the two specimens for motion 4 (Pacoima Dam at 80%), 5 (Takatori at 50%), and 6 (Takatori at 100%). Note the significant residual rotations during Test Day 2 after motion 6. The skewed specimen exhibited smaller overall peak drift ratios and residual rotations.

The skewed specimen developed significant displacements in the out-of plane direction, compared to the aligned specimen which primarily responded along the

direction of shaking. The ratio of peak out-of-plane displacement to the in-plane one was 0.54, 0.36, and 0.22 in Test Days 1, 2, and 3, respectively for the Takatori at 50% motion. Cast concrete around the footing for Test Day 3 reduced significantly the out-of-plane rocking of the skewed specimen. After motion 6 (Takatori at 100%), the cumulative residual foundation twisting for Test Day 1, 2 and 3 was equal to 0.045, 0.052 and 0.014 rad, respectively. Figure 3.7 plots the mass trajectories of the mass of the skewed specimen due to foundation rotation in polar coordinates for motions 5 and 6.

For the aligned specimen, $\Theta_{r,res}$ was negligible (less than 0.1%) for the El Centro motion for all three test days for $\Theta_{r,peak}$ between 1.4% and 2.2%. For the Pacoima Dam motion with $\Theta_{r,peak}$ between 3.3% and 3.9%, $\Theta_{r,res}$ = 0.4%, 0.5%, 0.2% in Test Days 1, 2, and 3, respectively. For motion 5 (Takatori at 50%), the $\Theta_{r,peak}$ was between 5.9% and 6.9%, with $\Theta_{r,res}$ = 0.9%, 1.4%, and 0.5% in Test Days 1, 2, and 3, respectively. The smallest $\Theta_{r,peak}$ and $\Theta_{r,res}$ for all these three motions were measured during Test Day 3. The smaller $\Theta_{r,peak}$ observed in Test Day 3 was primarily attributed to the larger moment capacity of the foundation due to the weak concrete around the footings as explained below. This construction detail was also the reason that the $\Theta_{r,res}$ were much smaller on Test Day 3, compared to Test Day 1 and especially to Test Day 2 because the casted concrete prevented the clean sand (without cohesion) from falling under the footing. This effect became more pronounced during motion 6 (Takatori at 100%) where the corresponding residual rotations for Test Days 1 and 2 were 3.4% and 7.8% for peak rotations of 11.6% and 13.7%, respectively. This phenomenon can also be observed in the videos of the experimental response. Figure 3.8 shows snapshots from Test Day 2 from a camera located near the North-east corner of the aligned footing, after motions 4, 5 and 6.

The effect of the falling sand was also observed in the skewed specimen, but to a smaller extent. Up to the Pacoima Dam motion (motion 4), the peak and residual drift ratios were similar for all three test days. Specifically, the $\Theta_{r,peak}$ was less than 3.5%, while the $\Theta_{r,res}$ was less than 0.4%. For ground motion 5, Takatori at 50%, the peak drift ratio for Test Days 1, 2, and, 3 was 5.2%, 4.5%, and 5.7%, respectively. The corresponding residual drift ratios were 0.8%, 1.8%, and 0.9%. For motion 6 (Takatori at 100%), the peak drift ratios were 11.7%, 9.9%, and 10.9% for test days 1, 2, and 3, respectively, while the residual values were 2.0%, 2.2%, and 0.7%. Although the moisture loss was similar for both specimens prior to Test Day 2, hand compaction in the vicinity of the foundations was performed by different persons, which may have resulted in better compaction near the skewed specimen leading to smaller residual drifts when compared to the aligned specimen. In Test Day 3, the residual drift ratio of the skewed specimen increased only slightly to 1.1%, even after being subjected to three additional strong ground motions (motion 7 to 9) that resulted in $\Theta_{r,peak}$ up to 10.1%.

Table 3.2. Recorded peak and cumulative residual total column drift ratios and cumulative residual foundation vertical displacements. Positive values for vertical displacements indicate uplift; negative values indicate settlement.

		Aligned specimen									**Skewed specimen**								
		Test Day 1			**Test Day 2**			**Test Day 3**			**Test Day 1**			**Test Day 2**			**Test Day 3**		
No.	Motion name	$\Theta_{r,peak}$ (%)	$\Theta_{r,res}$ (%)	Δ_{res} (mm)	$\Theta_{r,peak}$ (%)	$\Theta_{r,res}$ (%)	Δ_{res} (mm)	$\Theta_{r,peak}$ (%)	$\Theta_{r,res}$ (%)	Δ_{res} (mm)	$\Theta_{r,peak}$ (%)	$\Theta_{r,res}$ (%)	Δ_{res} (mm)	$\Theta_{r,peak}$ (%)	$\Theta_{r,res}$ (%)	Δ_{res} (mm)	$\Theta_{r,peak}$ (%)	$\Theta_{r,res}$ (%)	Δ_{res} (mm)
1	Gilroy #1, 100%	0.7	0.0	0	0.9	0.0	-2	0.8	0.0	-2	0.7	0.0	0	0.7	0.1	-2	0.9	0.0	-2
2	Corralitos, 80%	1.0	0.1	-1	1.5	0.1	-3	1.1	0.0	-2	0.9	0.0	-1	1.0	0.1	-3	1.0	0.1	-3
3	El Centro #6, 110%	1.5	0.1	-2	2.2	0.1	-4	1.4	0.0	-3	1.3	0.1	-2	1.4	0.1	-3	1.5	0.1	-3
4	Pacoima Dam, 80%	3.7	0.4	-5	3.9	0.5	-5	3.3	0.2	-5	3.5	0.2	-5	3.4	0.3	-5	3.3	0.3	-6
5	Takatori, 50%	6.9	0.9	-8	6.9	1.4	-4	5.9	0.5	-8	5.2	0.8	-8	4.5	1.8	-3	5.7	0.9	-10
6	Takatori, 100%	11.6	3.4	-6	13.7	7.8	15	10.1	2.1	-13	11.7	2.0	-7	9.9	2.2	8	10.9	0.7	-17
7	Parachute, 100%	-	-	-	-	-	-	12.9	2.5	-11	-	-	-	-	-	-	9.7	0.8	-21
8	Parachute, -100%	-	-	-	-	-	-	8.8	2.7	-14	-	-	-	-	-	-	8.3	1.1	-24
9	Parachute, 110%	-	-	-	-	-	-	13.8	3.5	-12	-	-	-	-	-	-	10.1	1.1	-26

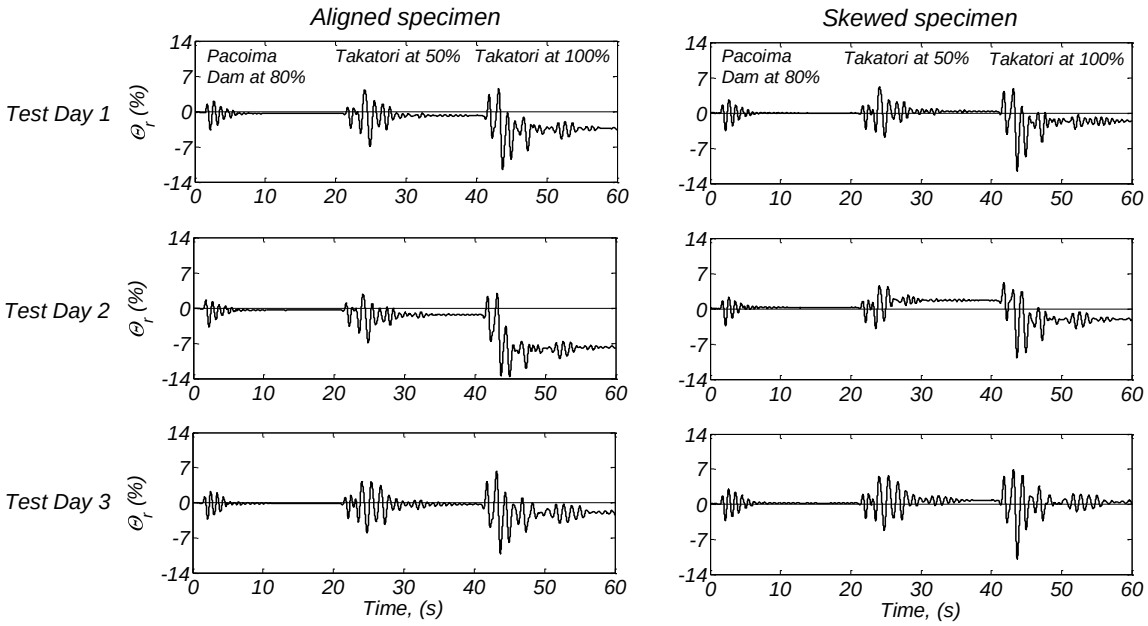

Figure 3.6. Recorded drift ratio response histories in the direction of shaking for motions 4, 5, and 6.

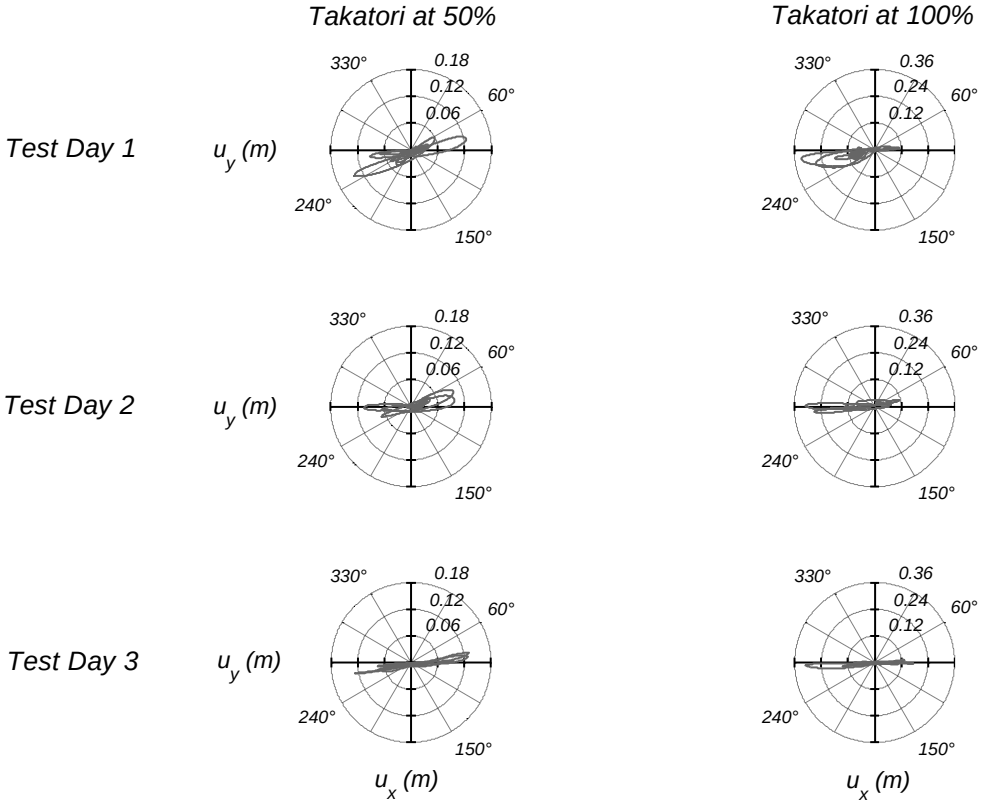

Figure 3.7. Mass trajectories in polar coordinates for the skew specimen due to foundation rotation for motions 5 and 6.

Figure 3.8. Snapshot from video camera located near the northeast corner of the aligned foundation during Test Day 2 after the end of; (a) motion 4 (Pacoima Dam at 80%), (b) motion 5 (Takatori at 50%), and (c) motion 6 (Takatori at 100%).

3.8.3 Hysteretic response

The moment of the foundation at the base center point of the footing was calculated using the measured linear and angular accelerations on the mass blocks and the footings including nonlinear geometry effects (P-Δ). Figure 3.9 and 3.10 show foundation moment versus foundation rotation, θ_f, in the direction of the excitation, for motions 5 (Takatori at 50%) and 6 (Takatori at 100%), respectively. As expected, the effect of the falling sand during Test Day 2 reduced re-centering capability but enhanced energy dissipation. Worth noting is that the foundations re-centered on Test Day 1 and especially in Test Day 3, even for large rotations. Although the weak concrete was separated from the footing using plastic sheets and joints were separating the weak concrete in four different monolithic blocks [Figure 3.2(d)], the weak concrete and the footing were interlocked together during rocking at the side near the contact area of the footing with the soil during large foundation rotations. As a result, the foundation moment capacity during the Test Day 3 was 1.28 times that of Test Day 1 and 2.

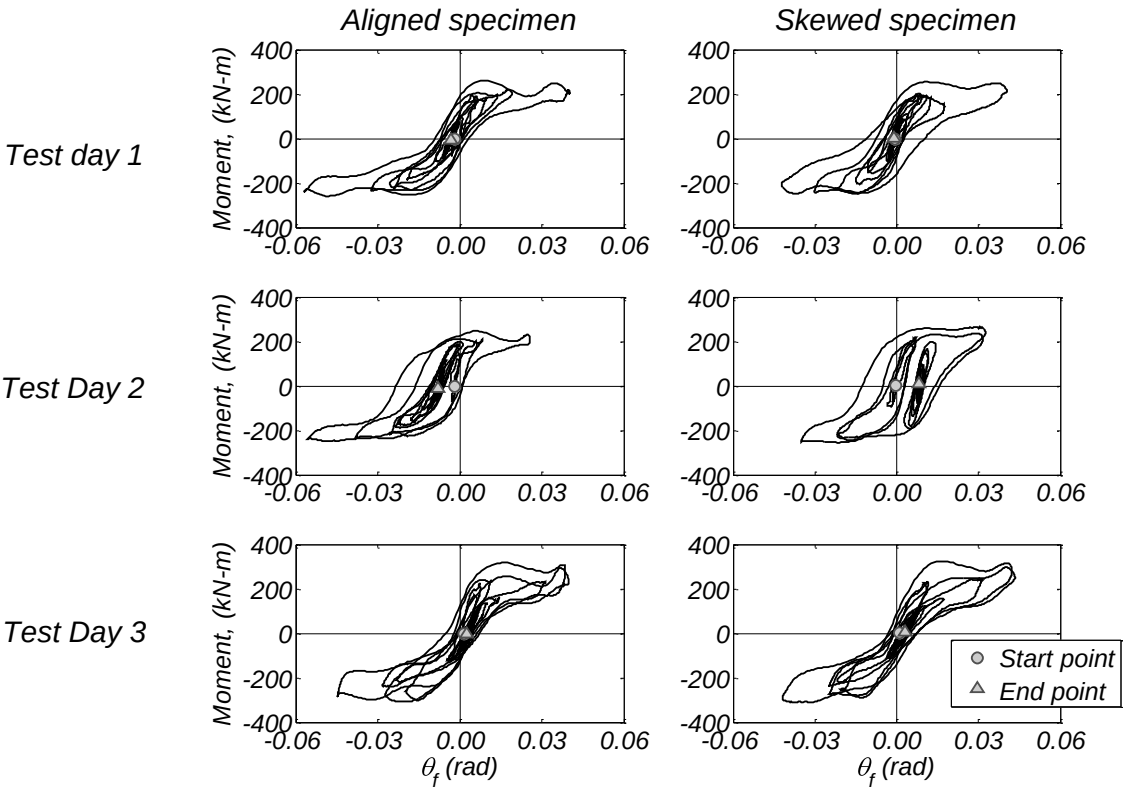

Figure 3.9. Recorded foundation moment-rotation diagrams for Takatori at 50%.

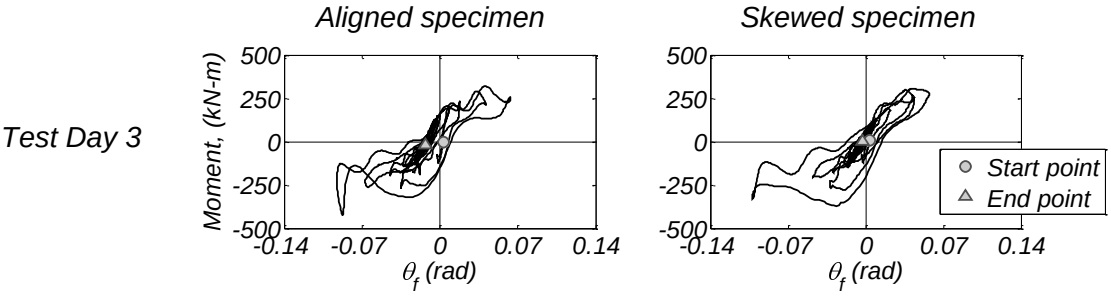

Figure 3.10. Recorded foundation moment-rotation diagrams for Takatori at 100% (Test Day 3 only).

3.8.4 Settlement response

The settlements presented and discussed here are total settlements since they include the free field soil settlement. The latter was monitored at a location near the middle of the south LSCB side during Test Days 2 and 3, and is discussed later. During Test Day 1, the settlement of the aligned foundation increased after each shake up to motion 5 (Takatori at 50%). After the last motion (Takatori at 100%), the cumulative residual settlement was slightly reduced from 8 to 6 mm, indicating that relative uplift of the base of the center of the foundation occurred during this motion. The same phenomenon was also observed for the skewed specimen, where the

settlements after motion 5 and 6 were 8 and 7 mm, respectively. Note that these values do not necessarily correspond to the soil surface under the center of the base of the footing, since a gap between the footing and the soil near the center of the foundation can be permanent after strong ground motions due to sand falling in under the perimeter of the footings.

The above phenomenon intensified during Test Day 2, when the settlements after motion 4 and 5 for the aligned specimen were 5 and 4 mm, respectively. The corresponding settlements for the skewed specimen were 5 and 3 mm. During the last shake (Takatori at 100%), the flow of sand under the one side of the footing was large enough so that uplift of the center of the base of the footing was observed, equal to 15 and 8 mm for the aligned and skewed specimens, respectively.

The low-strength concrete construction detail for the backfill adopted on Test Day 3 proved successful into preventing the sand from falling under the footings. As a result, the settlements of the foundations of both specimens essentially increased gradually after each consecutive shake. After motion 5 and 6, the settlements of the aligned and skewed specimens were 13 and 17 mm, respectively. These values correspond to 0.009*B* and 0.011*B*.

The corresponding foundation rotation-settlement responses for motion 5 (Takatori at 50%) are shown in Figure 3.11. For Test Day 3, the cumulative residual settlement even for very large peak rotations (0.13 rad) of the footing was 12 mm and 26 mm for the aligned and skewed specimen respectively, which corresponds to 0.008*B* and 0.017*B*.

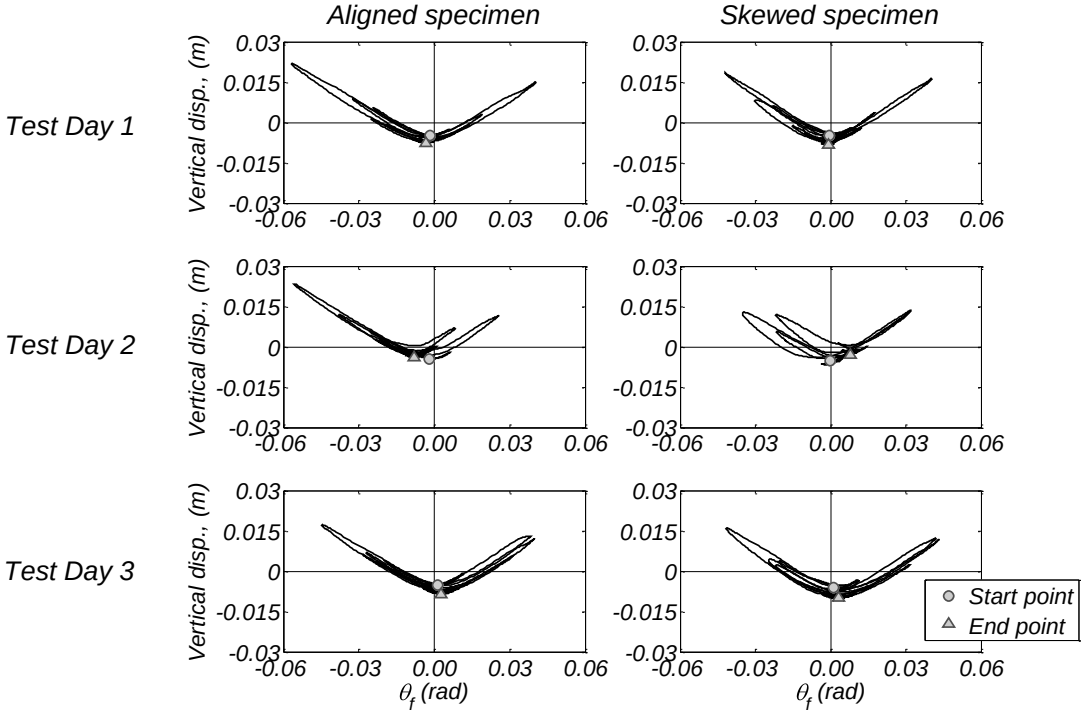

Figure 3.11. Recorded foundation settlement versus foundation rotation diagrams for Takatori at 50%.

3.8.5 Vertical acceleration effects

As shown in Equation 1, moment capacity of lightly-loaded footings is almost linearly dependent on their axial load. Therefore, vertical acceleration at the mass and the footing can induce foundation moment capacity variation due to altering the axial load. This mainly caused the

oscillations in the foundation moment response, shown in Figure 3.9 and 3.10, which are more significant for increasing ground motion intensity. Vertical accelerations were less than 0.3*g* in the Pacoima at 80% and Takatori at 50% motions, but accelerations were significantly larger in the Takatori at 100% motion. The vertical accelerations of the mass and the footings are mainly due to the impact of the specimen against the soil surface during the rocking motion.

To demonstrate this phenomenon, Figure 3.12 plots the foundation moment-rotation response of the aligned specimen for the Test Day 2 and motion 6 (Takatori at 100%), filtered at 8 Hz (low-pass) to remove high-frequency spikes and enhance clarity of this figure. The foundation moment is also plotted against the axial load calculated by the superposition of the gravity loads and the vertical load due to the recorded vertical accelerations of the mass blocks and the footing. The theoretical foundation moment capacities, for each axial load are also calculated and plotted; see $M^{+}_{c,foot}$ and $M^{-}_{c,foot}$ in Figure 3.12(b). Finally, the corresponding vertical acceleration response history of the mass is plotted in Figure 3.12(c). Starting from a positive foundation moment and rotation at time t = 15.29 s, the footing reverses passing through zero moment for a local peak positive moment at time t = 15.45 s. The impact of the footing with the soil at time t = 15.38 s results in a peak vertical acceleration of the mass equal to 0.56g (0.75g unfiltered), and as the vertical acceleration oscillates, so does the foundation moment; see points for time t = 15.56 s and t = 15.65 s. The period of the recorded vertical acceleration of the mass blocks is about 0.2 s (5 Hz). Despite the high vertical accelerations of the mass that were recorded in motion 6 (Takatori at 100%, Figure 3.13), no structural damage was observed in the columns.

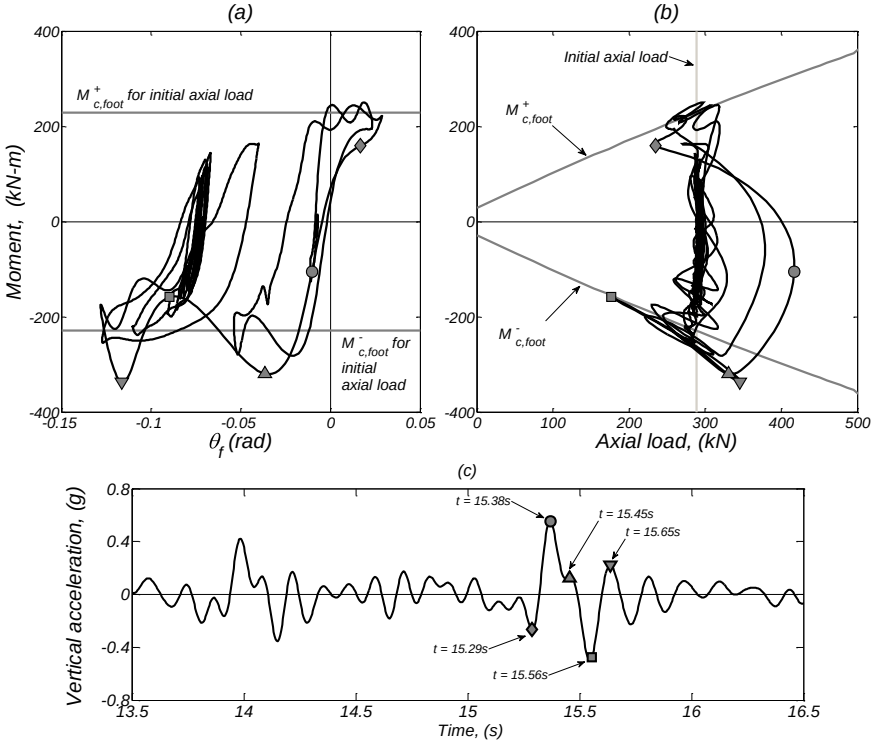

Figure 3.12. Foundation moment versus (a) rotation and (b) axial load for the aligned specimen in Test Day 2 and motion 6 (Takatori at 100%). (c) Vertical acceleration response history for the centroid of the mass blocks. The foundation moment, axial load and vertical acceleration are filtered at 8 Hz (low-pass).

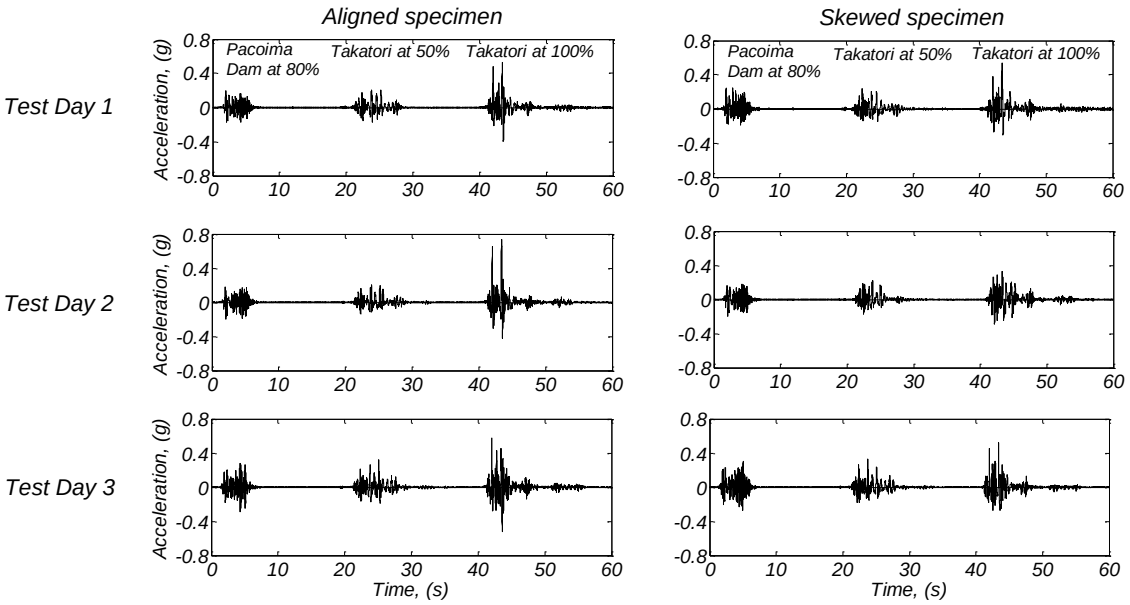

Figure 3.13. Measured vertical acceleration time histories at the centroid of the mass blocks for motions 4, 5, and 6.

3.8.6 Rotatory mass effects

The angular accelerations of the mass blocks impose moment demands at the top of the column which although do not change the foundation moment capacity, they affect the moment demand distribution along the height of the column. Using the linear and angular accelerations of the mass blocks, the moment was calculated for different locations along the height of the column, see Figure 3.14. The peak recorded moment at the base of the column was equal to 247 kN-m (skewed specimen and motion 6). The peak calculated moment at the centroid of the mass blocks was equal to 110 kN-m, which is equal to 48% of the foundation design moment of the aligned specimen.

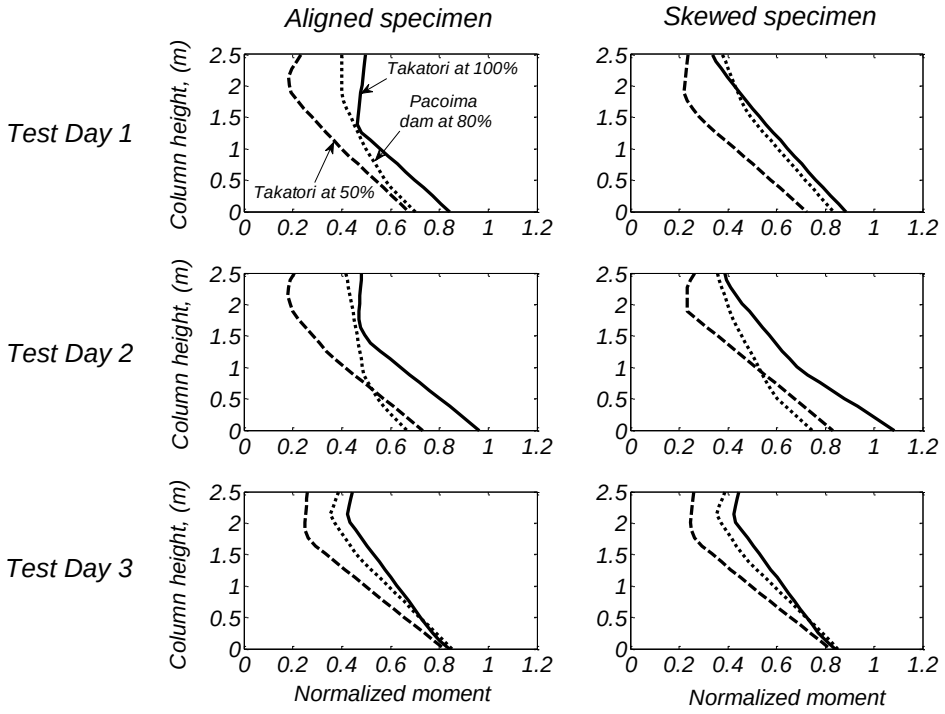

Figure 3.14. Envelopes for the recorded moment along the height of the column for motions 4, 5, and 6. The moment is normalized by the foundation design moment of the aligned specimen (229 kN-m).

3.8.7 Damage in the soil away from the foundations and structural damage

The water table elevation was varied to investigate the effect of a nearby water table, and liquefaction was not expected to be significant due to the relative density being 90%. Pore pressure transducers confirmed this expectation; the maximum recorded excess pore pressure during shaking at the free-field being 6.3% of the effective overburden stress. The observed very small excess pore water pressures are attributed to the high relative density of the sand; incomplete saturation and shaking of the foundation soil in prior shaking events may also have contributed to the small pore pressure ratios. A vertical string potentiometer placed at a distance away from the two specimens showed a cumulative settlement of 1.4 and 0.2 mm for Test Day 2 and 3, respectively. The specimens sustained no structural damage and only minor concrete cracking was observed in the lower part of the columns during the rocking of the foundations. These cracks were momentarily observed by the video recordings and they were fully closed at the end of first two tests. During Test Day 3, the moment demand of the column was larger as explained above, resulting in some minor cracks observed near the base of the column that remained visible after the end of the shaking.

3.9 Conclusions

Two 460-mm-diameter columns fixed on 1.52-m-square rocking shallow foundations were tested at the NEES@UCSD shake table. The specimens were placed inside a stiff soil confining box on

top of 2.7 m of well-compacted clean sand with $D_r \approx 90\%$; the embedment depth of the foundations was 0.66 m. One specimen was aligned and the other was placed in a skewed configuration with respect to the uniaxial direction of shaking. The experimental program included three test days with different groundwater elevations and different backfill conditions around the sides of the foundations. Up to nine ground motions were used for each test day. Negligible pore pressures developed in the sand during shaking; differences in the response of the specimens between test days are solely attributed to the effect of the footing backfill conditions. Conditions considered were as follows: no ground water table with wet footing backfill soil, with 1.2 m ground water and almost dry backfill soil, and 0.6 m ground water below the foundations with weak concrete cast around the sides of the footings. The following conclusions are drawn:

1. The rocking foundations achieved response objectives very successfully. They accommodated earthquake-induced lateral displacements corresponding to drift ratios between 3.3% and 5.9% with no structural damage and minimal residual drift ratios (0.1% and 0.3%, respectively). These values of drift ratio are similar to those expected for the DE and MCE level of shaking at a near-fault site 3 km from the Hayward fault (Antonellis and Panagiotou 2014). Cosmetic structural damage developed in both columns after 18 different ground motions, 7 of which produced system drift demands greater than 10%.

2. Consistent with previous observations from centrifuge model tests (Gajan and Kutter 2008; Deng et al. 2012a), loose and dry cohesion-less backfill can fall under gaps appearing on the side of the footing during the foundation rocking, potentially resulting in significant residual drifts. Residual drifts induced by this mechanism were small for peak drift ratios smaller than 6.9% but increased significantly for larger peak drift ratios. The residual drifts were small in Test Day 1, when the backfill soil was moist and did not slide as easily into the gap under the rocking foundation. Residual drifts were much larger on Day 2, when the backfill sand was relatively dry.

3. Casting of weak concrete around the footings for Test Day 3 was successful in minimizing material falling under the footing, which led to minimal residual drifts for peak drift ratios up to 5.9% and small residual drift ratios for peak drift ratios up to 10%. The moment capacity of the foundations backfilled with weak concrete was about 28% greater than the foundations with sand backfill, possibly due to interlocking of the footing and the weak concrete during large foundation rotations.

4. Sand falling under the foundation during the uplifting mechanism reduced settlements and enhanced energy dissipation; however, it also reduced the re-centering tendency. Sand falling under the edges of the rocking footing kept the edges of the footing in contact with the soil, which helped to maintain the rocking stiffness of embedded foundations. Without sand falling under the edges of the foundation, degradation of stiffness was apparent. The degradation of stiffness can be explained by the formation of a rounded soil-foundation interface during rocking; see Deng and Kutter (2012).

5. Vertical accelerations up to 0.75g (with 5 Hz predominant frequency) induced by the rocking mechanism were recorded in the Takatori at 100% motion that produced drift ratios more than 10%. For the Takatori at 50% motion, that produced footing rotations greater than 5%, the vertical accelerations were less than 0.3g. The cause of the vertical acceleration is the impact of the footing as the gap between the soil and footing closes during rocking. These accelerations cause a corresponding increase of the axial load of the columns, as well as oscillations in the moment resistance of the foundations.

6. The angular accelerations of the mass blocks imposed moment at the top of the columns that were up to 48% of the foundation design moment of the aligned specimen. Rotatory inertia effects in general increased with increase of peak drift ratio.

Chapter 4: Modified Modeling Scheme for Rocking Shallow Foundations

4.1 Introduction

This chapter presents a proposed modified numerical scheme for the modeling of rocking shallow foundations designed with high A/A_c ratios using Winkler springs. The modeling is scheme is based on the Winkler scheme proposed by Harden et al. (2009) and it was used in numerical models in Chapter 2 of this dissertation (see Figure 2.4).

Harden et al. (2009) used data mainly from centrifuge tests and limited large scale cyclic tests for the calibration of beam-on-nonlinear-Winkler-springs model. The majority of those tests included rocking shallow foundations with small values of factor of safety against vertical loads and small A/A_c ratios. This model was also developed for 2D analyses, and therefore a large number of Winkler springs were used for the modeling of underlying soil (50-100). Another drawback of the model proposed by Harden et al. (2009) is the estimation of the stiffness capacities of the Winkler springs based on the initial shear modulus of the soil G_0. The value of the peak shear modulus of the soil is hard to estimate and often unknown to the designer, during the preliminary analysis stages.

Recent studies by Deng et al. (2014) showed that the initial rocking stiffness, K_{init}, can be estimated as a function of the foundation moment capacity, M_r. More specifically they propose to use a value between $230M_r$ and $460M_r$, with a good match for design purposes equal to $300M_r$. This stiffness is in fact the secant stiffness of the foundation moment-rotation diagram of the rocking foundation at the point where 50% of the foundation moment capacity, M_r, is mobilized. Although this stiffness is used as the initial stiffness of a proposed simplified trilinear moment rotation model, the term is "initial" is kept here for consistency. The definition of the rocking stiffness as a function of the rocking moment capacity eliminates the need of the estimation of the shear modulus of the soil. Additionally, it is practically useful during the preliminary stages of the design, since it gives a direct relationship between the strength and the stiffness of the rocking foundations. For example, during the modeling of a bridge system the designer can estimate the required strength (and therefore stiffness) of the bridge columns using rocking foundations in order to limit the peak displacements without the need for detailed calculations of the foundation width, strength and stiffness of the underlying and soil.

4.2 Proposed Modeling Scheme for Rocking Shallow Foundations with High A/A_c Ratios

In this section the proposed model is presented, and the differences with the model by Harden et al. (2009) are identified. The main modifications are the following; (i) the uniaxial material

QzSimple1 is modified to further reduce the tensile stiffness which can create artificial tensile stresses during large rotations (for example when the overturning mechanism needs to be studied), (ii) the length of the end zone is defined by the A/A_c ratio, (iii) the capacity of the springs at the end zone areas is defined by the actual soil capacity during rocking, (iv) the stiffness of the end zone springs is calibrated so that the rocking stiffness at $0.50M_r$ is equal to K_{init} (usually taken as $300M_r$ as explained above), and (v) the stiffness and capacities of the vertical springs of the middle zone are defined as a function of the ones at the end zones.

4.2.1 Modified QzSimple1 uniaxial material

The current implementation of the QzSimple1 material in OpenSees has incorporated a small tensile stiffness for numerical purposes. More specifically, the tensile stiffness is 0.001 times the initial compression stiffness. Although this modeling assumption may cause no problem for small foundation rotations and uplifts, it can introduce tensile forces during large rotations. These tensile forces are larger in the end zones where the uplift is large, and increase the moment capacity of the model. This effect becomes more important on footings with large A/A_c ratios under large rotations. Large A/A_c ratios inherently imply competent soil conditions with increased stiffness and strength, and therefore the corresponding Winkler springs are also very stiff in compression. When the overturning response of columns with rocking foundations is studied the effect of the tensile stiffness can be even more important.

The modified QzSimple1 has a tensile stiffness equal to 10^{-6} times the initial compression stiffness. The numerical simulations showed that this ensures that no artificial hardening moment hardening is recorded even under large foundation rotations, and at the same time the model is numerically stable.

4.2.2 End zone length

The length of the end zone is proposed to be equal to the corresponding critical contact area length. This is a rational assumption and can simplify the accurate modeling of the moment capacity, as mentioned later. For example, a rocking foundation with A/A_c ratio equal to 8 has an end zone length equal to (1/8) $B_f = 0.125B_f$, where B_f is the foundation width. Harden et al (2009) use an end zone length ratio as a function of the foundation dimensions, in order to accurately model both the initial vertical and rocking stiffness. For a square foundation, this results to a corresponding end zone length equal to $0.15B_f$. It should be noted, that the accurate modeling of both the vertical and rocking stiffness is important for cases with small foundation rotations and no uplift, such as when including the foundation flexibility in the modeling of conventionally designed structures. In cases where the rocking foundation is used as a main mechanism to resist earthquake loads, the footings are expected to respond well beyond the elastic limit and eventually to uplift, and as a result the initial vertical and rocking stiffness become less significant.

4.2.3 End zone springs

The properties of the end zone springs are presented in this section. The number of the end zone springs is less critical than the number of the middle zone springs, in contrast to the modeling scheme proposed by Harden et al. (2009). The main reason is that the end springs are expected to yield and reach their ultimate capacities during the rocking mechanism. Therefore, how many springs are used is not very important since the resultant force and the centroid of this force is defined by the A/A_c ratio and is explicitly modeled, as described below.

4.2.3.1 Capacity

The capacity of the end zone springs, Q_{sr}, is simply the capacity of the soil when the footing is on minimum contact with the underlying soil during the rocking mechanism. In initial stages of the design the soil capacity is estimated using some assumed or determined site specific soil properties, mainly the critical shear angle φ_{cv}. The determination of the A/A_c ratio and the corresponding soil capacity is an iterative procedure and it was described in Chapter 2. In a preliminary design stage, the A/A_c ratio can first be estimated, and the soil capacity is then back-calculated as the total weight of the specimen divided by the critical contact area A_c.

4.2.3.2 Stiffness

The stiffness of the soil springs at the end regions, K_{sr}, is determined using an iterative procedure. The aim of this procedure is to achieve the required rocking stiffness K_{init} at the point where 50% of the foundation moment capacity, M_r, is mobilized, as described above. A simple "pushover" analysis in terms of applied moment is performed on the numerical model and the stiffness of the end zone springs is adjusted until the secant moment-rotation stiffness at $0.50M_r$ is equal to K_{init}. A small number of iterations (in the order of 5) is usually sufficient to achieve a secant rocking stiffness at $0.50M_r$ within 1% of the target K_{init}.

4.2.4 Middle zone springs

The properties of the middle zone springs are defined as a function of the spring properties of the end zone. More specifically they are determined through the K_{ratio} and Q_{ratio} which are defined as the ratio of the initial stiffness (or capacity) of the end zone springs to that of the middle zone springs respectively. Although more research is underway in order to provide guidelines for the selection of the appropriate K_{ratio} and Q_{ratio} values, the calibration using only the large scale shake-table tests (Antonellis et al. 2015) is presented here. The effect of these two values is important for capturing correctly the settlement response and the overall shape of the nonlinear moment-rotation diagram of the rocking shallow foundation, without changing the actual nonlinear force-displacement relation of the QzSimple1 uniaxial material. The shape of the moment-rotation loop is critical for the accurate modeling of the hysteretic damping in nonlinear time history analyses.

4.2.4.1 Capacity

As mentioned above, the capacity of the middle zone springs is defined as $Q_{sm} = Q_{sr}/Q_{ratio}$. Preliminary analyses using the large scale shake table test date indicate that values between 1 and 3 are appropriate for capturing accurately the hysteretic response of the rocking foundations. A Q_{ratio} value equal to one corresponds to uniform capacity of the springs along the foundation width. Although this may sound counter-intuitive, since the soil capacities are related to the shape and size of the contact area, it should be noted that since the foundation is designed with high A/A_c ratios, the soil springs along the middle section of the footing will never utilize their actual capacities. If the capacity of the springs near the middle part of the foundation is not artificially reduced, the resulting settlements are zero, since the total axial load of the foundation can be supported in a relatively small area of the total footing area. It should be noted that the QzSimple1 (type 2 for sand) springs are essentially elastic up to 25% of their capacities. It is therefore obvious that the modeling of the middle section springs needs to be adjusted for foundations with A/A_c ratios larger than 4, in order to capture some residual settlements that are expected during the rocking mechanism.

4.2.4.2 Stiffness

The stiffness of the middle zone springs, K_{sm}, is defined as $K_{sm} = K_{sr}/K_{ratio}$. Similarly to the discussion above, once the middle zone springs are artificially allowed to respond beyond their elastic limit, their actual stiffness will determine the value of the peak and residual settlement. Although more research is underway, using data from many centrifuge and a few large scale tests of rocking foundations, the calibration against the large scale shake table test indicates that a value between 5 and 10 is appropriate for the modeling of rocking foundations with similar A/A_c ratios (~ 12).

4.2.5 Damping coefficient

The radiation damping can be explicitly modeled using the QzSimple1 springs. No modification was required compared to the Harden et al. (2009) method. The damping coefficients, *c*, are determined using the elastic rocking damping coefficients by Gazetas (1983), using the secant period at the point where 50% of the foundation moment capacity, M_r, is mobilized. A uniform distribution of the damping coefficient along the width of the foundation is assumed.

4.2.6 Extension to 3D

The above methodology was presented for the 2D case, and therefore the A/A_c ratio corresponds to the B_f/B_c ratio, where *Bf* is the foundation width and B_c is the length of the critical contact area. The proposed modeling scheme can be easily extended into 3D cases, as shown in Chapter 2. The lengths of the end zone regions, the calibration of the stiffness properties of the springs of the end zone regions etc. can be calculated for each of the two main directions independently. For square footings, a symmetric model along the two main directions can be assumed, as shown in the next chapter. Please note that the behavior of the footing under a direction different than the two main directions for which the model is calibrated will be less accurate.

4.3 Comparison between the Proposed Modeling Scheme and the Large Scale Shake-Table Test Results

The modified modeling scheme which was presented above was used for the simulation results shown in this section. The results for two cases are presented; (i) $K_{ratio} = 5$, and (ii) $K_{ratio} = 10$. The Q_{ratio} for both cases was equal to 2. The numerical response of the aligned specimen subjected to the as recorded free-field soil acceleration of the Test Day 1 is plotted against the recorded responses. Figures 4.1 to 4.12 plot a variety of critical response parameters for earthquake motions 1 to 6. For each earthquake, one plot for each K_{ratio} is shown. Each figure plots the following; (i) lateral acceleration time history, (ii) vertical acceleration time history, (iii) foundation moment time history, (iv) drift ratio time history, (v) foundation rotation time history, (vi) foundation settlement time history, (vii) foundation moment-rotation diagram and (viii) foundation rotation-settlement diagram. Figures 4.13 and 4.14 plot the computed peak drift ratio, residual drift ratio and residual settlements against the recorded ones for all earthquakes, for K_{ratio} equal to 5 and 10 respectively. For both models a value of $K_{init} = 300M_r$ was assumed, and a sequential run of all six earthquakes was computed using sufficient time between each motion to damp out the free vibration parts.

The effect of the K_{ratio} on the shape of the moment rotation diagram and the settlement response becomes apparent from the figures below. The case with $K_{ratio} = 5$ captures correctly the

peak settlement for the motion 1, but underestimates the settlements for the remaining earthquakes. On the other hand, the case with K_{ratio} = 10, overestimates the settlements for the first ground motion but captures very well the overall settlements for motions 2 and 3 and with reducing accuracy for the remaining motions. The shape of the moment rotation diagram is captured well for both cases.

The time history responses demonstrate that both cases manage to capture the stiffness softening during the rocking mechanism under medium to strong cases. For the first earthquake, where only limited uplift was recorded, it becomes apparent that the initial rocking and vertical stiffness is important, as shown by the phase lag of the free vibration parts. For earthquakes with moderate and large rotations though the modified modeling scheme provides excellent agreement for both cases. The foundation moment capacity is also very accurate for both models, since the end region lengths and the capacities of the end region springs are explicitly modeled to match the experimental results.

It is shown that the Winkler-type spring models can not accurately capture the residual drift ratios of the rocking foundations. The reason for that is mainly that the force-displacement relation of each Winkler spring is independent of the state of the surrounding springs. Coupled vertical Winkler springs could solve this problem but they are beyond the scope of this study. It should be noted that current design code provisions and performance based evaluation techniques usually correlate the residual drift ratios to the ultimate peak drift ratios, and Deng et al. (2014) have provided similar data specifically for rocking foundations.

The differences of the numerical simulation and the experimental results in motion 6 are due to the flow of sand under the uplifting side of the footing. Since rocking foundations are expected to be especially detailed to prevent this phenomenon, the Winkler type models do not need be modified further.

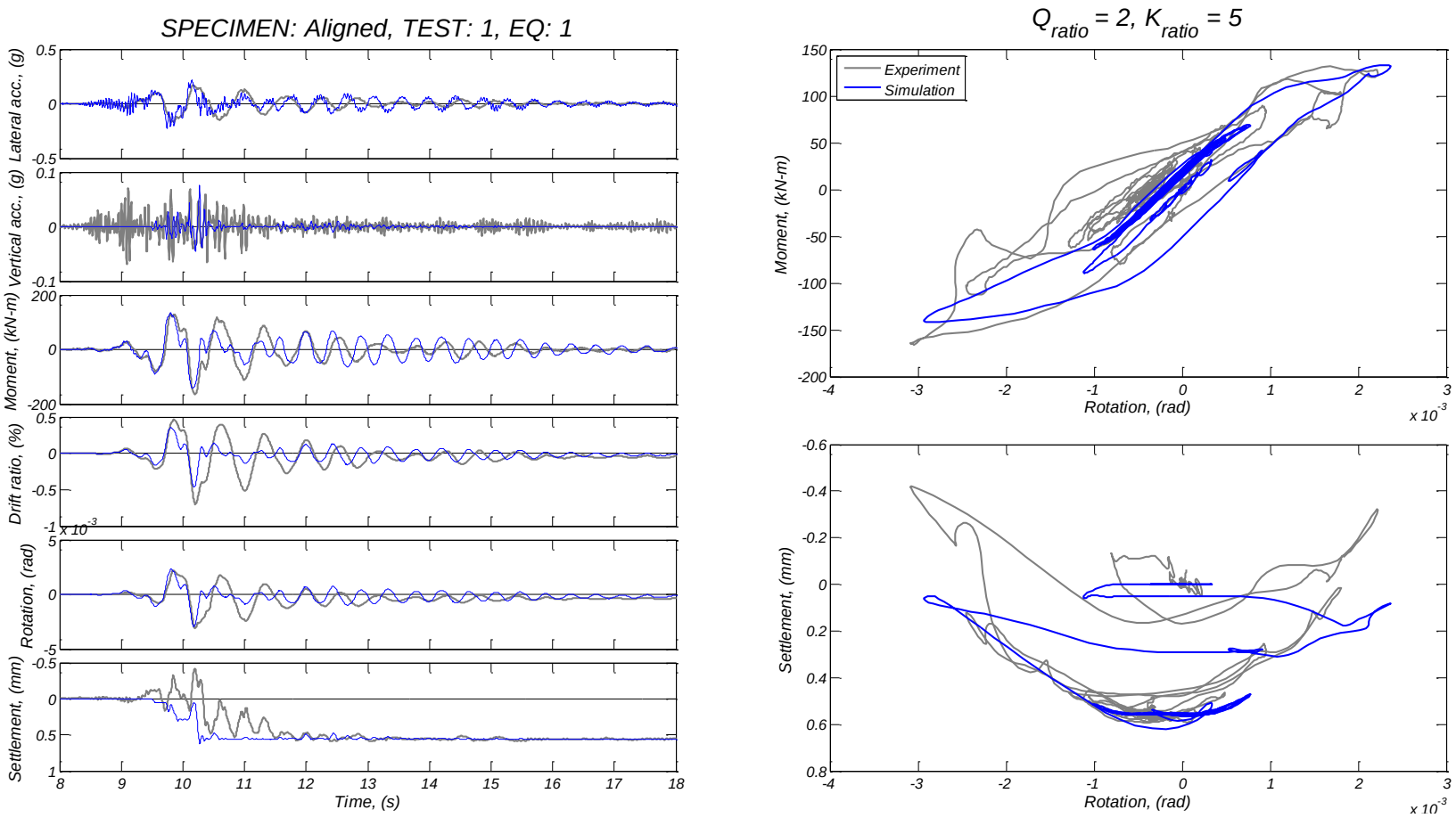

Figure 4.1. Comparison between experimental and numerical simulation results (K_{ratio} = 5) for the aligned specimen, Test Day 1, motion 1.

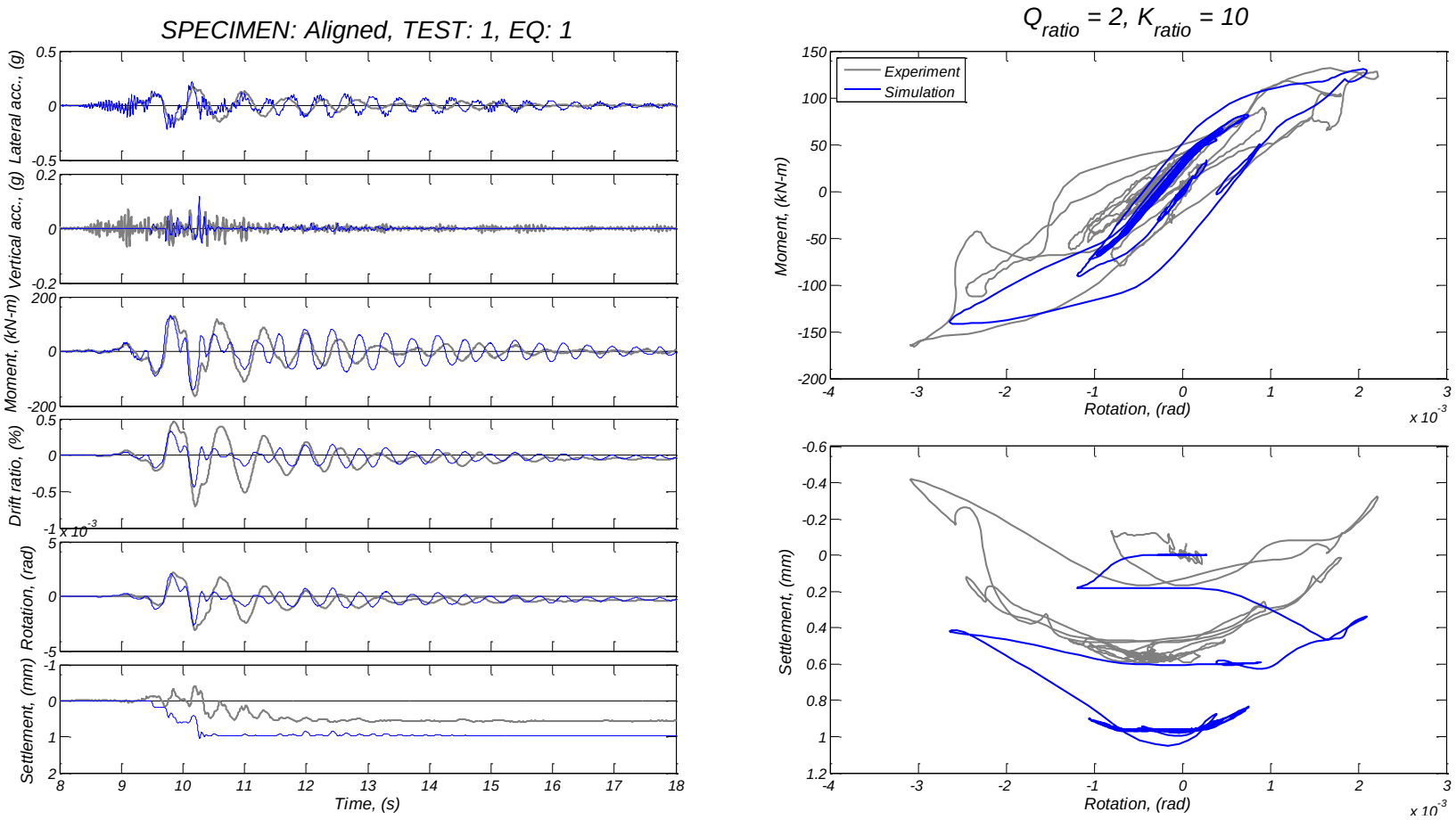

Figure 4.2. Comparison between experimental and numerical simulation results (K_{ratio} = 10) for the aligned specimen, Test Day 1, motion 1.

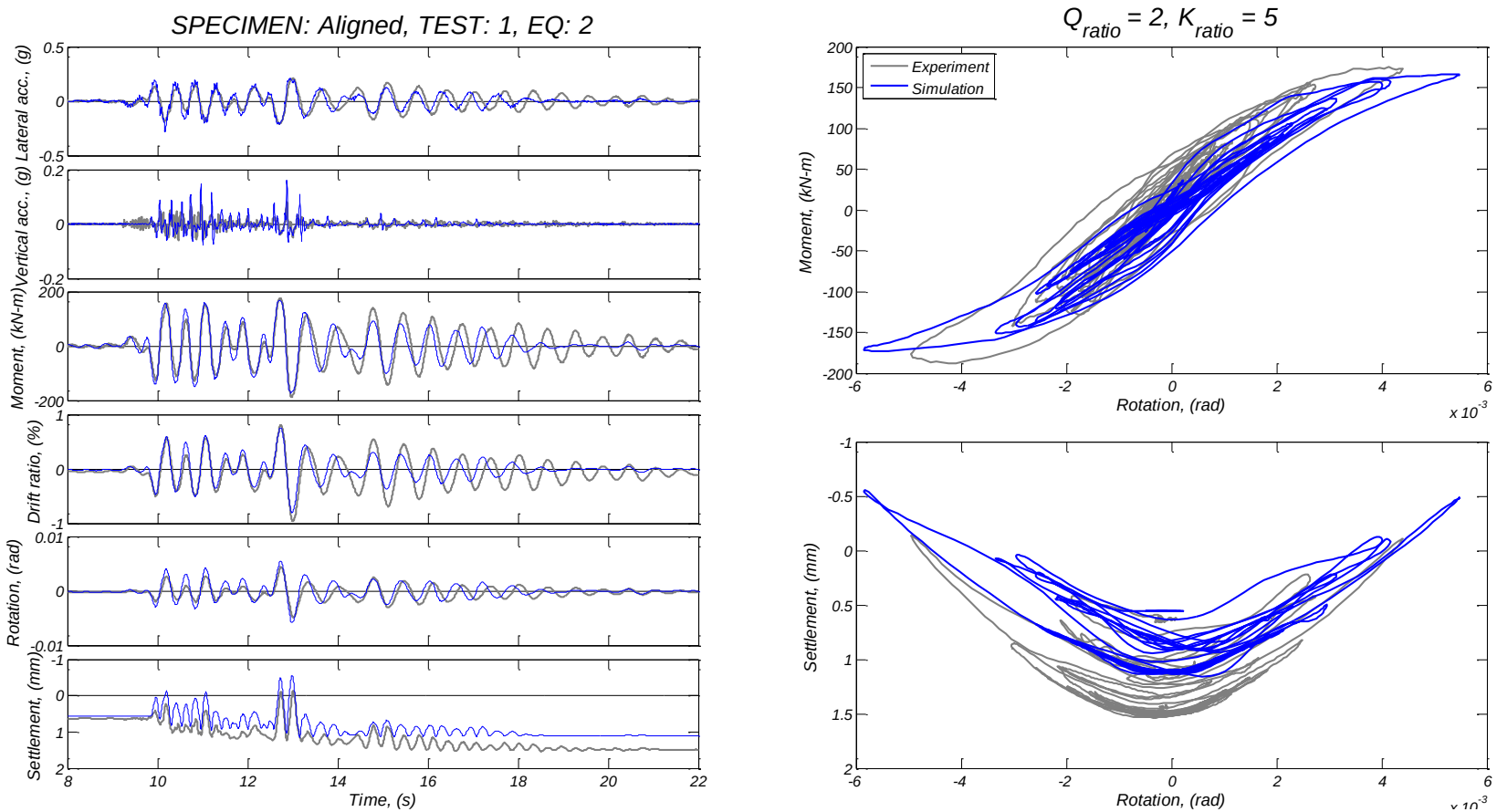

Figure 4.3. Comparison between experimental and numerical simulation results (K_{ratio} = 5) for the aligned specimen, Test Day 1, motion 2.

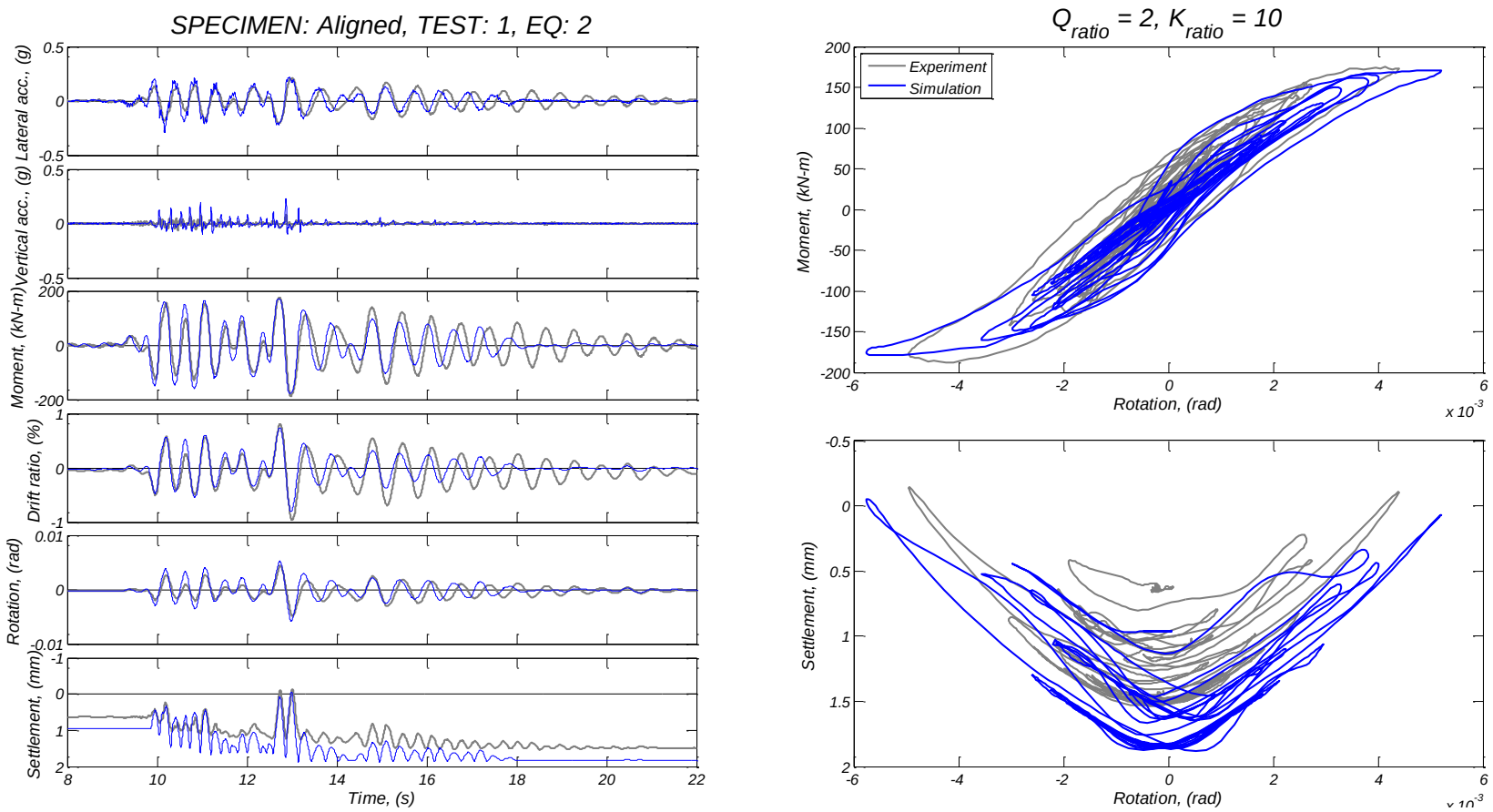

Figure 4.4. Comparison between experimental and numerical simulation results (K_{ratio} = 10) for the aligned specimen, Test Day 1, motion 2.

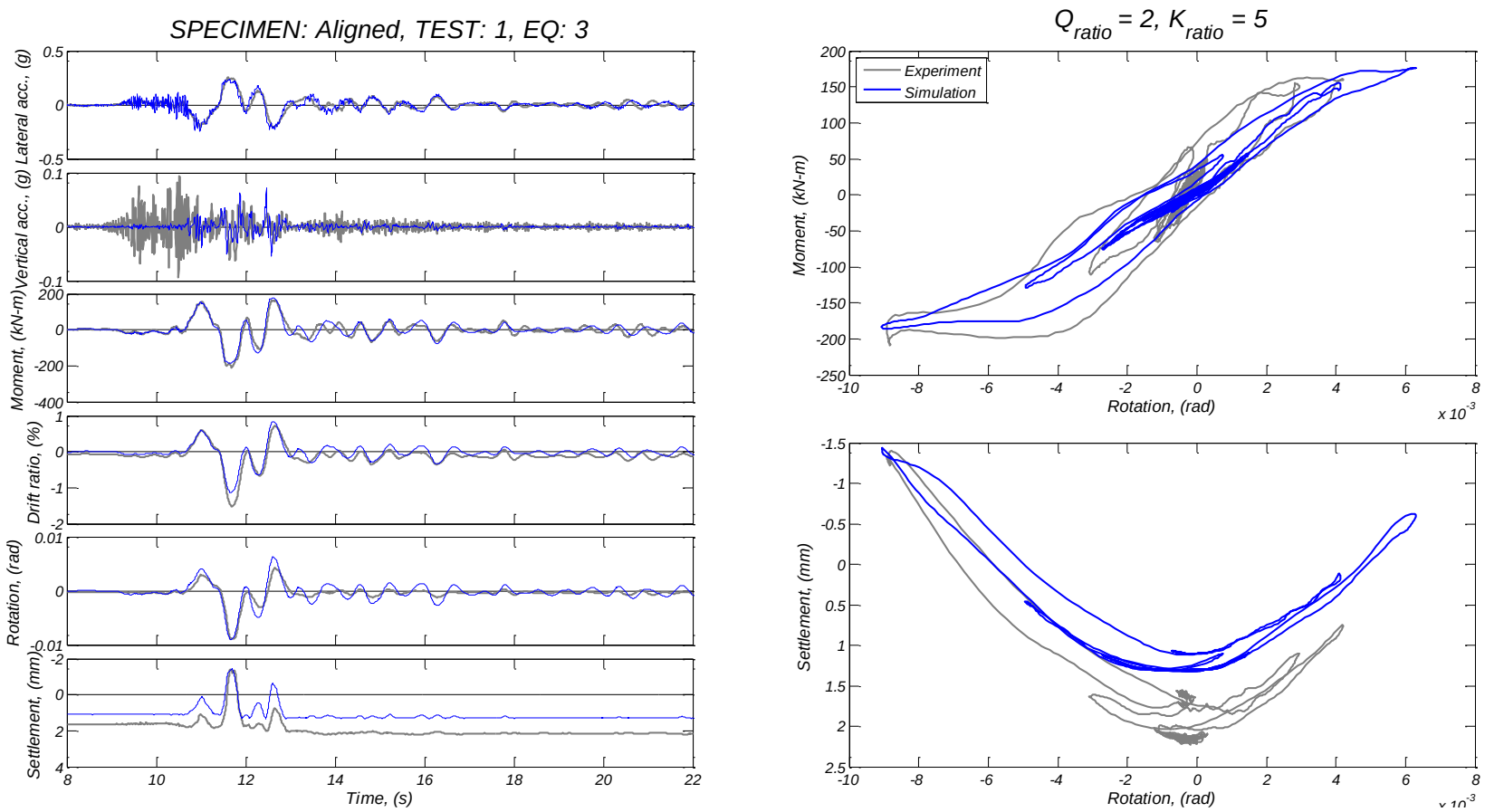

Figure 4.5. Comparison between experimental and numerical simulation results (K_{ratio} = 5) for the aligned specimen, Test Day 1, motion 3.

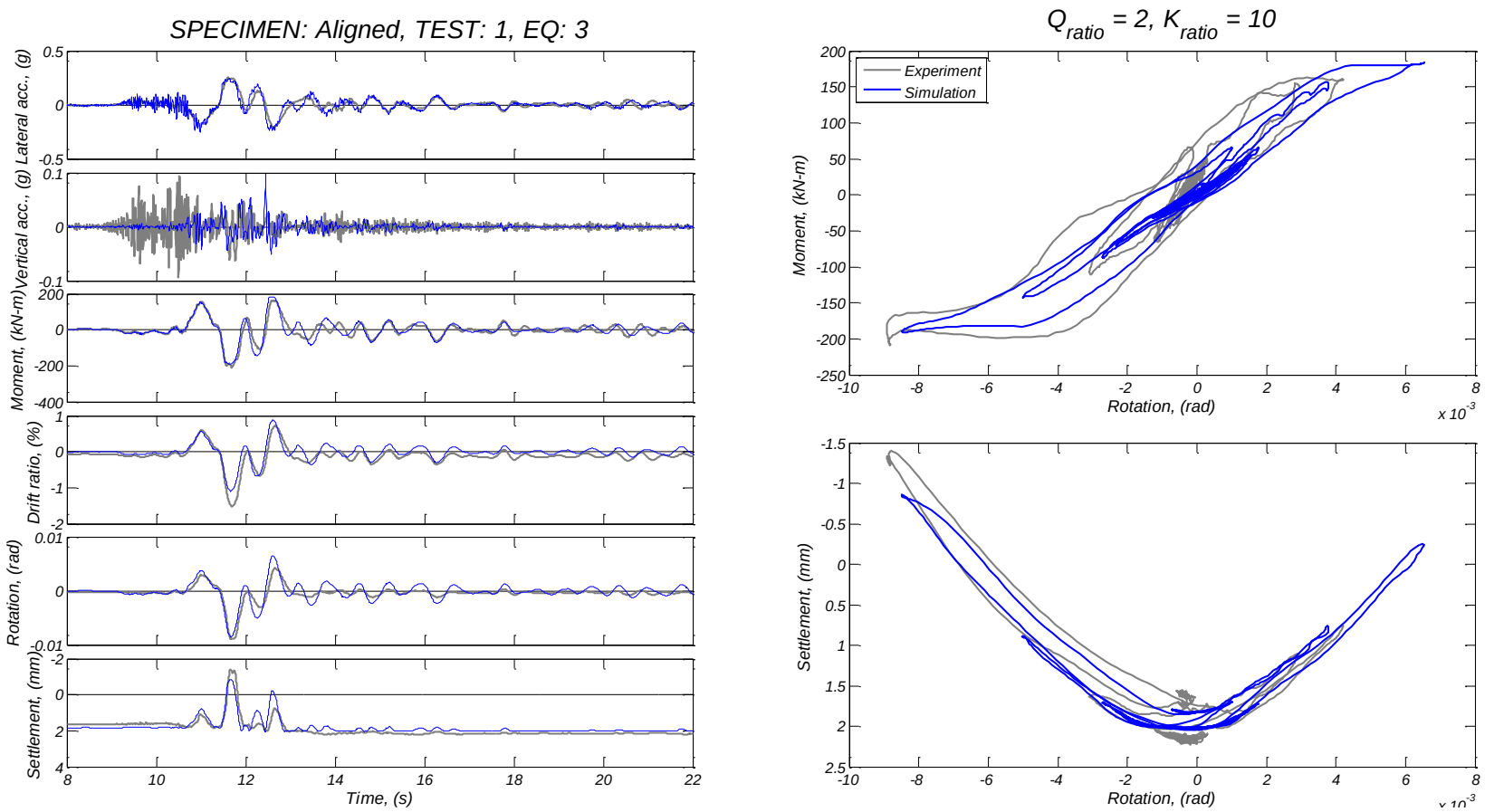

Figure 4.6. Comparison between experimental and numerical simulation results (K_{ratio} = 10) for the aligned specimen, Test Day 1, motion 3.

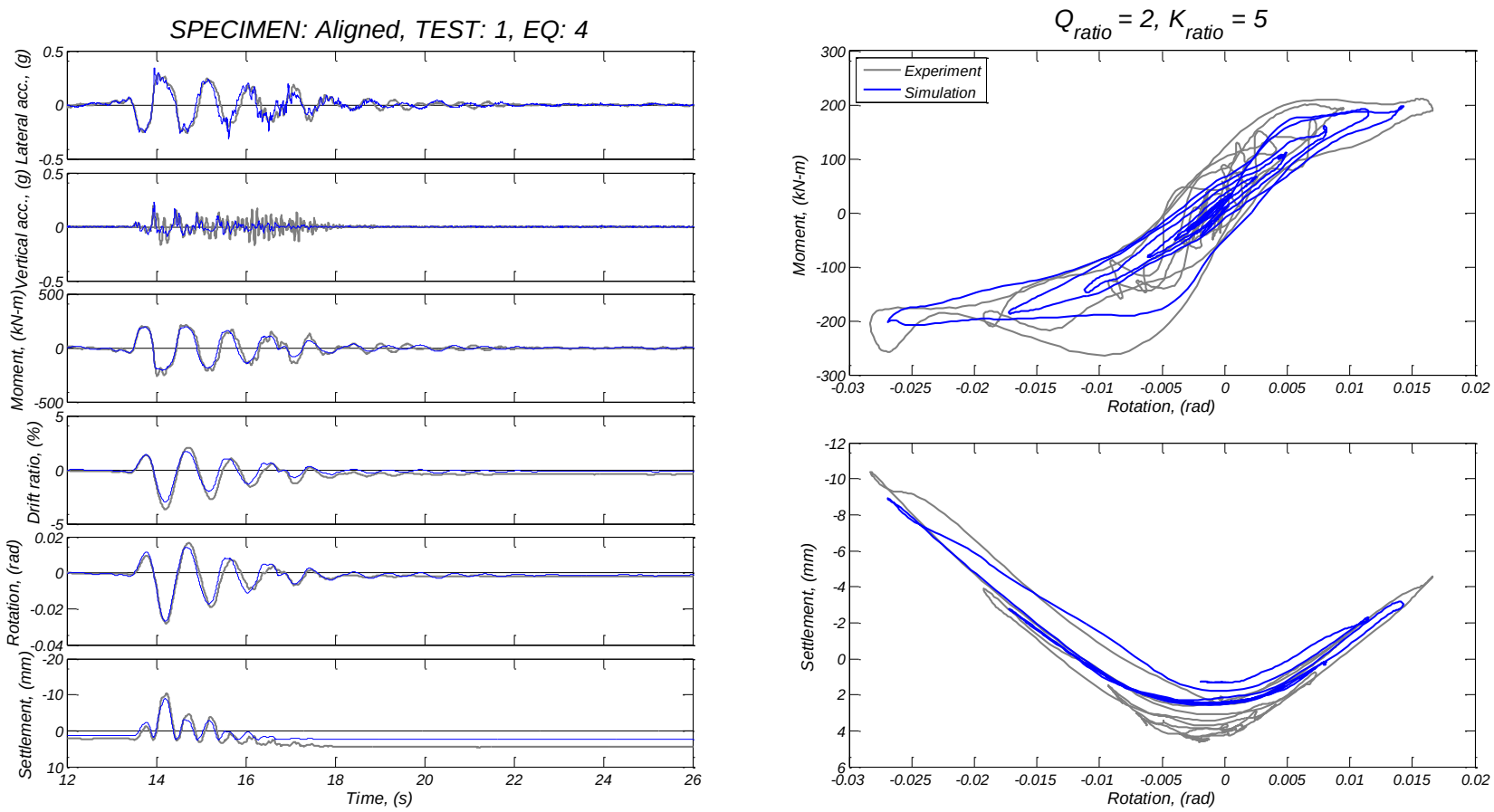

Figure 4.7. Comparison between experimental and numerical simulation results (K_{ratio} = 5) for the aligned specimen, Test Day 1, motion 4.

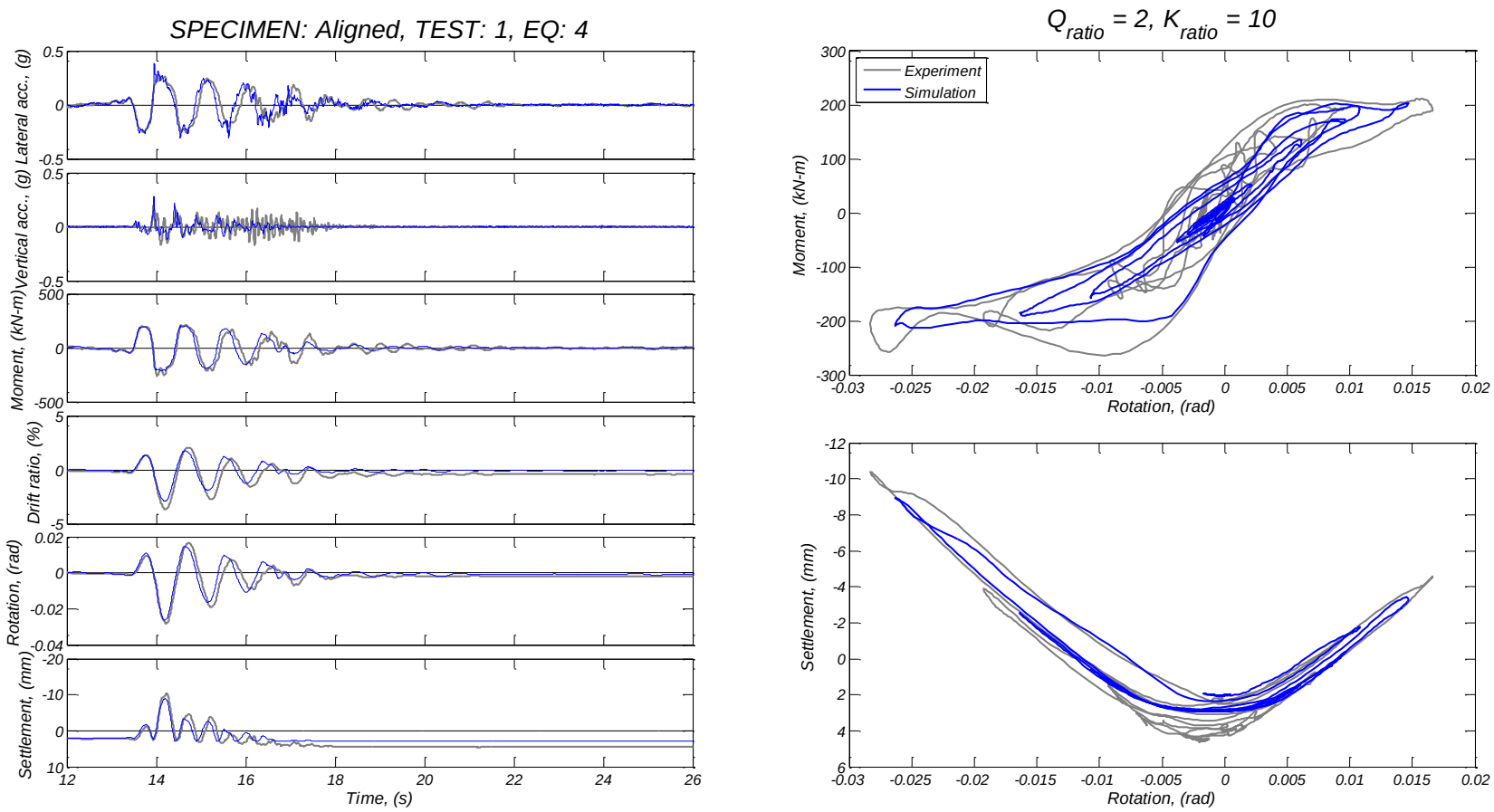

Figure 4.8. Comparison between experimental and numerical simulation results (K_{ratio} = 10) for the aligned specimen, Test Day 1, motion 4.

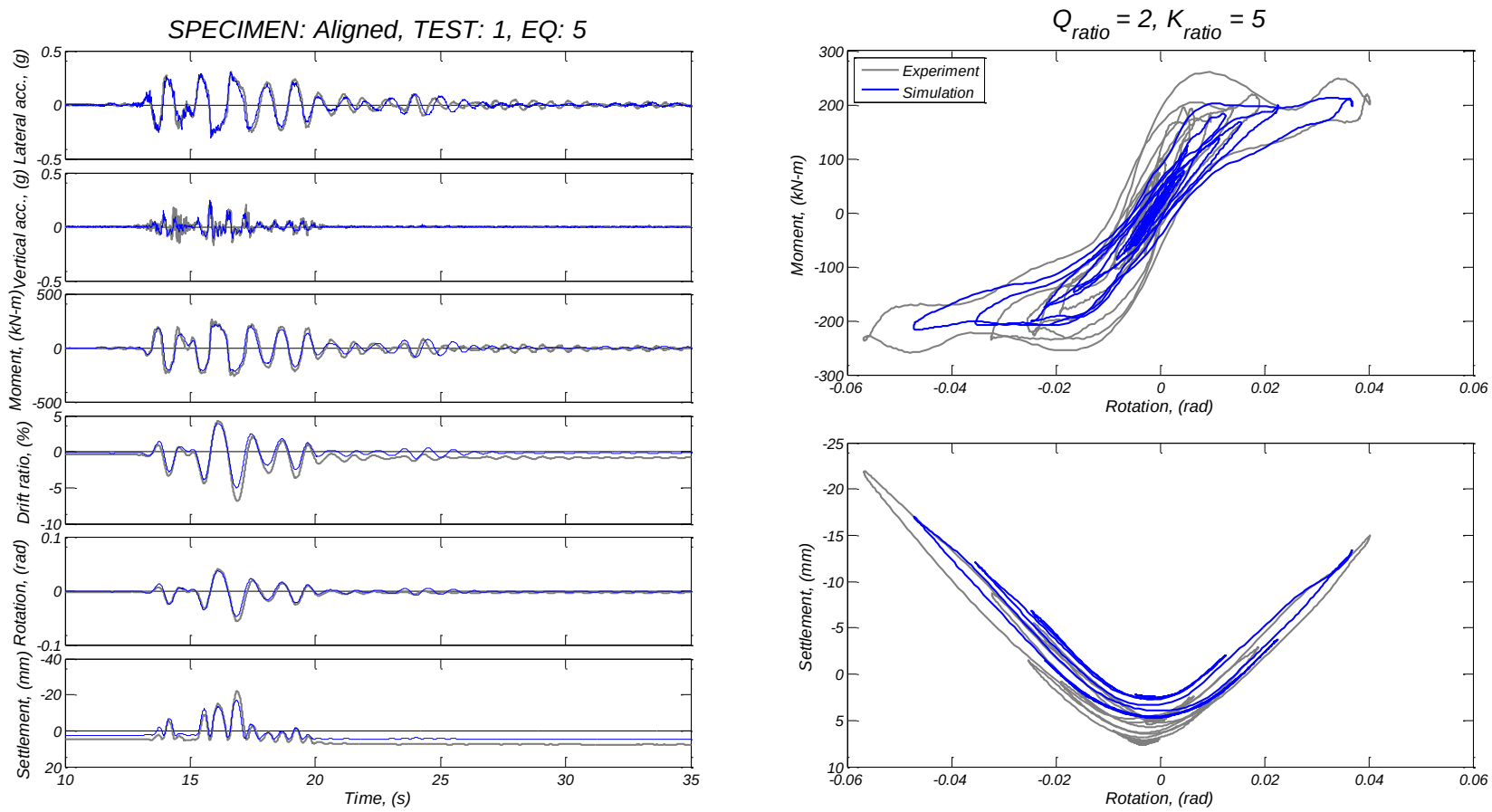

Figure 4.9. Comparison between experimental and numerical simulation results (K_{ratio} = 5) for the aligned specimen, Test Day 1, motion 5.

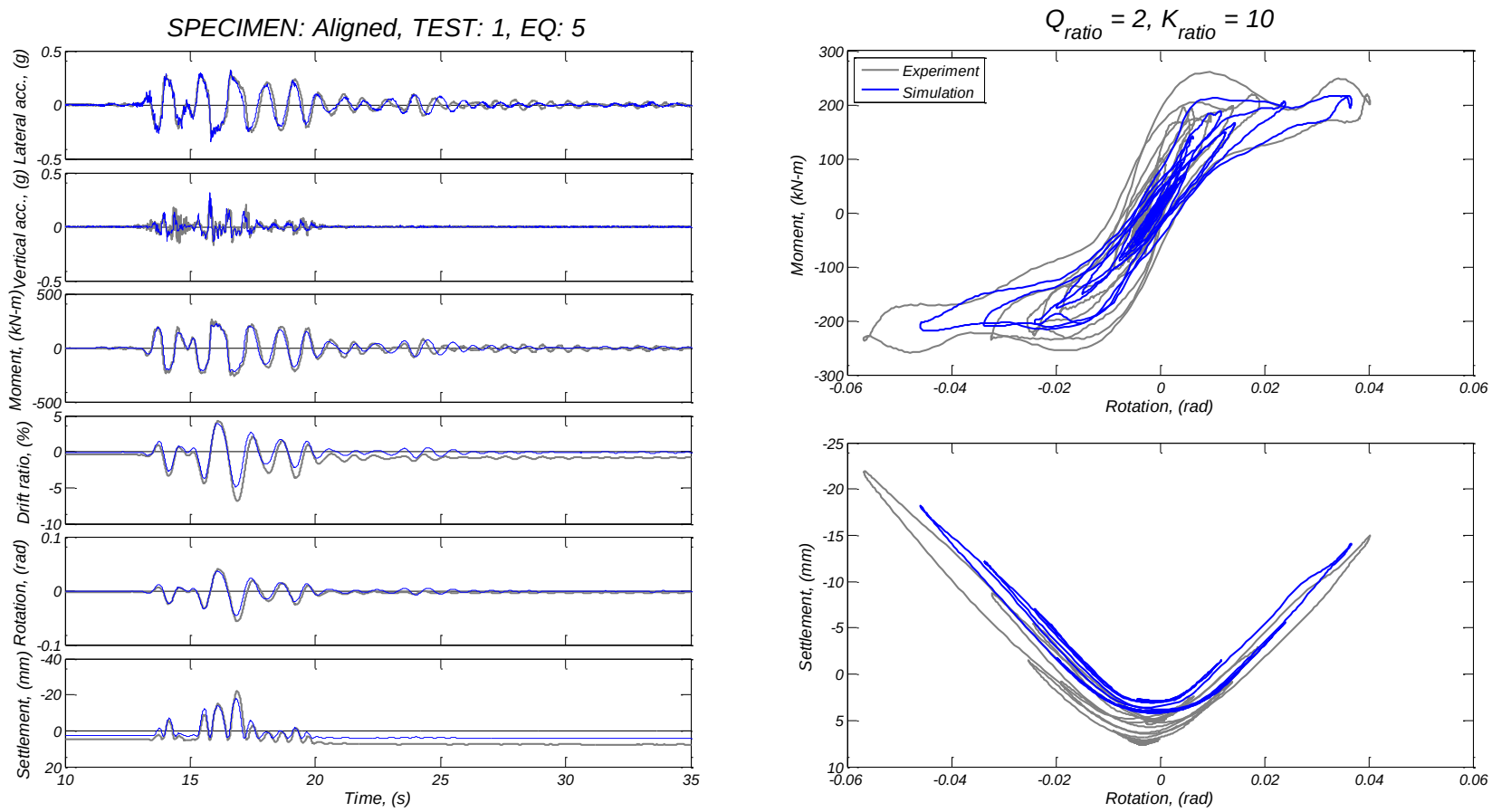

Figure 4.10. Comparison between experimental and numerical simulation results (K_{ratio} = 10) for the aligned specimen, Test Day 1, motion 4.

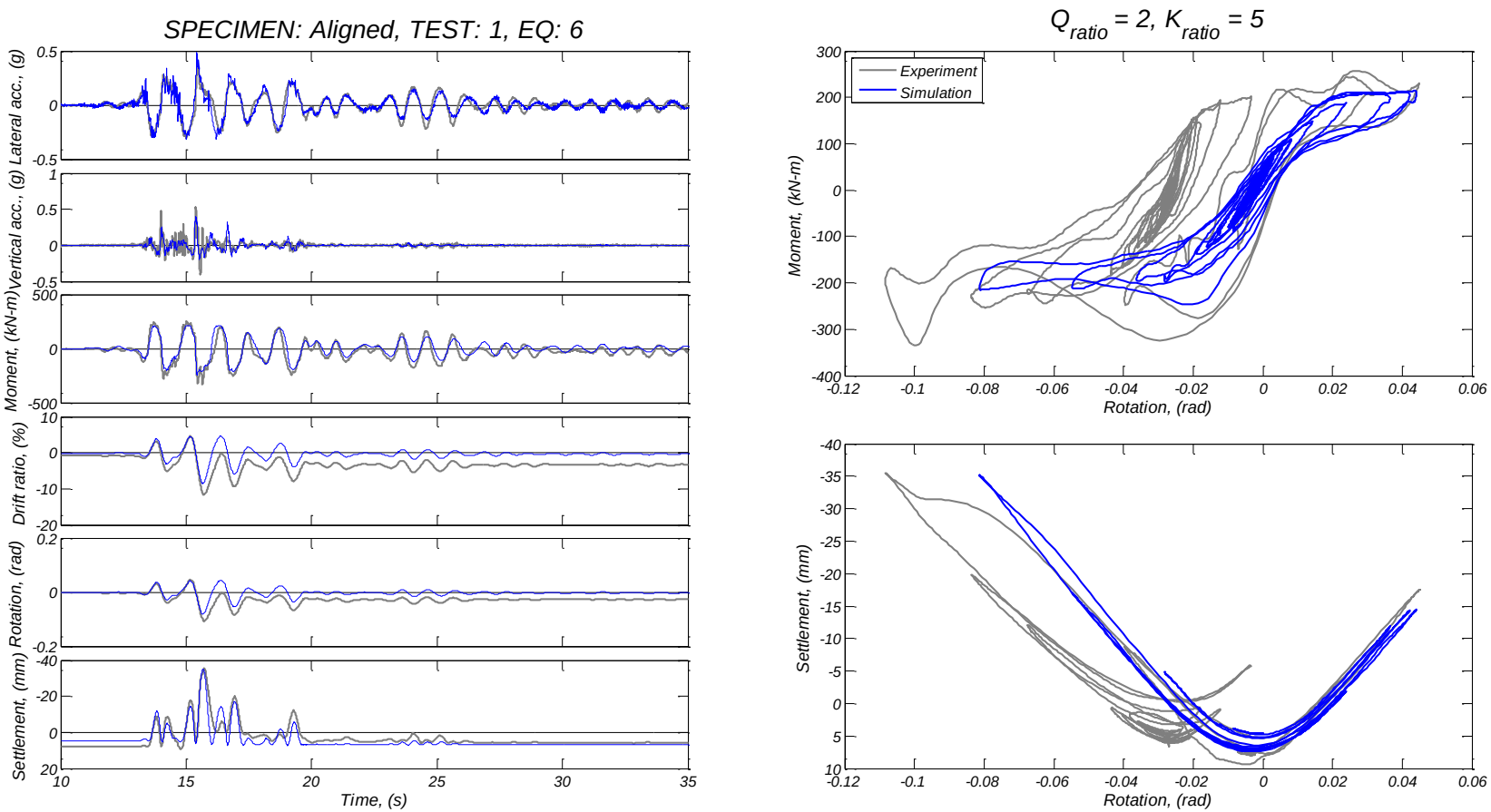

Figure 4.11. Comparison between experimental and numerical simulation results (K_{ratio} = 5) for the aligned specimen, Test Day 1, motion 6.

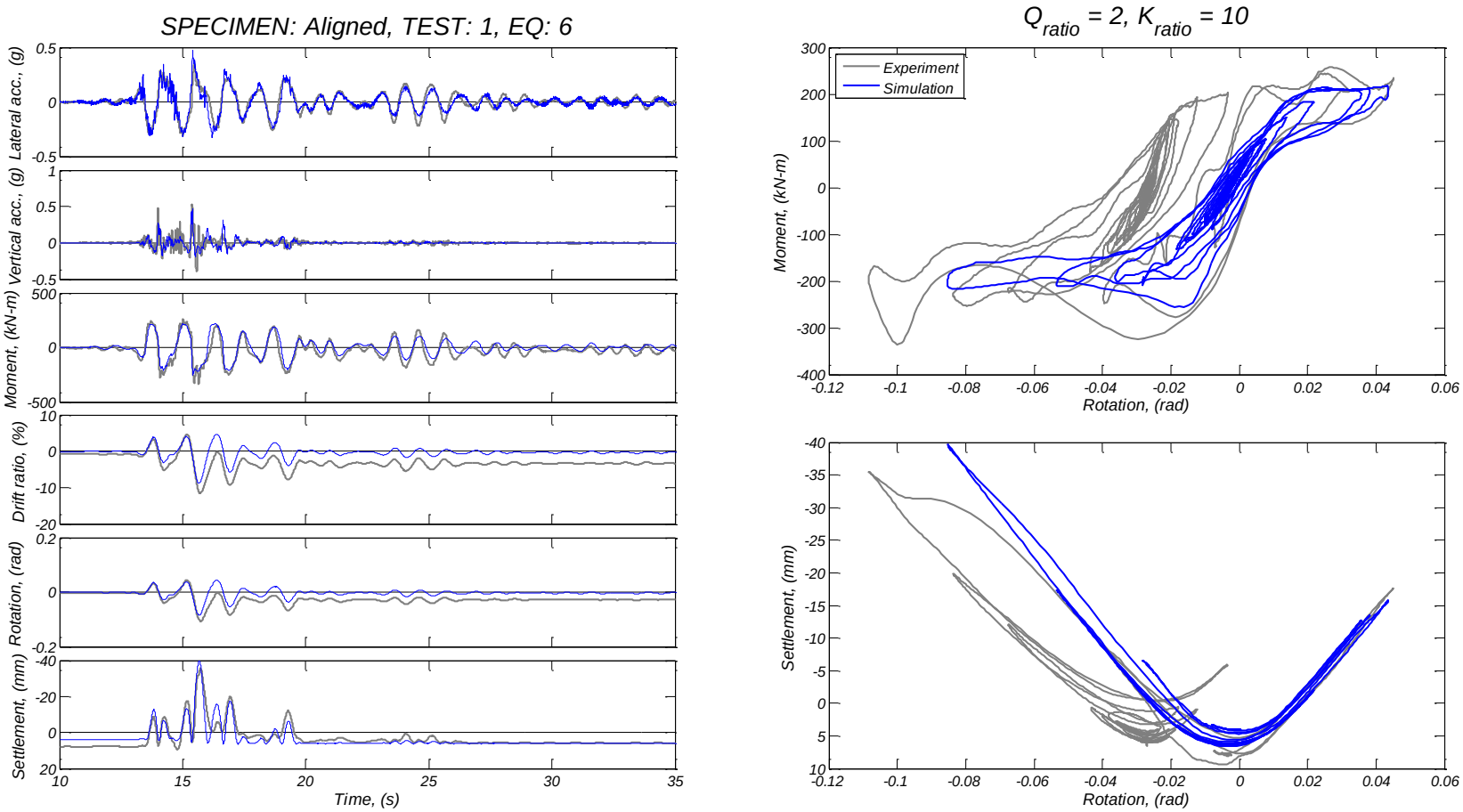

Figure 4.12. Comparison between experimental and numerical simulation results (K_{ratio} = 10) for the aligned specimen, Test Day 1, motion 6.

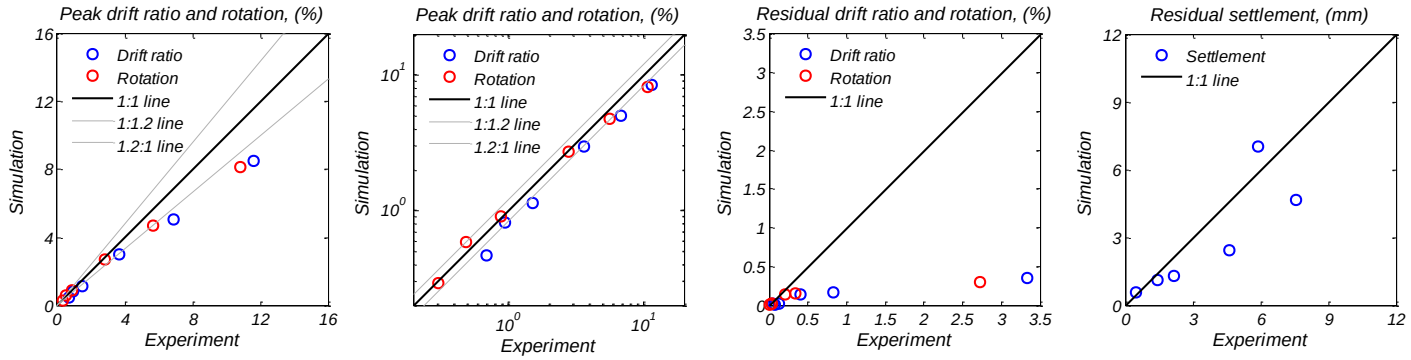

Figure 4.13. Summary of the comparison between the experimental and numerical simulation results (K_{ratio} = 5) for various response parameters.

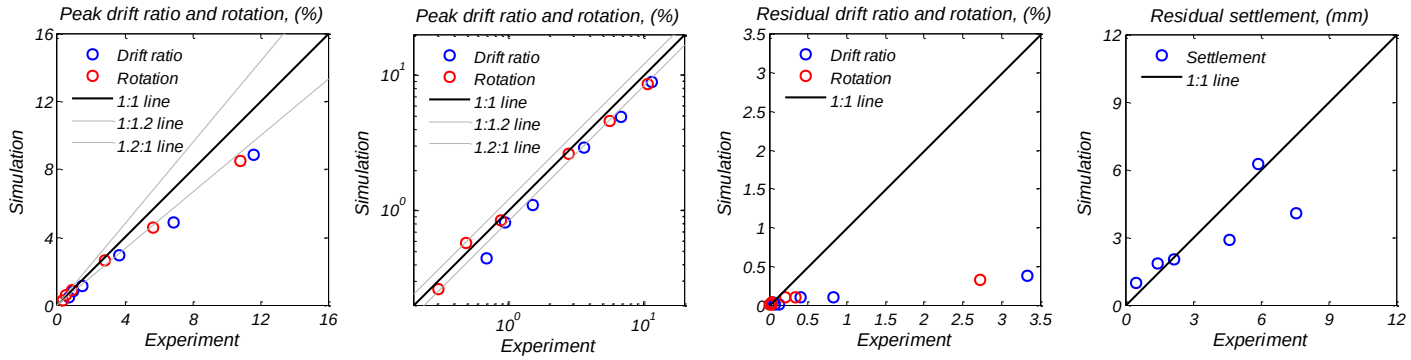

Figure 4.14. Summary of the comparison between the experimental and numerical simulation results (K_{ratio} = 10) for various response parameters.

4.4 Conclusions

This chapter presented a modified Winkler type based model for rocking foundations, based on the model proposed by Harden et al. (2009). The modified model uses uniaxial material with essentially zero tensile stiffness to properly model the foundation moment rotation behavior even under very large rotations. The main changes on the model are summarized below.

(i) The length of the end zone regions are directly calculated based on the A/A_c ratios so that they are identical to the minimum contact lengths.

(ii) The ultimate capacity of the Winkler springs at the end zones is directly calculated based on the actual calculated soil capacity during the minimum contact area between the footing and the soil. This along with (i) ensures the accurate representation of the foundation moment capacity M_r.

(iii) The vertical stiffness of the springs in the end zone regions (and eventually the stiffness of the springs in the middle zone region too) are calibrated so that the secant rocking stiffness when 50% of the foundation moment, M_r, is equal to K_{init} as defined by Dent et al. (2014). The recommended value of $K_{init} = 300M_r$ provided excellent results against the large scale shake table tests.

(iv) The capacity and stiffness of the springs in the middle zones are artificially reduced for the cases of rocking foundations with large A/A_c ratios in order to accurately capture the settlement response. Although more research is required for providing recommendations for the Q_{ratio} and K_{ratio}, using the data from the large scale shake-table test a value of $Q_{ratio} = 2$ and $K_{ratio} = 5$ is proposed here.

Similarly to Harden et al. (2009), a uniform distribution of the damping coefficient along the width of the foundation is adopted here. The damping coefficient can be calculated for the elastic rocking case, using the secant period at the point where $0.5M_r$ is mobilized. The passive and frictional components are also modeled in a similar way with the original model. Finally, the extension to the 3D case can be performed easily.

Using the modeling scheme which was summarized above, the numerical simulations of the large scale shake-table tests (Antonellis et al. 2015) for $Q_{ratio} = 2$ and $K_{ratio} = 5$ and 10 were performed. Both cases showed excellent agreement with the recorded response in terms of acceleration, foundation moment, foundation rotation, and drift ratio response. The agreement with the recorded settlements was also good. The residual drifts were not captured correctly since this is an inherent drawback of Winkler spring models. The flow of sand under the uplifting side of the footing is not modeled by Winkler spring models, but since rocking foundations should be detailed properly to prevent this phenomenon, there is no need for further modifications on the modeling scheme.

Chapter 5: Three-Dimensional Demand Model for Bridge Columns with Rocking Foundations

5.1 Introduction

The overturning of rocking systems has been studied extensively both numerically and experimentally. Makris and Roussos (2000) and Makris and Zhang (2001) studied the overturning response of free standing rigid blocks under idealized pulse excitations and near-fault ground motions. Konstantinidis and Makris (2009) studied experimentally and analytically the overturning of laboratory equipment under earthquake excitation. More recent studies have been performed on the stability of single rigid rocking columns (Makris 2014) and two-column rocking frames (Makris and Vassiliou 2014; Dimitrakopoulos and Paraskeva 2015; Dimitrakopoulos and Giouvanidis 2015). Finally, Deng et al. 2012b studied numerically the 2D seismic demand and the overturning of columns with rocking foundations.

The majority of these studies have been focused on the overturning of simple rigid blocks, either anchored or free standing. In cases where rocking columns and rocking frames have been assumed, the columns have been assumed rigid, with the exception of the study by Deng et al. (2012b). In cases of laboratory equipment the actual seismic response of the rigid block may be irrelevant as long as no overturning occurs. On the other hand, the interaction of the bridge columns with the deck and the abutments will require limited peak drift ratios and rotations, far smaller than the ones that may lead to overturning. The inclusion of the flexibility of the column, the rotatory mass properties of the superstructure weight, the modeling of the hysteretic moment rotation behavior of rocking shallow foundations are critical for the three-dimensional modeling of bridge columns with rocking foundations. This study builds on the previous numerical and experimental evaluation of rocking foundations to investigate numerically a large number of bridge columns with rocking shallow foundations under a plethora of real ground motion recordings.

In this chapter, a total of 44 foundation-column-inertia block units were subjected to two sets of forty ground motions using biaxial horizontal excitation. The numerical model was based on the modified nonlinear Winkler-type springs configuration which was described in the previous chapter. The first set of ground motions included a broadband set of records which result in mean linear spectral demands similar to those expected at a site 10 km from the fault plane of a M7 earthquake event. The second set consisted of only near-fault pulse-like records, including the ones with the highest peak ground velocity and spectral demands at "long" periods ever recorded. The parameters under investigation were the column height, H_c, the ratio of bridge column height to foundation length ($1 \leq H_c/B_f \leq 2.8$), the ratio between the initial rocking stiffness and the foundation moment capacity (K_{init}/M_r) and the weight of the superstructure (W_s). The absolute nonlinear displacement response as well as the ratio of nonlinear displacement to

the linear demand is presented. The conditions that lead to overturn are also discussed. For the pulse-like ground motions, only 12 occasions of overturn were reported. They were only caused by the TCU068 and TCU065 records and for models with C_r values less than 0.17. For the pulse-like motions the nonlinear displacement ratio, r_N, increases rapidly with decrease of the first period, $T_{1,s}$, for $T_{1,s} < 0.75$ s. For the near-fault motions, the demand as well as the number of overturns was related well with pulse energy and pulse area. No overturn was computed for the broadband set of ground motions.

5.2 Ground Motions

5.2.1 Broadband set of ground motions

The ground motions of broadband set consisted of 40 unscaled records (Table 5.1) selected so that their mean response spectrum matched the median spectrum, in the period range of 0–5 sec computed from Boore and Atkinson (2008), of a magnitude 7 (M7) strike-slip earthquake for a site at a distance of 10 km from the fault for a site with V_{s30} equal to 250 m/sec (Baker et al. 2011). Figure 5.1 shows the linear acceleration and displacement response spectra for each of the 40 ground motions, as well as the mean spectra. For the numerical analyses, the fault normal component was applied in the transverse direction and the fault parallel component in the longitudinal direction of the bridge piers.

Table 5.1. Broadband set of ground motions.

No.	Earthquake location	Year	M_w	R_{rup} (km)	Station Name
1	Mammoth Lakes	1980	6.0	15.5	Long Valley Dam (Upr L Abut)
2	Chi-Chi, Taiwan	1999	7.6	16.1	CHY036
3	Cape Mendocino, CA	1992	7.0	14.3	Rio Dell Overpass – FF
4	Imperial Valley, CA	1979	6.5	22.0	Delta
5	Kocaeli, Turkey	1999	7.5	4.8	Yarimca
6	Imperial Valley, CA	1979	6.5	24.6	Calipatria Fire Station
7	Chi-Chi, Taiwan	1999	7.6	14.8	CHY034
8	Chi-Chi, Taiwan	1999	7.6	38.4	NST
9	Kocaeli, Turkey	1999	7.5	15.4	Duzce
10	Trinidad	1980	7.2	-	Rio Dell Overpass, E Ground
11	Spitak, Armenia	1988	6.8	-	Gukasian
12	Loma Prieta, CA	1989	6.9	14.3	Gilroy Array #4
13	Chi-Chi, Taiwan	1999	7.6	8.5	TCU060
14	Victoria, Mexico	1980	6.3	19.0	Chihuahua
15	Loma Prieta, CA	1989	6.9	39.9	Fremont - Emerson Court
16	Chalfant Valley	1986	6.2	7.6	Zack Brothers Ranch
17	Chi-Chi, Taiwan	1999	7.6	26.8	TCU118
18	Denali, Alaska	2002	7.9	2.7	TAPS Pump Station #10
19	Imperial Valley, CA	1979	6.5	7.1	El Centro Array #4
20	Big Bear	1992	6.5	-	San Bernardino - E & Hospitality
21	Landers, CA	1992	7.3	23.6	Yermo Fire Station
22	Northridge, CA	1994	6.7	5.4	Sylmar - Converter Sta
23	San Fernando, CA	1971	6.6	22.8	LA - Hollywood Stor FF
24	N. Palm Springs, CA	1986	6.0	12.1	Morongo Valley
25	Loma Prieta, CA	1989	6.9	27.9	Hollister - South & Pine
26	Chi-Chi, Taiwan	1999	7.6	6.4	TCU055
27	Chi-Chi, Taiwan	1999	7.6	19.1	CHY025
28	Imperial Valley, CA	1979	6.5	10.4	Brawley Airport
29	Chi-Chi, Taiwan	1999	7.6	37.5	CHY088
30	Duzce, Turkey	1999	7.1	6.6	Duzce
31	Chi-Chi, Taiwan	1999	7.6	17.2	TCU061
32	Loma Prieta, CA	1989	6.9	8.5	Saratoga - Aloha Ave
33	Imperial Valley, CA	1940	7.0	6.1	El Centro Array #9
34	Chi-Chi, Taiwan	1999	7.6	31.8	TCU123
35	Northridge, CA	1994	6.7	5.4	Jensen Filter Plant
36	Chi-Chi, Taiwan	1999	7.6	35.1	CHY104
37	Loma Prieta, CA	1989	6.9	32.8	Salinas - John & Work
38	Loma Prieta, CA	1989	6.9	20.8	Coyote Lake Dam (Downst)
39	Chi-Chi, Taiwan	1999	7.6	40.4	CHY008
40	Chi-Chi, Taiwan	1999	7.6	45.7	TCU141

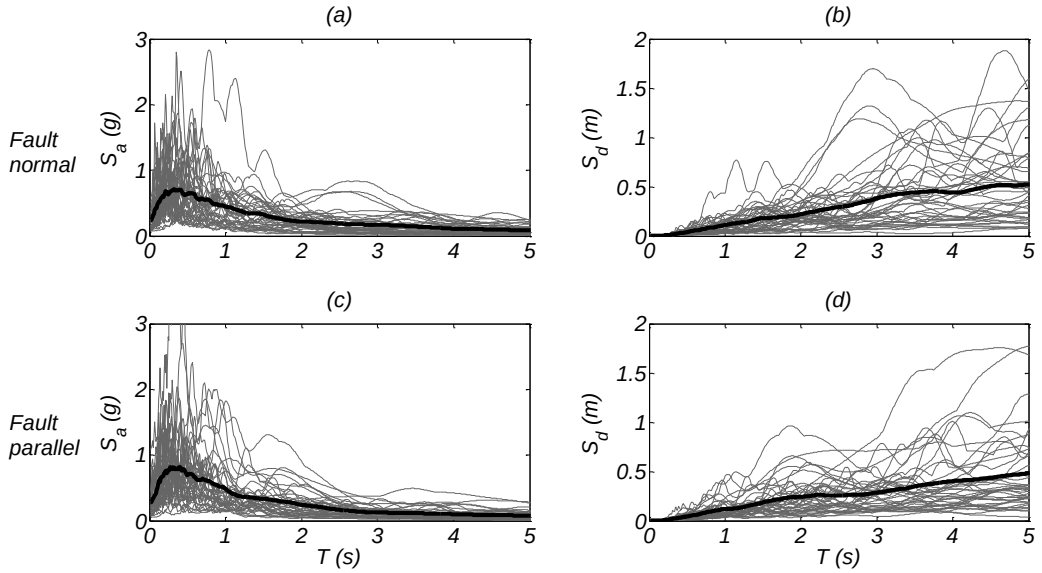

Figure 5.1. (a,b) Linear acceleration and displacement response spectra for the fault normal and (c,d) fault parallel direction of the broadband set of ground motions (damping ratio ζ=2%).

5.2.2 Pulse-like set of ground motions

Table 5.2 lists the 40 historical near-fault pulse-like ground motion records studied in Lu and Panagiotou (2012). The motions are rotated to the fault normal (FN) and fault parallel (FP) direction. The 40 ground motion records come from 17 historical earthquakes with magnitude M_W varying from 6.3 to 7.9; the recorded peak ground velocity (PGV) of the FN horizontal component of the 40 records ranges between 49 and 185 cm/s, with an average value of 106 cm/s. The specific earthquakes and their associated records are numbered in ascending order of earthquake magnitude. For each motion, the first two predominant pulses are identified by wavelet analysis (the CPEV_EN method from Lu and Panagiotou 2012) and the pulse period, acceleration amplitude, velocity amplitude, energy and area are also listed in Table 5.2. Additional parameters for these ground motions such as the strike angle, the distance from fault rupture plane (R_{rup}), the peak ground acceleration (PGA), the peak ground velocity (PGV), the peak ground displacement (PGD), and the shear wave velocity of the top 30 m of soil (V_{s30}) are also reported in Lu and Panagiotou (2012).

These records were selected by the following criteria: (a) earthquake magnitude $M_W \geq 6.3$; (b) distance from the fault rupture plane less than 10 km; and (c) PGV $\geq$ 60 cm/s in any of the two recorded horizontal components; the 1979 Imperial Valley, California, 1994 Northridge, California, and 1999 Chi-chi, Taiwan earthquake records were limited to the 5, 8, and 9 records, respectively, with the largest PGV. The 2011 Christchurch, New Zealand earthquake resulted in four more ground motion records (in addition to the PRPC record studied here) with $R_{rup} \leq 10$ km and PGV $\geq$ 60 cm/s that were not included here. It should be noted that the selected 40 records correspond to about 40% of the total number of historical records to date with $M_W \geq 6.3$ and $R_{rup} \leq 10$ km.

The linear acceleration and displacement spectra of the near-fault pulse-like ground motions for the FN and FP components are shown in Figure 5.2. Figure 5.3 plots the periods of the two pulses from the FN component with the highest energy for each of the 40 ground motions as determined by Lu and Panagiotou (2012). It can be seen that pulses with periods larger than 4 seconds can be caused even by earthquakes with smaller magnitudes.

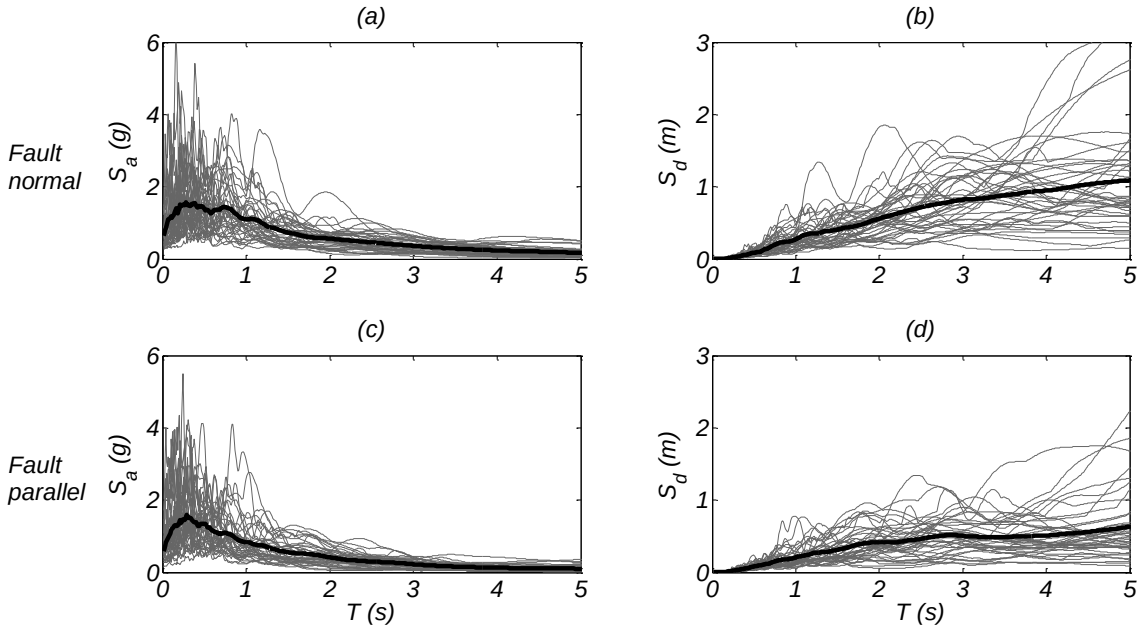

Figure 5.2. (a,b) Linear acceleration and displacement response spectra for the fault normal and (c,d) fault parallel direction of the near-fault pulse-like set of ground motions (damping ratio ζ=2%).

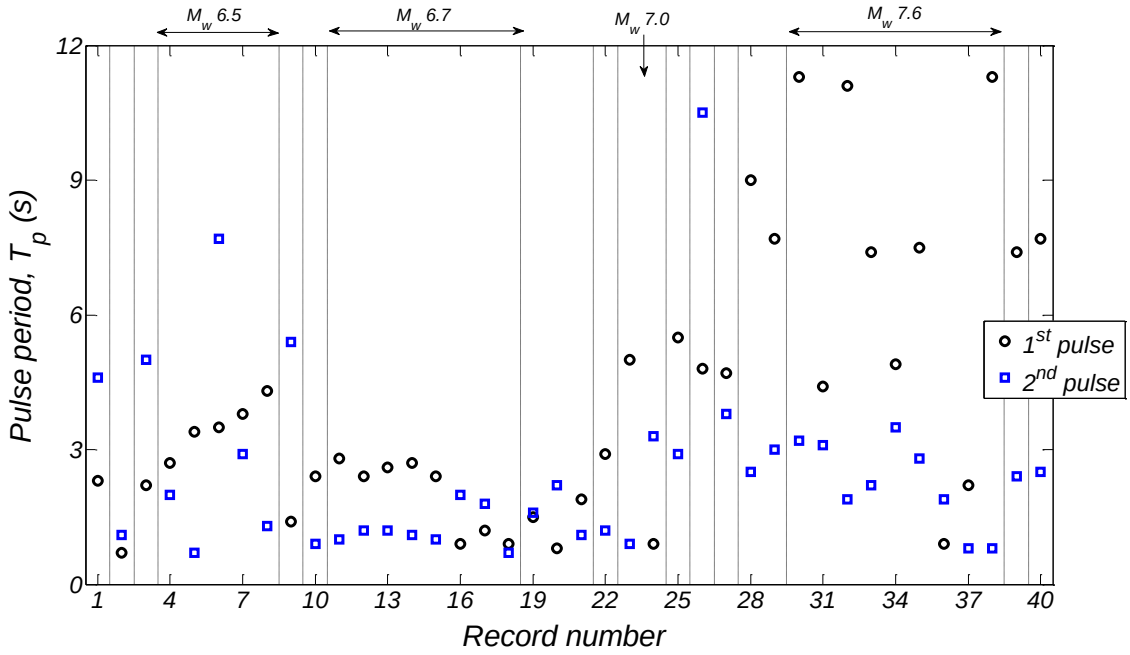

Figure 5.3. Predominant pulse periods of the fault normal (FN) component of the 40 near-fault pulse-like ground motions.

Table 5.2. Near-fault pulse-like set of ground motions.

No.	Earthquake location	Year	M_w	Station Name	R_{rup} (km)	1st pulse (FN)					2nd pulse (FN)				
						$T_{p,1}$ (s)	a_{max} (g)	v_{max} (cm/s)	Energy (m^2/s)	Area (m)	$T_{p,2}$ (s)	a_{max} (g)	v_{max} (cm/s)	Energy (m^2/s)	Area (m)
1	Christchurch, NZ	2011	6.3	PRPC	2.5	2.3	0.26	90.4	0.74	1.29	4.6	0.04	28.5	0.20	1.16
2	Coalinga, CA	1983	6.4	Pleasant Valley P.P. - Yard	8.4	0.7	0.49	58.0	0.09	0.25	1.1	0.18	35.4	0.07	0.34
3	Superstition Hills, CA	1987	6.5	Parachute Test Site	1.0	2.2	0.30	96.7	0.89	1.37	5.0	0.03	26.3	0.17	1.03
4	Imperial Valley-06, CA	1979	6.5	EC Meloland Overpass FF	0.1	2.7	0.19	87.4	0.77	1.46	2.0	0.08	27.8	0.08	0.48
5	Imperial Valley-06, CA	1979	6.5	El Centro Array #7	0.6	3.4	0.13	73.4	0.84	1.87	0.7	0.29	33.0	0.06	0.28
6	Imperial Valley-06, CA	1979	6.5	El Centro Array #6	1.4	3.5	0.16	84.3	1.38	2.45	7.7	0.01	7.0	0.03	0.66
7	Imperial Valley-06, CA	1979	6.5	El Centro Array #5	4.0	3.8	0.14	81.0	0.99	1.93	2.9	0.05	20.6	0.06	0.47
8	Imperial Valley-06, CA	1979	6.5	El Centro Array #4	7.1	4.3	0.10	69.0	0.82	1.86	1.3	0.13	24.6	0.04	0.27
9	San Fernando, CA	1971	6.6	Pacoima Dam	1.8	1.4	0.41	98.2	0.50	0.85	5.4	0.03	27.4	0.17	1.07
10	Erzincan, Turkey	1992	6.7	Erzincan	4.4	2.4	0.20	79.0	0.57	1.18	0.9	0.24	36.5	0.08	0.35
11	Northridge, CA	1994	6.7	Sylmar - Converter Sta East	5.2	2.8	0.10	47.2	0.47	1.62	1.0	0.31	47.6	0.09	0.30
12	Northridge, CA	1994	6.7	Sylmar Olive View Med FF	5.3	2.4	0.15	63.5	0.66	1.77	1.2	0.21	44.1	0.16	0.62
13	Northridge, CA	1994	6.7	Sylmar - Converter Sta	5.4	2.6	0.16	70.0	0.92	2.18	1.2	0.29	60.9	0.30	0.85
14	Northridge, CA	1994	6.7	Jensen Filter Plant	5.4	2.7	0.15	74.1	0.88	2.02	1.1	0.21	43.0	0.10	0.41
15	Northridge, CA	1994	6.7	Newhall W. Pico Canyon Rd	5.5	2.4	0.24	77.4	0.69	1.26	1.0	0.17	29.8	0.06	0.35
16	Northridge, CA	1994	6.7	Newhall Fire Station	5.9	0.9	0.65	95.2	0.31	0.53	2.0	0.17	48.9	0.20	0.62
17	Northridge, CA	1994	6.7	Rinaldi Receiving Station	6.5	1.2	0.70	129.2	0.80	0.97	1.8	0.17	48.2	0.17	0.54
18	Northridge, CA	1994	6.7	Pacoima Dam	7.0	0.9	0.66	66.8	0.29	0.50	0.7	0.36	43.5	0.08	0.31
19	Kobe, Japan	1995	6.9	Takarazuka	0.3	1.5	0.24	59.5	0.20	0.55	1.6	0.09	23.4	0.06	0.45
20	Kobe, Japan	1995	6.9	KJMA	1.0	0.8	0.69	94.9	0.44	0.78	2.2	0.14	42.3	0.19	0.63
21	Kobe, Japan	1995	6.9	Takatori	1.5	1.9	0.36	114.5	1.60	2.29	1.1	0.44	82.4	0.52	1.07
22	Loma Prieta, CA	1989	6.9	LGPC	3.9	2.9	0.10	53.2	0.56	1.79	1.2	0.32	64.9	0.19	0.48
23	Cape Mendocino, CA	1992	7.0	Cape Mendocino	7.0	5.0	0.05	35.0	0.24	1.10	0.9	0.29	44.7	0.07	0.25
24	Cape Mendocino, CA	1992	7.0	Petrolia	8.2	0.9	0.49	67.3	0.16	0.38	3.3	0.05	25.1	0.08	0.52
25	Duzce, Turkey	1999	7.1	Duzce	6.6	5.5	0.04	42.0	0.66	2.70	2.9	0.05	25.7	0.13	0.88
26	Landers, CA	1992	7.3	Lucerne	2.2	4.8	0.11	75.9	1.19	2.34	10.5	0.01	18.7	0.22	2.00
27	Tabas, Iran	1978	7.4	Tabas	2.1	4.7	0.12	100.6	2.41	4.10	3.8	0.05	31.3	0.27	1.42
28	Kocaeli, Turkey	1999	7.5	Sakarya	3.1	9.0	0.03	41.5	0.59	2.32	2.5	0.08	30.1	0.10	0.48
29	Kocaeli, Turkey	1999	7.5	Yarimca	4.8	7.7	0.03	32.0	0.38	1.67	3.0	0.06	30.8	0.19	1.08

Table 5.2 (cont'd)

No.	Earthquake location	Year	M_w	Station Name	R_{rup} (km)	1st Pulse (FN)					2nd Pulse (FN)				
						$T_{p,1}$ (s)	a_{max} (g)	v_{max} (cm/s)	Energy (m^2/s)	Area (m)	$T_{p,2}$ (s)	a_{max} (g)	v_{max} (cm/s)	Energy (m^2/s)	Area (m)
30	Chi-Chi, Taiwan	1999	7.6	TCU068	0.3	11.3	0.09	158.8	10.84	11.13	3.2	0.22	101.2	1.41	2.08
31	Chi-Chi, Taiwan	1999	7.6	TCU065	0.6	4.4	0.12	90.0	2.50	4.67	3.1	0.09	46.3	0.41	1.48
32	Chi-Chi, Taiwan	1999	7.6	TCU067	0.6	11.1	0.02	42.4	0.76	2.92	1.9	0.23	62.7	0.32	0.77
33	Chi-Chi, Taiwan	1999	7.6	TCU052	0.7	7.4	0.11	133.4	5.01	6.12	2.2	0.21	72.5	0.79	1.74
34	Chi-Chi, Taiwan	1999	7.6	TCU075	0.9	4.9	0.10	78.3	1.20	2.40	3.5	0.04	24.0	0.14	0.98
35	Chi-Chi, Taiwan	1999	7.6	TCU102	1.5	7.5	0.04	55.7	1.07	3.13	2.8	0.10	45.7	0.36	1.22
36	Chi-Chi, Taiwan	1999	7.6	CHY080	2.7	0.9	0.59	91.7	0.53	0.97	1.9	0.12	42.0	0.17	0.70
37	Chi-Chi, Taiwan	1999	7.6	CHY028	3.1	2.2	0.10	39.3	0.18	0.77	0.8	0.30	44.2	0.09	0.36
38	Chi-Chi, Taiwan	1999	7.6	TCU072	7.0	11.3	0.01	18.5	0.16	1.31	0.8	0.35	47.5	0.13	0.45
39	Denali, Alaska	2002	7.9	Alyeska Pump Station 10	2.7	7.4	0.04	47.0	0.71	2.24	2.4	0.14	53.1	0.51	1.56
40	Wenchuan, China	2008	7.9	Mianzuqingping	3.0	7.7	0.07	78.8	1.91	3.80	2.5	0.09	39.9	0.27	1.16

5.3 Benchmark Bridge Piers

The bridge piers studied here consisted of a square foundation and a single circular column supporting the superstructure weight. The main characteristics of each model are shown in

Table 5.3. The parameters altered here were: (i) the clear height of the column (H_c), (iii) the width of the foundation (B_f), the ratio of the initial rocking stiffness, K_{init}, to the moment capacity of the foundation, M_r, (K_{init}/M_r), and (iv) the weight of the superstructure (W_s). More specifically, four column heights were investigated; 6.1, 9.1, 12.2, 15.2 m, and two superstructure weights; 6.7 and 13.3 MN. For each column height and superstructure weight, two to three foundation widths were chosen resulting to column height to foundation width ratios, H_c/B_f, between 1 and 2.8. The foundation widths were selected such that the resulting base shear coefficient, C_r, spanned sufficiently the design range of interest as described below. The base shear coefficient, C_r, is defined as the foundation base shear that mobilizes the moment capacity of the foundation, M_r, divided by the seismic weight of the bridge pier, W_{seism}. In this study the seismic weight was assumed to be equal to the sum of the superstructure weight and one third of the column weight. Finally, for each resulting model two different values of the initial rocking stiffness to the foundation moment capacity ratios were assumed; 230 and 460. The initial rocking stiffness of the rocking foundation is defined in terms of a trilinear moment rotation representation of rocking foundations by Deng and Kutter 2014. It is essentially the actual secant stiffness of the foundation at the point where 50% of the foundation moment, M_r, capacity has been mobilized, as described in the previous chapter.

For simplicity, a number of parameters were kept constant for all of the above models. The height of the footing was assumed to be equal to 1.8 m, and the embedment height of all footings was equal to 2.4 m. Note that although the weight of overlying soil was included in the modeling, the passive resistance of the backfill soil was ignored, as described later. The distance between the top of the column and the center of gravity of the superstructure was equal to 1.2 m. The superstructure weight was assumed to have a square plan view with a side of 12.2 m and a height of 1.8 m. The specific weight of the soil and the concrete were equal to 16 and 24 kN/m^3 respectively.

Additionally, since rocking foundations are expected to be used in competent soil conditions, a constant contact area ratio during rocking, A/A_c, equal to 8 was assumed. In the previous expression A_c is the area of the minimum contact between the footing and the soil during rocking and A is the total area of the footing. Experimental studies have shown that for A/A_c ratios larger than about 8, the resulting cumulative settlements are limited (Deng et al. 2012a).

The selection of the model parameters is based on the following iterative procedure. Assuming a foundation width B_f, the minimum contact area A_c, the total weight of the bridge pier, the moment capacity of the foundation, M_r, and the required ultimate stress capacity of the soil at the contact area during rocking, $Q_{s,r}$, can be calculated. The base shear coefficient, C_r, is then calculated as M_r / ($W_{seism}H$), where H is the distance of the centroid of the deck to the base of the footing and W_{seism} the seismic weight of the bridge pier, as defined above. The diameter of the circular column, D_c, is chosen such that the

resulting moment capacity of the column, assuming a longitudinal reinforcing steel ratio of 2.5%, is larger than the foundation moment capacity for any direction of loading.
The above calculations were performed for each model for different values of foundation widths and the final values were chosen so that the resulting base shear coefficients are inside the range of values most commonly used in practice, i.e. 0.15 to 0.4. An additional constraint was that the required ultimate capacity of the soil during rocking could not exceed a peak value, equal here to 6.5 MPa. Using the numerical model of each bridge pier which is described below, the secant rocking period at the point where 50% of the foundation moment capacity was mobilized, $T_{1,s}$, was also calculated (see

Table 5.3). Table 2.1. Set of the fourteen ground motions and their individual scale factors for the DE and MCE level.

Figure 5.4 plots the correlation between the main parameters of the model. It can be seen that increased base shear coefficient, C_r, results to smaller period, $T_{1,s}$, since it inherently implies larger foundation width, B_f, and column diameter, D_c. In a similar manner by increasing the H_c/B_f ratio, the secant period increases and the base shear coefficient decreases. For example, for a column height to foundation width ratio equal to 2.8, the maximum base shear coefficient of the given suites of models is equal to 0.18. Larger base shear coefficients would require larger A/A_c ratios, compared to the value of 8 which was assumed here, which would then also imply larger vertical soil stress capacities compared to the ones assumed here (6.5MPa).

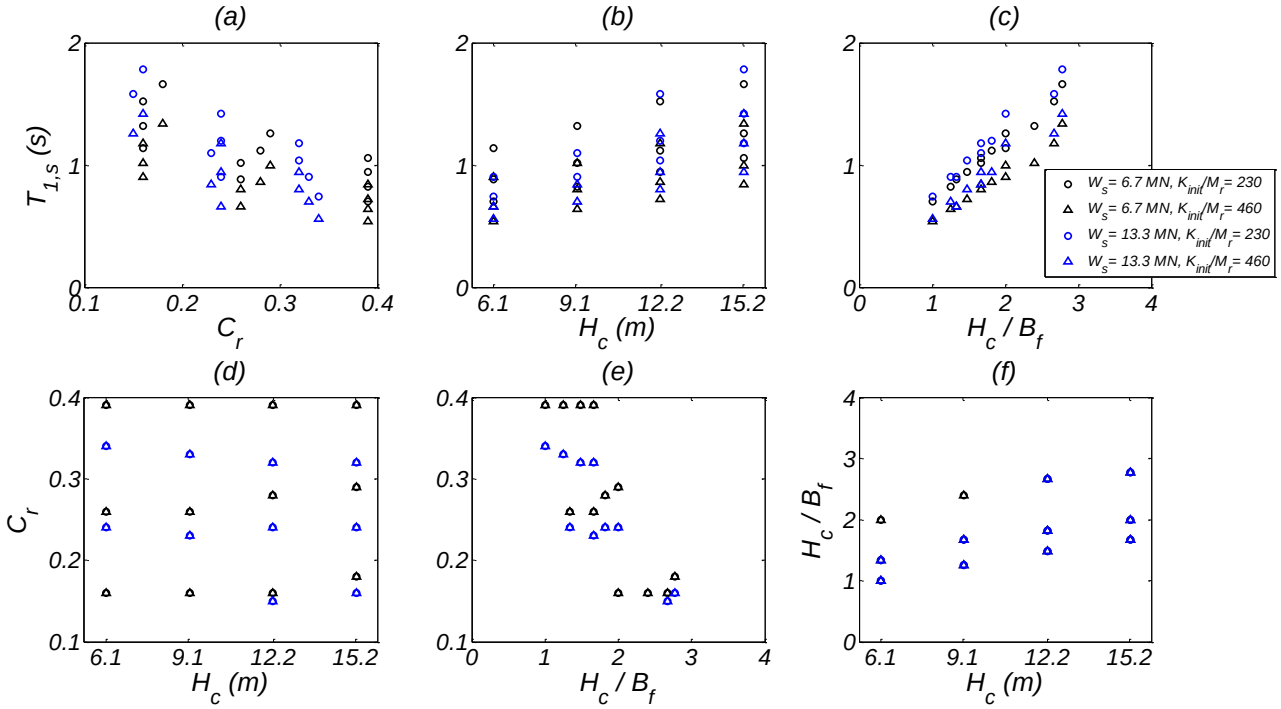

Figure 5.4. Relation between the main four parameters of the 44 models; secant period ($T_{1,s}$), base shear coefficient (C_r), column height (H_c), and column height to foundation width ratio (H_c/B_f).

Table 5.3. Bridge foundation-column-mass model parameters.

No.	H_c (m)	H_c / B_f	B_f (m)	D_c (m)	K_{init}/M_r	W_s (MN)	M_r (MN-m)	$Q_{s,r}$ (MPa)	C_r	c (kN-s/m^3)	$T_{1,s}$ (s)
1	6.1	1.0	6.1	2.1	230	6.7	24.4	1.97	0.39	684.9	0.71
2	6.1	1.3	4.6	1.8	230	6.7	16.3	3.12	0.26	887.5	0.87
3	6.1	2.0	3.0	1.5	230	6.7	9.9	6.39	0.16	1647.8	1.14
4	6.1	1.0	6.1	2.1	460	6.7	24.4	1.97	0.39	763.4	0.54
5	6.1	1.3	4.6	1.8	460	6.7	16.3	3.12	0.26	962.9	0.67
6	6.1	2.0	3.0	1.5	460	6.7	9.9	6.39	0.16	1737.4	0.89
7	9.1	1.3	7.3	2.4	230	6.7	33.6	1.57	0.39	559.2	0.82
8	9.1	1.7	5.5	2.1	230	6.7	21.7	2.40	0.26	678.6	1.02
9	9.1	2.4	3.8	1.8	230	6.7	13.3	4.41	0.16	1063.5	1.33
10	9.1	1.3	7.3	2.4	460	6.7	33.6	1.57	0.39	618.9	0.64
11	9.1	1.7	5.5	2.1	460	6.7	21.7	2.40	0.26	736.7	0.80
12	9.1	2.4	3.8	1.8	460	6.7	13.3	4.41	0.16	1129.5	1.03
13	12.2	1.5	8.2	2.7	230	6.7	43.0	1.41	0.39	491.7	0.94
14	12.2	1.8	6.7	2.4	230	6.7	30.5	1.85	0.28	541.9	1.12
15	12.2	2.7	4.6	2.0	230	6.7	17.3	3.31	0.16	777.6	1.51
16	12.2	1.5	8.2	2.7	460	6.7	43.0	1.41	0.39	546.7	0.73
17	12.2	1.8	6.7	2.4	460	6.7	30.5	1.85	0.28	590.6	0.87
18	12.2	2.7	4.6	2.0	460	6.7	17.3	3.31	0.16	823.1	1.19
19	15.2	1.7	9.1	2.9	230	6.7	53.8	1.29	0.39	441.4	1.06
20	15.2	2.0	7.6	2.6	230	6.7	38.7	1.60	0.29	471.3	1.26
21	15.2	2.8	5.5	2.1	230	6.7	22.9	2.54	0.18	598.5	1.66
22	15.2	1.7	9.1	2.9	460	6.7	53.8	1.29	0.39	487.0	0.84
23	15.2	2.0	7.6	2.6	460	6.7	38.7	1.60	0.29	509.0	0.99
24	15.2	2.8	5.5	2.1	460	6.7	22.9	2.54	0.18	631.5	1.35
25	6.1	1.0	6.1	2.6	230	13.3	42.8	3.46	0.34	721.0	0.74
26	6.1	1.3	4.6	2.3	230	13.3	30.1	5.75	0.24	970.8	0.89
27	6.1	1.0	6.1	2.6	460	13.3	42.8	3.46	0.34	799.6	0.55
28	6.1	1.3	4.6	2.3	460	13.3	30.1	5.75	0.24	1055.6	0.67
29	9.1	1.3	7.3	2.7	230	13.3	55.8	2.61	0.33	568.7	0.90
30	9.1	1.7	5.5	2.4	230	13.3	38.3	4.24	0.23	721.0	1.10
31	9.1	1.3	7.3	2.7	460	13.3	55.8	2.61	0.33	623.6	0.69
32	9.1	1.7	5.5	2.4	460	13.3	38.3	4.24	0.23	777.6	0.84
33	12.2	1.5	8.2	3.0	230	13.3	68.4	2.25	0.32	493.3	1.03
34	12.2	1.8	6.7	2.7	230	13.3	51.1	3.10	0.24	559.2	1.21
35	12.2	2.7	4.6	2.3	230	13.3	31.3	5.98	0.15	846.7	1.59
36	12.2	1.5	8.2	3.0	460	13.3	68.4	2.25	0.32	543.5	0.81
37	12.2	1.8	6.7	2.7	460	13.3	51.1	3.10	0.24	604.8	0.94
38	12.2	2.7	4.6	2.3	460	13.3	31.3	5.98	0.15	893.8	1.25
39	15.2	1.7	9.1	3.2	230	13.3	82.6	1.97	0.32	438.3	1.18
40	15.2	2.0	7.6	2.9	230	13.3	62.6	2.59	0.24	476.0	1.42
41	15.2	2.8	5.5	2.4	230	13.3	39.9	4.41	0.16	637.8	1.78
42	15.2	1.7	9.1	3.2	460	13.3	82.6	1.97	0.32	477.5	0.95

43	15.2	2.0	7.6	2.9	460	13.3	62.6	2.59	0.24	515.2	1.17
44	15.2	2.8	5.5	2.4	460	13.3	39.9	4.41	0.16	673.9	1.42

5.4 Numerical Modeling

The analyses were conducted using the Open System for Earthquake Engineering Simulation (OpenSees 2012) computer software using numerical models similar to the one described in chapter 4. A side of view of the column and foundation part of model is shown in Figure 5.5. Fiber-section nonlinear Euler Bernoulli beam-column (frame) elements were used to model the columns, with 3 integration points per element. Existing material models in OpenSees—*Concrete03* and *Steel02*—were used to model the concrete and steel, respectively. The compressive strength of concrete was 35 MPa, and the yielding stress of steel was 450 MPa with a 2% hardening ratio. Linear elastic stiff elements were used to connect the top of the columns with the centroid of the deck, as well as the foundation centroid with the bottom of the column and the bottom of the foundation.

The soil underneath each shallow foundation was modeled using 289 zero length springs distributed in a non-uniform 17 × 17 grid. The length of the end regions was determined by the A/A_c ratio. The vertical force-displacement relation was modeled using the modified QzSimple1 F-D relation, as described in the previous chapter. The initial stiffness of the vertical springs in the end region was calibrated in order to match the corresponding initial rocking stiffness. The vertical stiffness of the springs in the middle zone was 20% the stiffness the springs of the end regions (K_{ratio} = 5). The capacity of the springs in the end region was equal to $Q_{s,r}$ (see

Table 5.3), whereas the capacity of the springs in the middle zone was equal to $0.5Q_{s,r}$ (Q_{ratio} = 2). The damping coefficient was determined by the elastic rocking radiation damping (Gazetas 1991) for a period equal to $T_{1,s}$. The coefficient was equal for all springs (uniformly distributed along the footing) and is also shown in

Table 5.3. Horizontal springs at the bottom of the footing were used to model the friction (TzSimple1). For simplicity in this study, the passive resistance was not modeled so that the theoretical and numerical foundation moments are identical. The total frictional capacity of the footings was assumed to be 60% of the total weight of the specimens.

The mass was assigned at the centroid of deck and the foundations. The corresponding mass moments of inertia at each of these locations were also assigned. The gravity load was assigned as point loads in the above locations. An initial stiffness Rayleigh damping of 2% was used in first translational mode. Two horizontal directions of excitation were used for the numerical analyses.

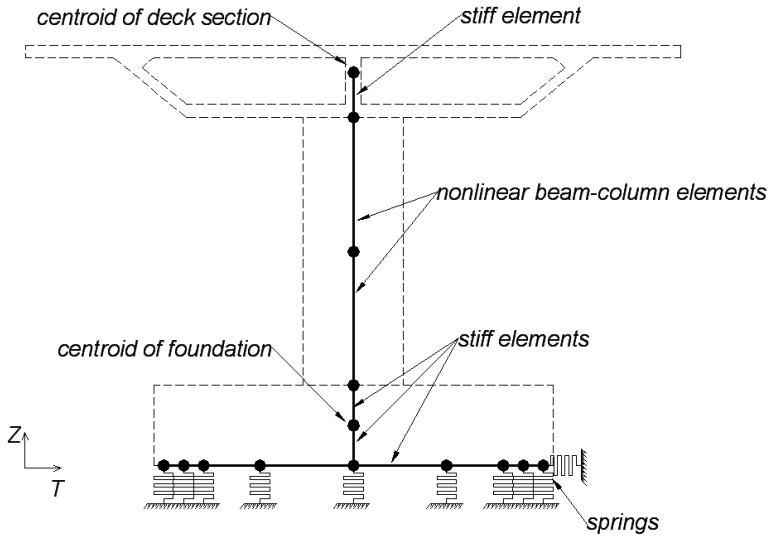

Figure 5.5. Numerical modeling of the bridge piers using OpenSees (drawing and number of springs not to scale).

5.5 Numerical Analysis Results

5.5.1 Seismic demand for the broadband ground motions

For the broadband ground motions, no overturning was reported. The mean displacement demand versus the period of each model is plotted in Figure 5.6. In this figure, the mean displacement spectra of the broadband motions (FN component) are also shown. It can be seen that the recorded displacements are significantly larger than the linear elastic spectrum values, for all period ranges studied here. The mean demand in terms of drift ratio is shown in Figure 5.7, for various ranges of C_r values. The drift ratios were between 0.7% and 2.6%. The drift ratio results for all models and broadband ground motions are shown in Table 5.4. Figure 5.8 plots the computed nonlinear displacement ratio, r_N, versus $T_{1,s}$, for each of the 44 models for each of the forty ground motions. Figure 5.9 plots the mean values of r_N versus $T_{1,s}$ while Figure 5.10 plots the mean values of r_N versus C_r. The calculation of the linear elastic displacement was based on the secant period $T_{1,s}$ and a damping ratio of 2%. Overall both the mean r_N and the scatter decreases with increase of $T_{1,s}$ indicating that for shorter period units (in the specific period range studied and the specific ground motions) the nonlinear response results in a displacement 1.2 – 2.5 times larger than the linear demands for the secant period. For any level of $T_{1,s}$ the nonlinear displacement ratio increases, in general, with decrease of base strength (decrease of C_r). Note the major difference in the mean value of nonlinear displacement ratio that is observed for the systems with $T_{1,s}$ smaller than 0.75 s. For example for the systems with $T_{1,s}$ smaller than 0.65 s and C_r between 0.3 and 0.4 the r_N varies between 1.3 and 2.5. For these four systems only the one with the largest slenderness ratio (equal to 1.5) results in the largest mean r_N (equal to 2.4) indicating the effect of P-Δ on the nonlinear displacement ratio.

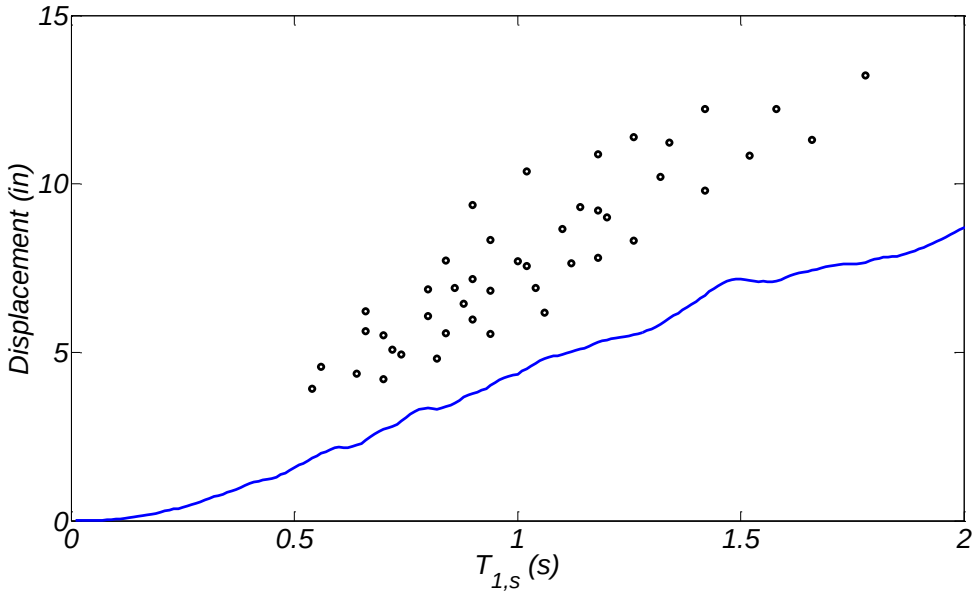

Figure 5.6. Mean displacement demand versus the secant period, $T_{1,s}$, for the broadband ground motions. The mean linear displacement spectrum is also plotted for reference (the maximum value between the FN and FP components was used with a damping ratio equal 2%).

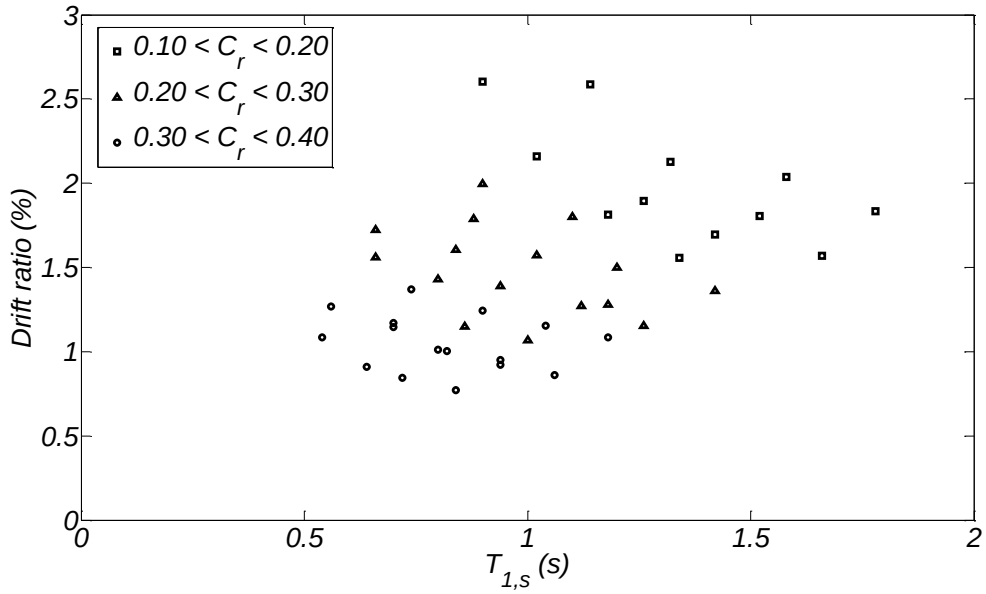

Figure 5.7. Mean drift ratios computed for the broadband ground motions versus the secant period, $T_{1,s}$, for various ranges of C_r.

Table 5.4. Peak drift ratios (%) of the 44 models for each of the 40 broadband ground motions.

Model	C_r	$T_{1,s}$ (s)	Long Valley Dam (Upr. L. Abut)	CHY036	Rio Dell Overpass - FF	Delta	Yarimca	Calipatria Fire Station	CHY034	NST	Duzce	Rio Dell Overpass, E Ground	Gurkasian	Gilroy Array #4	TCU060	Chihuahua	Fremont – Emerson Court	Zack Brothers Ranch	TCU118	TAPS Pump Station #10	El Centro Array #4	Sam Bernandino – E & Hospitality
1	0.39	0.71	0.6	1.1	1.2	1.1	1.8	0.1	1.9	0.8	1.6	0.3	0.4	0.7	0.4	0.4	0.4	1.3	0.3	5.3	1.7	0.4
2	0.26	0.87	0.6	1.7	1.5	2.9	2.2	0.2	2.7	0.7	2.8	0.4	0.9	1.8	1.1	0.6	0.6	2.2	0.4	7.9	3.2	0.7
3	0.16	1.14	0.6	2.5	1.4	2.5	9.5	0.4	2.3	0.7	3.2	0.3	0.9	1.8	1.3	1.1	0.5	1.5	2.4	11.7	6.0	0.9
4	0.39	0.54	0.5	1.2	1.0	1.4	1.4	0.1	1.7	0.8	0.9	0.2	0.4	0.6	0.4	0.4	0.3	1.5	0.2	4.8	1.5	0.4
5	0.26	0.67	0.8	1.3	1.6	1.6	3.1	0.1	2.2	0.7	2.6	0.2	0.7	1.7	0.6	0.6	0.6	2.3	0.5	7.8	2.6	0.4
6	0.16	0.89	0.5	2.5	1.6	2.3	9.9	0.5	3.0	0.5	3.4	0.4	0.8	1.8	1.1	0.8	0.5	1.7	1.1	11.6	6.1	0.8
7	0.39	0.82	0.6	1.1	1.1	0.9	1.4	0.1	1.7	0.5	1.7	0.2	0.5	0.8	0.4	0.3	0.4	1.3	0.3	4.4	1.7	0.4
8	0.26	1.02	0.4	2.2	1.3	1.6	2.1	0.2	2.3	0.5	2.7	0.4	0.7	1.4	0.8	0.5	0.4	1.6	0.4	6.3	2.7	0.5
9	0.16	1.33	0.5	2.2	1.2	2.1	7.8	0.3	2.1	0.7	2.6	0.2	0.7	1.5	0.8	1.0	0.4	1.2	1.7	8.6	5.0	0.7
10	0.39	0.64	0.6	0.8	0.9	0.9	0.7	0.1	1.4	0.7	0.8	0.3	0.4	0.6	0.3	0.3	0.3	1.1	0.2	4.1	1.2	0.2
11	0.26	0.80	0.5	1.2	1.2	2.4	1.9	0.2	1.6	0.7	2.3	0.3	0.7	1.4	0.9	0.4	0.4	1.8	0.3	6.5	2.5	0.6
12	0.16	1.03	0.5	1.9	1.3	2.3	8.5	0.3	2.2	0.5	2.7	0.3	0.7	1.5	0.8	0.9	0.3	1.3	0.7	8.9	5.0	0.8
13	0.39	0.94	0.4	0.8	1.0	0.8	1.6	0.1	1.3	0.4	1.5	0.3	0.6	1.0	0.4	0.4	0.3	1.4	0.3	4.1	1.6	0.3
14	0.28	1.12	0.4	1.8	1.1	1.3	1.7	0.2	1.8	0.4	2.2	0.3	0.6	1.2	0.7	0.5	0.3	1.3	0.4	5.0	2.2	0.5
15	0.16	1.51	0.6	1.6	1.0	2.1	6.6	0.3	1.3	0.4	2.0	0.2	0.5	1.2	0.8	0.8	0.4	1.0	1.6	6.8	4.4	0.7
16	0.39	0.73	0.5	1.0	0.9	0.7	1.4	0.1	1.5	0.4	1.2	0.2	0.3	0.6	0.5	0.3	0.3	1.1	0.2	3.6	1.2	0.4
17	0.28	0.87	0.4	1.0	1.1	1.5	1.7	0.2	1.5	0.5	1.8	0.3	0.6	1.2	0.8	0.4	0.4	1.5	0.3	5.2	2.0	0.5
18	0.16	1.19	0.4	1.7	1.0	1.6	7.5	0.3	1.6	0.6	2.2	0.2	0.6	1.3	0.9	0.8	0.3	1.1	1.0	7.5	4.3	0.6
19	0.39	1.06	0.3	0.9	0.9	0.7	1.3	0.1	1.1	0.4	1.3	0.3	0.5	1.1	0.5	0.3	0.3	1.2	0.2	3.7	1.4	0.3
20	0.29	1.26	0.3	1.3	0.9	1.3	1.4	0.2	1.7	0.3	2.1	0.2	0.4	1.0	0.6	0.5	0.2	1.1	0.4	4.2	1.9	0.4
21	0.18	1.66	0.4	1.1	0.9	1.8	6.4	0.3	1.1	0.5	1.7	0.2	0.4	1.0	0.8	0.7	0.4	0.9	1.3	5.6	3.9	0.6
22	0.39	0.84	0.4	0.8	0.9	0.6	0.9	0.1	1.3	0.3	1.2	0.2	0.5	0.6	0.4	0.2	0.3	1.2	0.2	3.3	1.2	0.3
23	0.29	0.99	0.3	1.2	1.0	1.3	1.5	0.1	1.2	0.3	1.8	0.3	0.5	1.1	0.5	0.4	0.3	1.2	0.4	4.3	1.7	0.4
24	0.18	1.35	0.4	1.5	0.9	1.4	6.7	0.2	1.4	0.3	1.9	0.2	0.4	1.1	0.7	0.8	0.3	0.9	0.8	6.1	3.6	0.5
25	0.34	0.74	0.8	1.4	1.9	1.1	2.0	0.2	2.2	0.5	2.2	0.2	0.5	1.0	0.7	0.4	0.5	2.1	0.4	6.1	2.1	0.6
26	0.24	0.89	0.5	2.5	1.6	2.4	2.4	0.2	2.9	0.7	3.5	0.5	0.9	1.8	1.2	0.7	0.5	2.1	0.6	8.5	3.5	0.7
27	0.34	0.55	0.8	1.1	1.3	1.2	1.0	0.1	1.9	0.9	1.0	0.3	0.5	0.7	0.4	0.5	0.5	1.7	0.3	5.9	1.6	0.3
28	0.24	0.67	0.8	1.6	1.6	1.5	1.9	0.1	3.1	0.7	2.9	0.2	0.7	1.8	0.7	0.6	0.7	2.3	0.4	8.6	2.9	0.4
29	0.33	0.90	0.6	1.0	1.4	1.1	2.0	0.2	1.6	0.6	1.8	0.4	0.7	1.6	0.8	0.4	0.4	1.9	0.3	5.5	2.1	0.5
30	0.23	1.10	0.5	2.2	1.4	2.2	2.2	0.4	2.4	0.6	3.0	0.3	0.6	1.3	1.0	0.8	0.4	1.6	0.6	6.7	3.0	0.5
31	0.33	0.69	0.7	1.3	1.6	1.0	2.1	0.1	1.9	0.4	1.8	0.2	0.4	0.8	0.6	0.3	0.4	1.8	0.3	5.0	1.5	0.5
32	0.23	0.84	0.4	1.9	1.4	2.3	2.0	0.2	2.4	0.5	3.0	0.4	0.8	1.6	0.9	0.5	0.4	1.7	0.5	7.2	2.7	0.6
33	0.32	1.03	0.4	1.2	1.1	1.5	1.7	0.2	1.3	0.5	1.9	0.3	0.6	1.2	0.8	0.4	0.4	1.5	0.3	4.8	1.9	0.4
34	0.24	1.21	0.4	1.7	1.1	1.4	1.8	0.3	2.1	0.4	2.6	0.2	0.5	1.1	0.7	0.6	0.3	1.2	0.5	5.5	2.5	0.5
35	0.15	1.59	0.5	1.6	1.0	2.0	7.9	0.4	1.1	0.6	1.9	0.2	0.5	1.2	1.1	1.0	0.5	1.1	1.3	6.8	5.1	0.8
36	0.32	0.81	0.5	0.8	1.2	0.9	1.2	0.2	1.5	0.4	1.6	0.3	0.6	1.3	0.5	0.4	0.4	1.7	0.3	4.6	1.6	0.4
37	0.24	0.94	0.3	1.9	1.2	1.5	1.8	0.2	2.0	0.4	2.8	0.3	0.6	1.3	0.7	0.4	0.3	1.3	0.4	5.5	2.2	0.5
38	0.15	1.25	0.4	1.7	1.0	1.8	7.3	0.3	1.6	0.5	2.3	0.2	0.5	1.3	0.8	1.1	0.3	1.0	1.0	7.8	4.8	0.6
39	0.32	1.18	0.4	1.4	1.0	0.7	1.4	0.2	1.6	0.3	1.8	0.2	0.4	1.1	0.6	0.6	0.2	1.2	0.4	4.1	1.7	0.4
40	0.24	1.42	0.4	1.6	0.9	1.3	3.0	0.2	1.7	0.3	2.0	0.1	0.4	1.0	0.6	0.6	0.3	1.0	1.0	5.2	2.4	0.6
41	0.16	1.78	0.3	2.0	0.9	1.7	6.5	0.3	1.0	0.5	1.6	0.2	0.5	1.0	0.8	0.9	0.4	0.9	1.5	5.6	4.3	0.7
42	0.32	0.95	0.3	1.2	1.0	0.7	1.6	0.1	1.1	0.4	1.5	0.3	0.5	1.1	0.5	0.3	0.3	1.3	0.2	4.2	1.4	0.3
43	0.24	1.17	0.4	1.6	1.0	1.2	1.4	0.2	1.8	0.3	2.4	0.2	0.5	1.0	0.6	0.6	0.2	1.1	0.3	4.7	2.0	0.5
44	0.16	1.42	0.4	1.3	0.9	1.6	6.5	0.3	1.1	0.5	1.9	0.1	0.5	1.1	0.8	0.7	0.4	0.9	1.9	6.2	4.3	0.7
No. of OT			0	0	0	0	0	0	0	0	0	0	0	0	0	0	0	0	0	0	0	0

Table 5.4 (cont'd)

Model	C_r	$T_{1,s}$ (s)	Yermo Fire Station	Sylmar – Converter Sta	LA – Hollywood Stor FF	Morongo Valley	Hollister – South & Pine	TCU055	CHY025	Brawley Airport	CHY088	Duzce	TCU061	Saratoga – Aloha Ave	El Centro Array #9	TCU123	Jensen Filter Plant	CHY104	Salinas – John & Work	Coyote Lake Dam (Downst)	CHY008	TCU141	No. of OT
1	0.39	0.71	1.3	5.1	0.3	1.6	3.3	1.0	0.9	0.4	0.7	2.2	0.5	1.7	1.0	0.2	3.6	0.3	0.2	0.4	0.3	0.1	0
2	0.26	0.87	1.4	7.6	0.5	3.5	2.7	2.3	1.3	0.6	0.7	2.6	1.3	2.2	1.3	0.5	6.5	0.3	0.3	0.5	0.4	0.2	0
3	0.16	1.14	1.8	6.3	0.9	3.2	2.2	2.3	3.0	1.6	1.0	9.3	2.5	2.2	2.5	0.9	6.3	2.0	0.4	1.0	1.5	0.7	0
4	0.39	0.54	1.3	4.6	0.3	1.1	3.5	0.8	0.8	0.4	0.4	2.4	0.6	0.9	1.1	0.1	4.3	0.2	0.2	0.2	0.3	0.1	0
5	0.26	0.67	1.4	7.4	0.5	2.0	2.7	0.9	1.6	0.5	0.6	2.1	0.6	1.9	1.2	0.5	5.1	0.2	0.3	0.4	0.4	0.2	0
6	0.16	0.89	2.3	7.3	1.1	3.0	2.6	2.4	3.6	1.3	1.2	8.4	2.8	2.0	2.2	0.7	6.8	2.0	0.3	1.1	1.2	0.7	0
7	0.39	0.82	1.0	4.5	0.4	1.3	2.7	0.7	0.8	0.4	0.5	1.4	0.4	1.4	0.8	0.3	2.8	0.2	0.2	0.3	0.3	0.1	0
8	0.26	1.02	2.0	6.7	0.7	2.8	2.1	1.7	1.2	0.7	0.5	2.9	1.7	1.6	1.1	0.4	5.3	0.7	0.2	0.4	0.9	0.2	0
9	0.16	1.33	1.4	5.3	0.7	2.6	2.0	2.1	2.5	1.3	1.0	7.3	1.8	1.7	2.1	0.7	5.2	1.8	0.3	0.9	2.5	0.7	0
10	0.39	0.64	1.1	3.7	0.3	1.4	2.9	0.7	0.7	0.3	0.4	1.9	0.5	1.3	0.9	0.1	3.2	0.2	0.2	0.3	0.3	0.1	0
11	0.26	0.80	1.2	6.0	0.4	2.9	2.2	1.4	0.9	0.5	0.6	2.0	1.1	1.7	1.0	0.4	5.3	0.5	0.3	0.4	0.4	0.2	0
12	0.16	1.03	1.6	6.0	0.8	2.5	2.1	2.5	3.2	1.2	0.8	7.8	2.2	1.7	2.0	0.5	5.6	1.5	0.3	0.9	1.0	0.5	0
13	0.39	0.94	0.9	4.3	0.4	1.0	2.2	0.5	0.8	0.4	0.5	1.4	0.5	1.3	0.7	0.3	2.3	0.2	0.2	0.4	0.3	0.1	0
14	0.28	1.12	1.8	5.0	0.7	2.2	1.8	1.4	1.2	0.6	0.4	2.2	1.0	1.2	0.9	0.3	4.6	0.5	0.2	0.3	0.6	0.2	0
15	0.16	1.51	1.2	4.7	0.5	2.2	1.8	1.7	3.9	1.2	0.9	5.5	1.4	1.5	1.7	0.5	4.4	1.6	0.2	0.8	1.6	0.7	0
16	0.39	0.73	0.7	3.7	0.2	1.1	2.3	0.6	0.7	0.3	0.5	1.4	0.4	1.2	0.7	0.3	2.4	0.2	0.2	0.3	0.2	0.1	0
17	0.28	0.87	1.0	5.2	0.3	2.1	1.9	1.0	1.0	0.4	0.5	1.4	0.7	1.4	0.8	0.3	4.1	0.2	0.2	0.3	0.3	0.1	0
18	0.16	1.19	1.3	5.3	0.6	2.2	1.8	1.6	2.5	1.0	0.6	6.1	1.6	1.5	1.7	0.6	4.8	1.3	0.3	0.7	0.9	0.7	0
19	0.39	1.06	0.9	4.1	0.3	1.0	1.8	0.7	0.8	0.4	0.4	1.2	0.7	1.1	0.7	0.2	2.1	0.3	0.2	0.2	0.2	0.2	0
20	0.29	1.26	1.6	4.4	0.8	2.1	1.6	1.3	1.5	0.6	0.3	2.4	1.0	1.0	0.7	0.3	4.0	0.6	0.2	0.3	0.7	0.3	0
21	0.18	1.66	1.0	4.4	0.5	1.9	1.5	1.5	3.3	1.0	0.9	3.7	1.2	1.3	1.4	0.4	3.9	1.5	0.2	0.6	2.0	0.5	0
22	0.39	0.84	0.7	3.5	0.4	0.9	2.0	0.4	0.7	0.3	0.4	1.3	0.4	1.1	0.7	0.2	1.8	0.2	0.2	0.4	0.2	0.1	0
23	0.29	0.99	1.1	4.4	0.5	2.1	1.6	1.2	0.9	0.4	0.4	1.7	0.7	1.2	0.7	0.3	3.9	0.5	0.2	0.3	0.6	0.2	0
24	0.18	1.35	1.1	4.9	0.5	1.9	1.6	1.4	3.4	0.9	0.5	3.9	1.3	1.4	1.4	0.5	4.1	1.2	0.2	0.7	0.8	0.5	0
25	0.34	0.74	1.2	7.0	0.5	1.8	3.1	0.8	1.2	0.4	0.7	1.9	0.5	2.0	1.0	0.5	3.7	0.3	0.3	0.4	0.4	0.2	0
26	0.24	0.89	1.6	8.7	0.5	3.6	2.7	2.6	2.1	0.7	0.8	3.3	2.4	2.2	1.2	0.4	6.4	0.7	0.3	0.6	0.8	0.2	0
27	0.34	0.55	1.5	6.4	0.3	2.2	3.6	1.2	0.7	0.4	0.6	2.0	0.7	2.0	1.1	0.2	4.5	0.2	0.2	0.3	0.4	0.2	0
28	0.24	0.67	1.5	7.8	0.6	2.3	2.6	1.1	2.4	0.5	0.9	2.1	1.6	2.1	1.3	0.6	6.2	0.4	0.3	0.6	0.5	0.2	0
29	0.33	0.90	1.2	6.2	0.5	1.4	2.5	1.1	1.3	0.5	0.5	1.6	0.4	1.5	1.0	0.4	3.0	0.2	0.2	0.5	0.4	0.2	0
30	0.23	1.10	2.3	6.6	1.2	3.1	2.7	2.2	3.5	0.9	0.6	4.3	1.9	1.6	1.0	0.3	5.0	0.7	0.2	0.6	1.3	0.6	0
31	0.33	0.69	0.9	5.8	0.4	1.5	2.7	0.7	0.9	0.3	0.6	1.5	0.4	1.7	0.9	0.4	2.9	0.2	0.2	0.3	0.3	0.2	0
32	0.23	0.84	1.4	7.1	0.4	2.9	2.1	0.9	1.5	0.6	0.6	2.6	1.8	1.8	1.0	0.4	5.4	0.5	0.3	0.5	0.7	0.2	0
33	0.32	1.03	1.2	5.3	0.4	2.1	2.0	1.0	1.2	0.5	0.5	1.5	0.7	1.3	0.7	0.3	3.4	0.5	0.2	0.3	0.6	0.2	0
34	0.24	1.21	1.8	5.9	1.0	2.6	2.2	1.8	2.9	0.8	0.8	3.5	1.9	1.3	0.8	0.4	4.2	0.6	0.3	0.5	0.9	0.4	0
35	0.15	1.59	1.4	4.2	0.5	2.2	2.0	3.2	5.1	1.5	1.1	6.4	2.6	1.9	1.7	0.5	4.2	2.0	0.3	0.8	2.6	0.8	0
36	0.32	0.81	0.9	5.3	0.4	1.1	2.1	0.5	0.9	0.4	0.5	1.3	0.5	1.4	1.0	0.3	2.2	0.2	0.2	0.5	0.3	0.1	0
37	0.24	0.94	1.7	5.9	0.8	2.5	1.8	1.5	1.5	0.5	0.4	2.5	1.4	1.5	0.9	0.3	4.5	0.5	0.3	0.4	0.7	0.2	0
38	0.15	1.25	1.2	4.9	0.6	2.4	1.6	2.0	3.5	1.1	0.7	6.8	1.5	1.6	1.8	0.6	4.7	1.6	0.3	0.8	1.1	0.6	0
39	0.32	1.18	1.6	4.4	0.8	2.1	1.7	1.2	1.0	0.5	0.3	1.7	0.9	1.0	0.7	0.3	3.7	0.5	0.2	0.3	0.6	0.3	0
40	0.24	1.42	1.4	4.9	0.7	1.9	1.7	1.4	1.9	0.8	0.7	3.0	1.4	1.2	1.3	0.5	3.4	1.0	0.2	0.7	0.9	0.6	0
41	0.16	1.78	1.4	3.9	0.5	1.9	1.8	3.8	4.6	1.2	0.9	5.3	2.9	1.8	1.4	0.5	3.7	1.9	0.7	0.7	2.3	0.6	0
42	0.32	0.95	1.1	4.7	0.3	1.2	1.8	0.8	0.8	0.4	0.4	1.2	0.6	1.2	0.7	0.3	2.5	0.4	0.2	0.3	0.3	0.2	0
43	0.24	1.17	1.6	5.2	0.9	2.3	1.9	1.3	2.3	0.6	0.5	3.1	1.2	1.1	0.7	0.3	3.8	0.6	0.3	0.4	0.6	0.3	0
44	0.16	1.42	1.0	4.6	0.5	2.0	1.5	1.6	4.3	1.0	1.0	5.4	1.4	1.3	1.5	0.4	4.2	1.3	0.2	0.7	1.2	0.5	0
No. of OT			0	0	0	0	0	0	0	0	0	0	0	0	0	0	0	0	0	0	0	0	

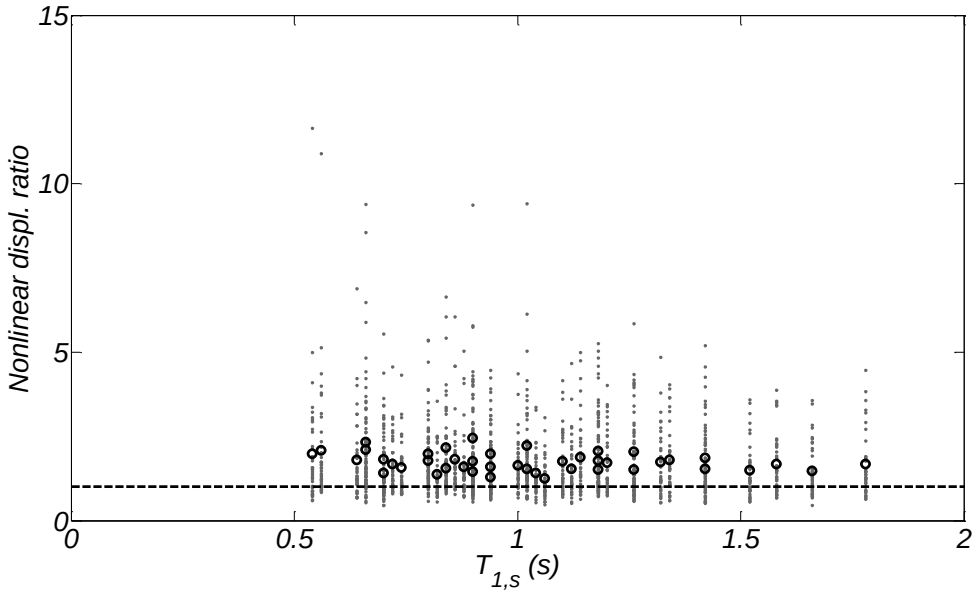

Figure 5.8. Scatter and mean values (in circles) of the nonlinear displacement ratio versus the secant period of the models, $T_{1,s}$, for the broadband records.

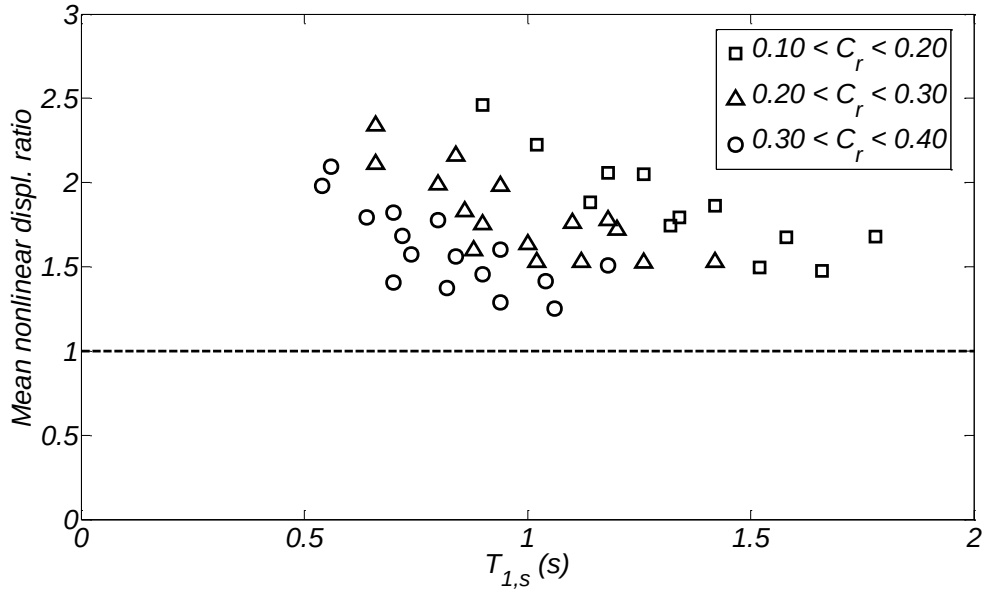

Figure 5.9. Mean nonlinear displacement ratio versus the secant period of the models, $T_{1,s}$, for the broadband records and various ranges of base shear coefficient.

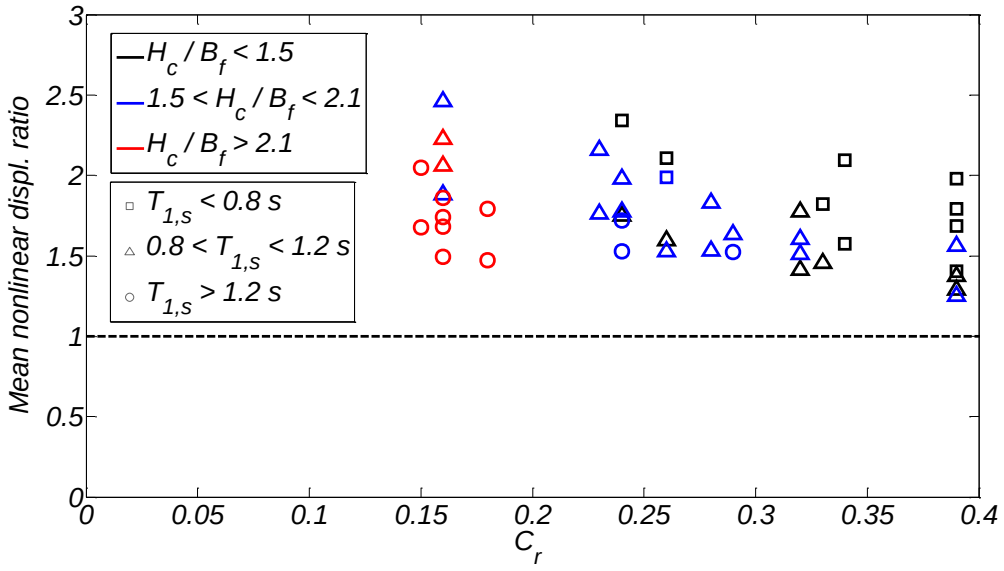

Figure 5.10. Mean nonlinear displacement ratio versus base shear coefficient of the models for the broadband records and various ranges of the secant periods, $T_{1,s}$, and H_c / B_f ratios.

5.5.2 Overturn and seismic demand for the pulse-like ground motions

The displacement demand of each model versus the secant period, T1,s, is shown in Figure 5.11. The mean linear displacement spectra are also shown in this figure for comparison. It can be seen that nonlinear demand is significantly higher than the linear elastic demand for all period ranges studied here. The peak mean displacement demand is on the order of 34 in, for models with periods between 1.3 and 1.8 s. The demand in terms of drift ratio is shown in Figure 5.12, for various ranges of C_r. The mean peak drift ratios for the models studied here ranged between 2.2% and 7%. The drift ratio demand decreased in general with the increase of C_r. The individual peak drift ratios for each model and near-fault ground motion are shown in Table 5.5. In this table the cases of overturn are shown as OT, and a summary of the total number of reported overturns for each motion and model are shown in the far bottom and right rows respectively. Only two motions caused overturns, the TCU068 (10 OT) and TCU065 (2OT), by the 1999 Chi-Chi earthquake in Taiwan. All models that overturned had a C_r value of less than 0.17. Figure 5.13 plots the percentage of overturns versus the base shear coefficient of each model for the 40 near-fault pulse-like ground motions grouped in terms of W_s and K_{init}/M_r ratio. As mentioned before, overturns were observed for C_r larger than 0.17.

Figures 5.14 to 5.16 plot the percentage of overturn that each motion caused to the 44 models versus the period, the energy, and the area of the predominant (1^{st}) pulse of each motion. As shown in Figure 5.14 the percentage of overturns depends on both the predominant pulse period as well as the amplitude of the pulse (at different ranges of T_p only some of the pulses cause overturns). The percentage of overturn in general increased with increase of pulse energy and increase of pulse area. The motion (TCU068) that caused the most overturns includes the pulses with the largest area and energy ever recorded.

Figure 5.17 plots the individual as well as the mean nonlinear displacement ratios, r_N, for each of the 44 models subjected to the 40 near-fault pulse-like ground motions. Figures 18 and 19 plot the mean values of r_N, for different ranges of C_r, H_c / B_f ratios and secant periods. The ratio r_N decreases very fast with increase of $T_{1,s}$ (for $T_{1,s}$ smaller than 1 s) and becomes less than 2.0 for $T_{1,s}$ larger than 1.5 s. For $T_{1,s}$ between 0.7 and 1.5, r_N varies between 3.5 and 1.5.

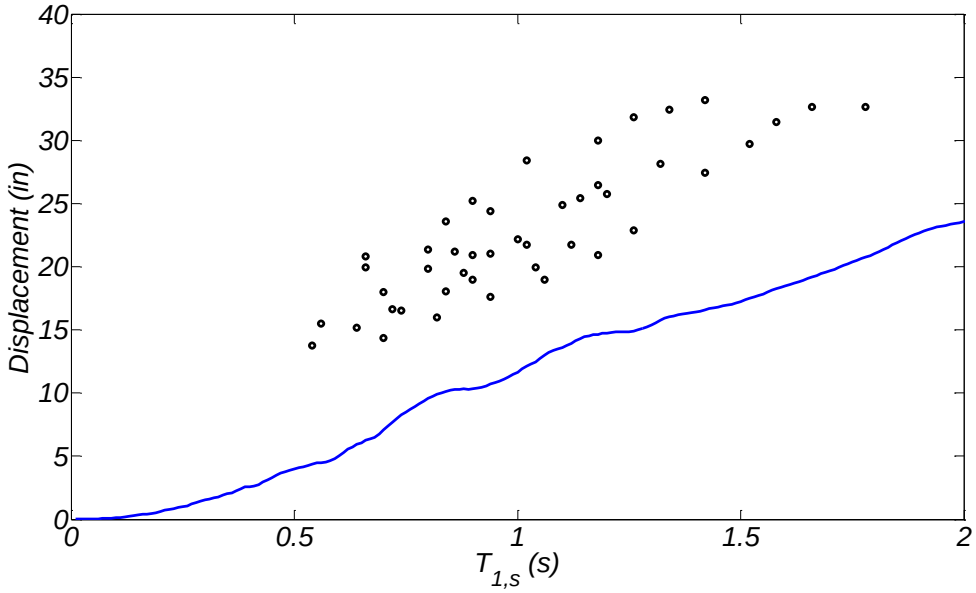

Figure 5.11. Mean displacement demand versus the secant period, $T_{1,s}$, for the near-fault pulse-like ground motions. The mean linear displacement spectrum is also plotted for reference (the maximum value between the FN and FP components was used with a damping ratio equal 2%).

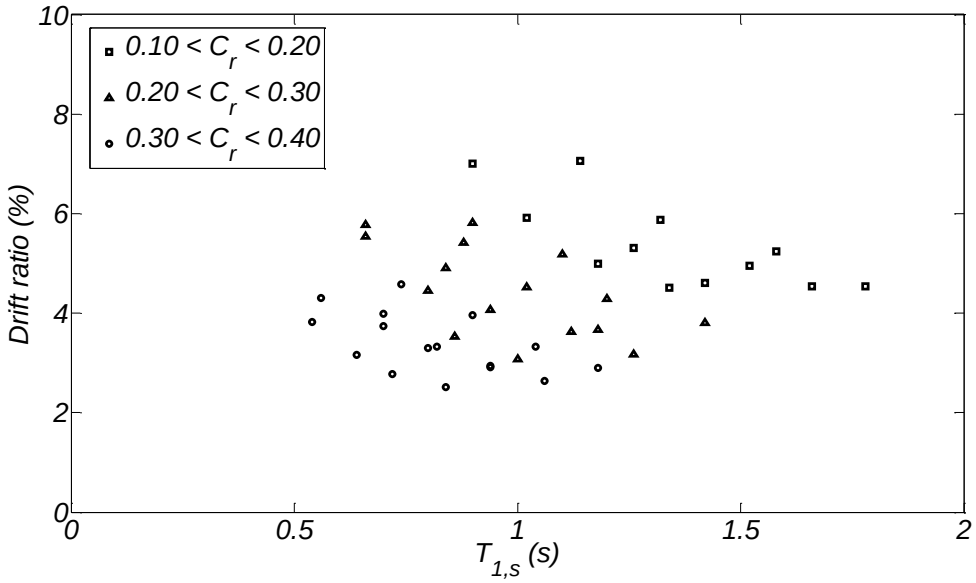

Figure 5.12. Mean drift ratios computed for the near-fault pulse-like ground motions versus the secant period, $T_{1,s}$, for various ranges of C_r. The cases that lead to overturn were ignored.

Table 5.5. Peak drift ratios (%) of the 44 models for each of the 40 near-fault pulse-like ground motions.

Model	C_r	$T_{1,s}$ (s)	PRPC	Pleasant Valley P.P. - Yard	Parachute Test Site	EC Meloland Overpass FF	El Centro Array #7	El Centro Array #6	El Centro Array #5	El Centro Array #4	Pacoima Dam	Erzincan	Sylmar - Converter Sta East	Sylmar Olive View Med FF	Sylmar - Converter Sta	Jensen Filter Plant	Newhall W. Pico Canyon Rd	Newhall Fire Station	Rinaldi Receiving Station	Pacoima Dam	Takarazuka	KJMA
1	0.39	0.71	7.4	1.6	8.4	2.0	2.0	1.7	1.6	1.7	4.5	4.0	3.4	5.7	4.9	6.4	5.0	3.4	5.6	2.6	3.9	3.9
2	0.26	0.87	6.8	1.7	9.8	6.2	7.0	6.0	3.5	3.2	4.1	6.8	3.7	6.4	7.5	10.2	6.9	3.7	4.6	2.4	3.9	3.7
3	0.16	1.14	7.2	1.4	6.4	7.6	8.6	12.9	7.2	6.1	4.7	5.8	6.5	5.7	6.2	7.7	10.4	3.4	5.0	1.7	3.5	4.3
4	0.39	0.54	7.9	1.9	9.0	1.6	1.6	1.1	2.0	1.5	5.0	2.9	3.5	4.4	4.7	6.6	3.4	4.0	6.2	2.9	4.0	3.7
5	0.26	0.67	7.9	1.9	10.3	6.0	6.7	4.9	2.3	2.6	4.0	7.1	4.5	6.7	7.3	10.6	7.0	3.8	5.3	3.0	3.9	3.9
6	0.16	0.89	7.6	1.4	6.1	8.4	9.1	12.7	8.4	6.0	4.7	6.1	6.7	6.0	7.3	7.9	10.0	2.9	4.3	1.8	3.6	4.1
7	0.39	0.82	6.0	1.3	6.1	1.9	1.8	1.6	1.4	1.7	3.5	3.5	2.9	5.3	4.4	5.6	4.3	2.5	4.5	2.1	3.2	3.2
8	0.26	1.02	5.3	1.4	7.5	5.3	6.0	5.7	4.2	2.7	3.3	5.4	3.7	5.2	6.7	8.1	5.2	3.0	3.5	1.7	3.2	2.7
9	0.16	1.33	5.9	1.1	5.9	5.9	7.1	10.2	6.2	5.1	3.8	4.7	5.2	4.5	5.2	6.1	8.1	2.9	4.5	1.4	2.8	3.6
10	0.39	0.64	6.3	1.4	7.2	1.5	1.5	1.1	1.4	1.2	3.9	3.1	2.5	4.1	3.6	4.6	3.6	3.1	4.8	2.3	3.3	3.3
11	0.26	0.80	5.9	1.5	8.0	5.2	6.1	4.4	2.5	2.5	3.3	5.8	3.3	5.5	6.0	8.5	5.6	3.0	4.0	2.1	3.2	3.1
12	0.16	1.03	6.3	1.1	5.3	6.6	7.4	10.0	6.6	5.0	3.8	4.8	5.5	4.9	6.0	6.3	8.2	2.5	3.9	1.5	2.8	3.4
13	0.39	0.94	5.0	1.0	5.2	1.9	1.8	1.4	1.2	1.6	2.8	3.4	2.7	4.7	4.3	5.3	3.7	1.8	3.7	1.7	2.7	2.7
14	0.28	1.12	4.5	1.2	6.2	4.3	4.6	4.3	2.3	2.2	2.7	4.6	2.8	4.4	5.0	6.3	4.1	2.4	3.0	1.4	2.7	2.3
15	0.16	1.51	5.0	0.9	5.3	4.9	6.0	8.6	5.5	4.3	3.1	3.9	4.3	3.6	4.7	5.1	6.7	2.6	3.9	1.2	2.3	2.9
16	0.39	0.73	5.3	1.2	5.0	1.4	1.4	1.2	1.1	1.2	3.2	2.9	2.1	4.8	3.6	4.6	3.5	2.5	4.0	1.8	2.8	2.9
17	0.28	0.87	5.1	1.3	6.2	3.9	4.2	2.4	1.5	2.0	2.7	4.8	2.9	4.6	5.1	6.8	4.4	2.4	3.4	1.7	2.7	2.7
18	0.16	1.19	5.4	1.0	4.6	5.5	6.4	8.1	5.5	4.3	3.1	3.8	4.5	4.3	5.2	5.2	6.6	2.2	3.4	1.2	2.3	2.9
19	0.39	1.06	4.2	1.0	4.5	2.0	1.9	1.1	1.1	1.4	2.3	3.1	2.7	4.2	4.1	4.9	3.0	1.5	3.3	1.6	2.3	2.3
20	0.29	1.26	3.8	1.0	5.5	3.7	4.0	3.9	2.2	1.9	2.2	3.9	2.8	3.8	4.4	5.2	3.6	2.0	2.5	1.2	2.3	1.9
21	0.18	1.66	4.4	0.8	4.2	4.4	5.2	7.1	4.5	3.9	2.6	3.3	3.7	3.3	4.4	4.4	5.6	2.2	3.3	1.0	2.0	2.5
22	0.39	0.84	4.6	1.0	4.6	1.4	1.3	1.1	1.0	1.2	2.7	2.8	1.9	4.5	3.5	4.4	3.0	2.0	3.4	1.6	2.4	2.5
23	0.29	0.99	4.3	1.1	5.6	3.6	3.5	2.4	1.2	1.7	2.2	4.2	2.4	4.1	4.4	5.7	3.3	2.0	2.9	1.3	2.4	2.3
24	0.18	1.35	4.6	0.8	4.5	4.7	5.4	6.6	5.0	3.6	2.6	3.4	3.8	3.7	4.8	4.7	5.4	1.9	3.0	1.1	2.0	2.4
25	0.34	0.74	7.9	1.9	8.0	2.8	2.8	2.3	1.9	2.1	4.3	5.2	4.4	7.9	6.8	8.7	6.0	2.8	5.7	2.5	4.1	4.2
26	0.24	0.89	7.1	1.9	10.3	7.0	7.9	7.4	5.0	3.5	4.3	6.8	4.6	6.5	8.8	10.4	7.1	4.0	4.3	2.2	3.9	3.6
27	0.34	0.55	8.4	2.1	9.8	2.1	1.9	1.3	1.6	1.6	4.9	4.5	3.2	7.9	6.2	7.9	4.4	3.7	6.1	2.9	4.1	3.9
28	0.24	0.67	8.0	1.9	10.6	6.5	8.1	6.6	3.3	2.9	4.2	7.3	4.0	6.9	7.6	10.7	7.4	3.9	5.2	2.8	3.9	3.9
29	0.33	0.90	6.3	1.6	6.9	3.1	3.2	1.8	1.6	2.1	3.2	5.1	4.0	6.4	6.1	7.6	4.9	2.5	4.4	2.4	3.3	3.3
30	0.23	1.10	5.8	1.4	8.4	6.0	6.6	6.3	5.2	3.1	3.4	5.3	5.1	5.3	6.7	8.1	5.7	2.9	3.5	1.6	3.1	2.6
31	0.33	0.69	6.8	1.6	6.7	2.1	1.8	1.7	1.5	1.5	3.7	4.3	3.2	6.7	5.7	7.3	4.8	2.6	4.9	2.2	3.4	3.4
32	0.23	0.84	6.2	1.6	8.6	6.2	6.9	6.1	4.1	2.7	3.5	5.9	3.8	5.5	7.1	8.6	5.6	3.3	3.7	1.8	3.2	3.0
33	0.32	1.03	5.0	1.3	6.1	3.3	3.2	1.7	1.4	1.9	2.5	4.6	3.0	5.2	5.2	6.4	3.9	2.3	3.4	1.8	2.8	2.6
34	0.24	1.21	4.7	1.1	6.6	5.1	5.6	5.4	4.0	2.5	2.8	4.6	4.5	4.6	5.9	6.8	4.7	2.3	2.8	1.4	2.6	2.1
35	0.15	1.59	5.9	0.9	6.2	4.7	6.1	9.3	6.5	5.1	3.2	4.2	4.4	3.5	4.2	5.2	6.9	3.0	4.0	1.2	2.3	3.0
36	0.32	0.81	5.7	1.4	5.8	2.2	2.4	1.5	1.3	1.6	2.9	4.3	3.0	5.5	5.2	6.5	4.1	1.9	3.9	2.0	2.8	2.8
37	0.24	0.94	5.2	1.3	6.5	4.9	5.8	4.9	2.8	2.2	2.8	5.0	3.1	4.8	5.8	7.4	4.2	2.7	3.1	1.5	2.7	2.5
38	0.15	1.25	5.5	1.0	5.9	5.6	6.6	9.1	5.0	4.7	3.1	3.9	4.7	4.1	4.8	5.4	7.0	2.4	3.9	1.2	2.2	3.1
39	0.32	1.18	4.1	1.0	5.0	3.5	3.0	2.5	1.2	1.7	2.1	4.0	2.2	4.4	4.4	5.5	3.3	2.0	2.8	1.3	2.4	2.2
40	0.24	1.42	3.8	0.9	5.2	4.4	4.8	4.6	4.2	2.4	2.4	3.9	3.5	4.0	4.9	5.5	4.4	1.8	2.5	1.1	2.2	2.0
41	0.16	1.78	4.9	0.8	5.2	4.1	5.3	7.8	5.7	4.3	2.7	3.6	3.8	3.1	3.8	4.4	5.8	2.7	3.3	1.0	1.9	2.6
42	0.32	0.95	4.8	1.2	5.1	2.3	2.5	1.1	1.1	1.4	2.4	4.1	2.9	4.8	4.6	5.8	3.1	1.8	3.2	1.8	2.5	2.5
43	0.24	1.17	4.3	1.0	6.2	4.5	5.1	4.7	3.0	2.0	2.3	4.2	4.1	4.2	5.2	6.1	3.8	2.1	2.6	1.2	2.3	2.0
44	0.16	1.42	4.9	0.8	5.1	4.8	5.7	7.7	4.5	4.2	2.6	3.4	4.1	3.5	4.6	4.6	5.8	2.1	3.4	1.0	1.9	2.6
No. of OT			0	0	0	0	0	0	0	0	0	0	0	0	0	0	0	0	0	0	0	0

Table 5.5 (cont'd)

Model	C_r	T_{Ls} (s)	Takatori	LGPC	Cape Mendocino	Petrolia	Duzce	Lucerne	Tabas	Sakarya	Yarimca	TCU068	TCU065	TCU067	TCU052	TCU075	TCU102	CHY080	CHY028	TCU072	Alyeska Pump Station 10	Mianzuqing ping	No. of OT
1	0.39	0.71	8.8	3.7	2.0	2.2	2.2	1.5	5.3	1.4	1.8	10.3	6.5	2.9	9.7	0.6	4.1	5.3	2.1	1.8	5.2	1.6	0
2	0.26	0.87	6.1	4.9	2.5	3.2	2.7	3.0	3.9	3.3	2.2	14.1	9.0	5.2	17.9	1.8	9.0	5.7	2.2	2.5	7.8	1.7	0
3	0.16	1.14	6.3	6.7	4.5	3.8	9.4	9.0	12.3	4.1	9.8	OT	OT	5.3	19.1	9.3	13.5	4.6	4.0	3.2	11.3	9.6	2
4	0.39	0.54	9.1	3.8	1.4	1.9	2.4	1.5	3.4	1.6	1.4	9.1	6.9	3.0	10.0	0.7	2.1	4.6	2.8	2.6	4.7	2.0	0
5	0.26	0.67	6.7	4.8	2.4	2.8	2.1	1.5	4.8	2.9	3.1	18.6	8.1	4.9	19.3	1.6	9.1	5.8	2.0	2.2	7.7	1.8	0
6	0.16	0.89	6.5	6.5	4.2	3.7	8.3	8.7	11.5	2.9	9.7	OT	OT	6.7	19.0	7.3	13.1	4.8	4.3	3.0	11.3	10.0	2
7	0.39	0.82	7.9	3.0	1.7	2.0	1.5	0.9	4.4	1.1	1.4	8.9	5.2	2.2	8.2	0.6	4.2	4.3	1.6	1.8	4.4	1.2	0
8	0.26	1.02	4.9	3.9	2.2	2.6	2.9	3.0	3.8	2.9	2.1	11.8	7.7	4.8	14.7	1.5	6.7	3.9	2.0	2.2	6.2	1.7	0
9	0.16	1.33	5.5	6.0	3.7	3.2	7.3	6.8	10.5	3.9	8.0	OT	14.3	4.1	13.1	7.5	9.4	3.6	3.6	2.4	8.4	7.4	1
10	0.39	0.64	7.2	3.1	1.5	1.6	1.8	1.2	4.0	1.4	0.7	7.8	6.1	2.5	8.0	0.4	2.2	4.2	2.0	1.6	4.1	1.3	0
11	0.26	0.80	5.2	4.2	2.0	2.5	1.9	2.5	3.4	2.6	1.9	11.7	5.1	4.2	15.9	1.5	7.6	4.6	2.3	2.0	6.4	1.3	0
12	0.16	1.03	5.3	5.1	3.7	3.0	7.8	7.2	10.6	2.6	8.3	OT	14.8	4.9	13.1	6.9	9.7	3.8	3.4	2.7	8.7	7.4	1
13	0.39	0.94	7.1	2.7	1.5	1.8	1.4	0.8	3.6	1.0	1.6	7.7	4.0	2.1	7.0	0.6	4.3	3.5	1.3	1.5	4.1	1.0	0
14	0.28	1.12	4.4	3.3	1.8	2.1	2.2	2.2	3.2	2.3	1.7	9.0	6.2	3.8	11.6	1.3	5.5	3.5	1.8	1.7	5.0	1.2	0
15	0.16	1.51	4.6	5.4	3.2	2.7	5.5	5.8	9.0	3.2	6.7	OT	11.7	3.4	12.5	6.6	7.5	2.8	3.1	1.8	6.7	6.1	1
16	0.39	0.73	5.8	2.5	1.4	1.5	1.4	0.9	3.7	0.9	1.4	6.8	5.1	1.9	7.2	0.4	2.9	3.5	1.5	1.1	3.6	1.0	0
17	0.28	0.87	4.8	3.2	1.6	2.0	1.3	1.8	2.9	1.9	1.7	8.9	3.6	3.4	12.9	1.2	5.7	3.7	1.9	1.7	5.1	0.9	0
18	0.16	1.19	4.7	4.1	3.1	2.5	6.1	6.3	9.1	2.7	7.4	OT	11.8	3.6	12.7	5.9	7.9	3.0	2.9	2.2	7.4	5.9	1
19	0.39	1.06	6.1	2.5	1.4	1.6	1.2	1.2	3.0	1.0	1.3	6.8	3.3	2.4	6.3	0.7	3.8	3.0	1.3	1.4	3.7	0.8	0
20	0.29	1.26	3.7	2.9	1.5	1.8	2.5	2.0	2.8	1.9	1.4	7.9	5.4	3.5	10.3	1.4	4.6	2.8	1.7	1.7	4.2	1.2	0
21	0.18	1.66	4.0	4.6	2.8	2.3	3.7	4.8	7.5	2.5	6.3	16.4	9.5	3.6	12.6	5.4	6.3	2.3	2.5	1.4	5.5	4.8	0
22	0.39	0.84	6.3	2.2	1.2	1.4	1.3	0.6	3.3	0.9	0.9	6.5	3.6	1.6	6.4	0.5	3.0	3.0	1.3	1.4	3.3	0.9	0
23	0.29	0.99	4.3	2.8	1.5	1.7	1.7	1.9	2.7	1.7	1.5	7.8	3.8	3.3	10.4	1.1	4.7	3.4	1.4	1.7	4.3	0.7	0
24	0.18	1.35	4.0	3.8	2.5	2.1	3.9	4.9	7.4	2.5	6.7	16.5	8.9	3.3	11.2	4.1	6.6	2.3	2.7	1.8	6.0	4.9	0
25	0.34	0.74	11.3	4.3	2.2	2.6	1.9	1.3	4.9	1.9	2.0	13.9	5.8	3.0	10.7	0.9	6.7	5.7	2.0	2.2	6.1	1.7	0
26	0.24	0.89	6.8	5.4	2.6	3.3	3.3	3.8	4.5	3.8	2.4	16.2	9.0	6.0	17.3	1.7	9.0	4.8	2.4	3.1	8.4	2.5	0
27	0.34	0.55	9.0	4.1	1.7	2.0	2.0	1.5	5.0	1.8	1.0	13.0	5.4	3.9	10.6	0.7	3.9	5.6	2.6	2.4	5.9	1.7	0
28	0.24	0.67	6.9	5.4	2.5	2.9	2.0	1.7	3.9	3.6	1.9	18.8	8.1	5.0	19.7	2.0	10.2	5.6	2.0	2.6	8.5	1.8	0
29	0.33	0.90	8.2	3.7	1.8	2.3	1.6	1.3	4.4	1.8	2.0	11.0	5.0	4.3	9.0	1.1	6.0	4.5	1.6	1.9	5.5	1.4	0
30	0.23	1.10	5.2	5.2	2.3	2.7	4.3	4.1	9.4	3.0	2.1	14.1	8.8	5.5	15.2	2.5	7.8	3.4	3.0	2.6	6.6	3.4	0
31	0.33	0.69	9.4	3.3	1.7	1.9	1.6	1.1	4.0	1.3	2.1	9.9	5.7	2.4	9.1	0.6	5.2	4.2	1.7	2.0	5.0	1.5	0
32	0.23	0.84	5.4	4.9	2.1	2.6	2.7	3.2	3.8	3.1	2.0	13.8	8.3	5.0	16.2	1.5	7.5	4.3	1.9	2.1	7.1	1.9	0
33	0.32	1.03	6.0	3.2	1.7	2.0	1.4	1.9	3.1	1.7	1.7	8.7	3.8	3.7	7.8	1.1	5.2	3.6	1.6	1.7	4.8	0.8	0
34	0.24	1.21	4.3	3.9	1.9	2.3	3.5	3.0	6.9	2.4	1.8	11.1	7.6	4.5	13.8	2.2	6.2	2.7	2.8	2.2	5.4	3.1	0
35	0.15	1.59	4.6	5.9	3.1	2.8	6.4	6.1	10.1	2.7	8.0	OT	12.9	3.5	12.5	7.1	8.1	2.8	2.8	1.7	6.7	7.0	1
36	0.32	0.81	6.7	2.9	1.4	1.8	1.3	0.9	3.7	1.3	1.2	10.4	5.1	2.8	7.7	0.6	4.6	3.6	1.4	1.6	4.5	1.3	0
37	0.24	0.94	4.7	4.0	1.8	2.1	2.5	2.8	3.4	2.5	1.8	10.7	6.9	4.3	15.0	1.3	6.4	3.1	1.8	2.0	5.4	1.1	0
38	0.15	1.25	4.8	4.9	3.3	2.6	6.9	6.6	10.0	3.3	7.5	OT	13.8	3.6	11.6	7.2	8.5	3.0	3.2	2.1	7.6	7.1	1
39	0.32	1.18	4.8	2.7	1.5	1.7	1.7	1.8	2.8	1.8	1.4	6.8	3.3	3.2	7.2	1.1	4.3	3.3	1.6	1.6	4.0	0.8	0
40	0.24	1.42	3.7	4.2	1.7	2.0	3.0	2.8	6.5	1.9	3.0	9.7	6.9	3.5	12.0	2.3	5.6	2.4	2.6	1.7	5.1	2.9	0
41	0.16	1.78	3.9	5.0	2.7	2.4	5.4	5.6	8.8	2.0	6.6	OT	11.5	3.0	12.6	6.4	6.6	2.5	2.1	1.4	5.5	6.2	1
42	0.32	0.95	5.4	2.8	1.3	1.5	1.2	1.6	2.9	1.1	1.6	8.4	3.9	3.2	6.9	0.8	4.1	3.1	1.5	1.4	4.2	0.9	0
43	0.24	1.17	4.2	3.4	1.6	1.9	3.1	2.5	3.8	2.0	1.4	9.5	5.1	3.9	13.3	1.6	5.4	2.4	2.5	2.0	4.6	1.6	0
44	0.16	1.42	4.2	4.4	2.9	2.3	5.5	5.7	8.5	2.8	6.4	OT	10.4	3.0	14.2	6.2	6.9	2.4	2.8	1.7	6.1	6.0	1
No. of OT			0	0	0	0	0	0	0	0	0	10	2	0	0	0	0	0	0	0	0	0	

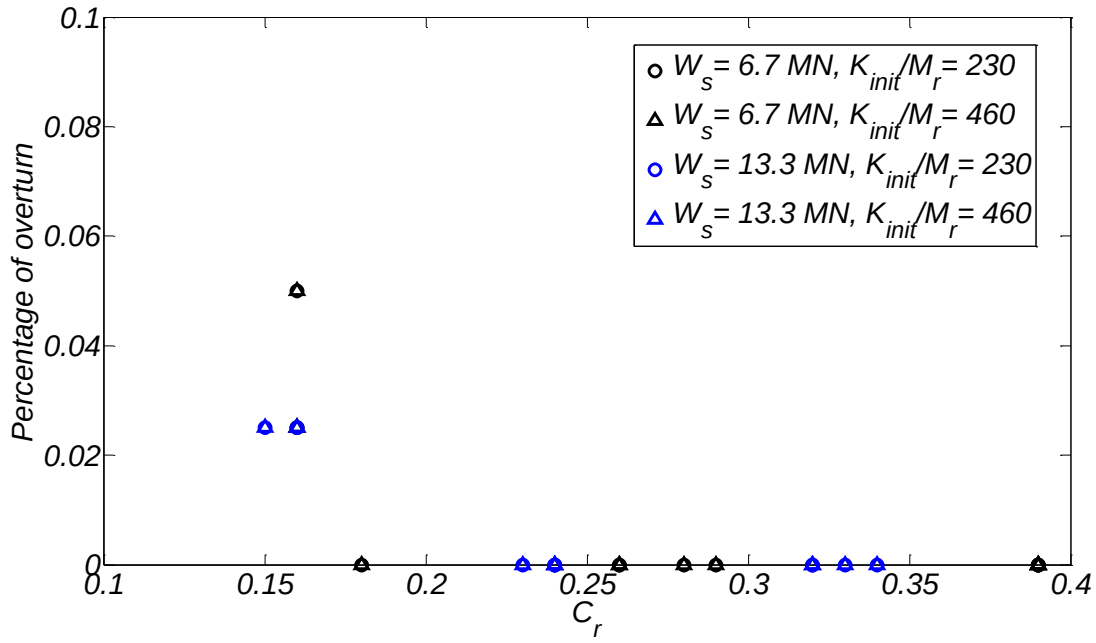

Figure 5.13. Percentage of overturn versus rocking shear coefficient for the near-fault pulse-like ground motions for different soil conditions and superstructure weights.

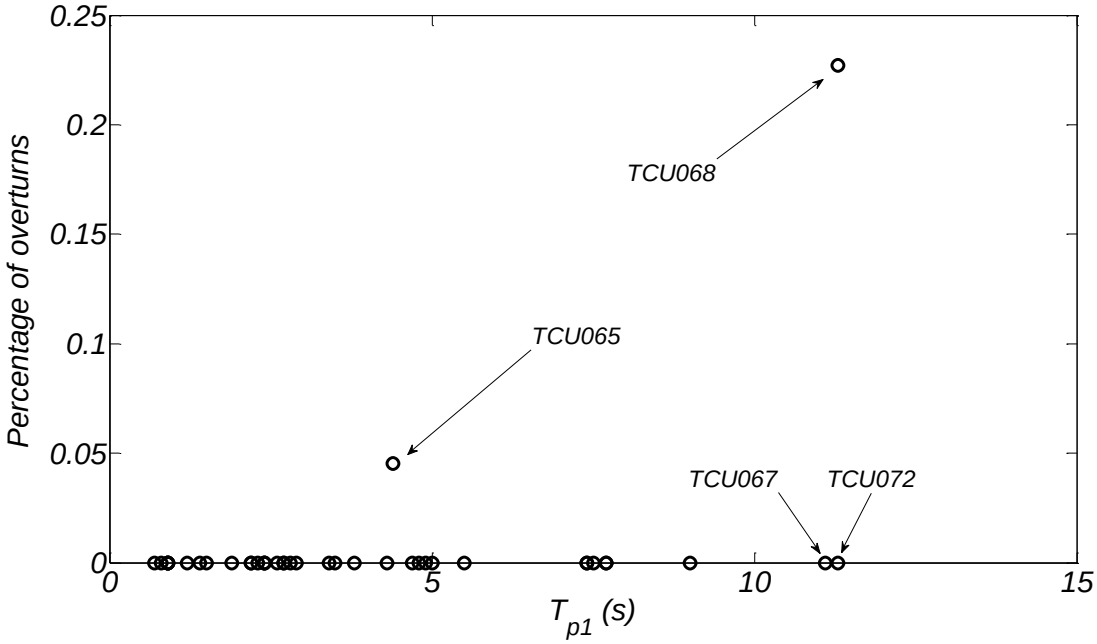

Figure 5.14. Percentage of overturns versus period of the predominant pulse for the near-fault pulse-like ground motions.

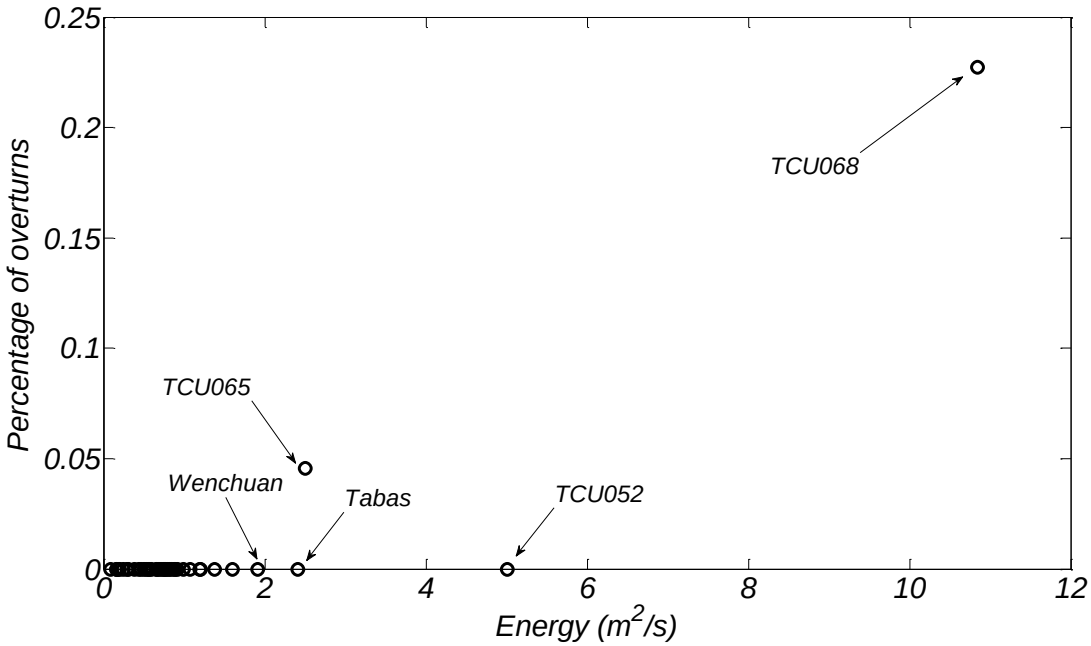

Figure 5.15. Percentage of overturns versus the energy of the predominant pulse for the near-fault pulse-like ground motions.

.

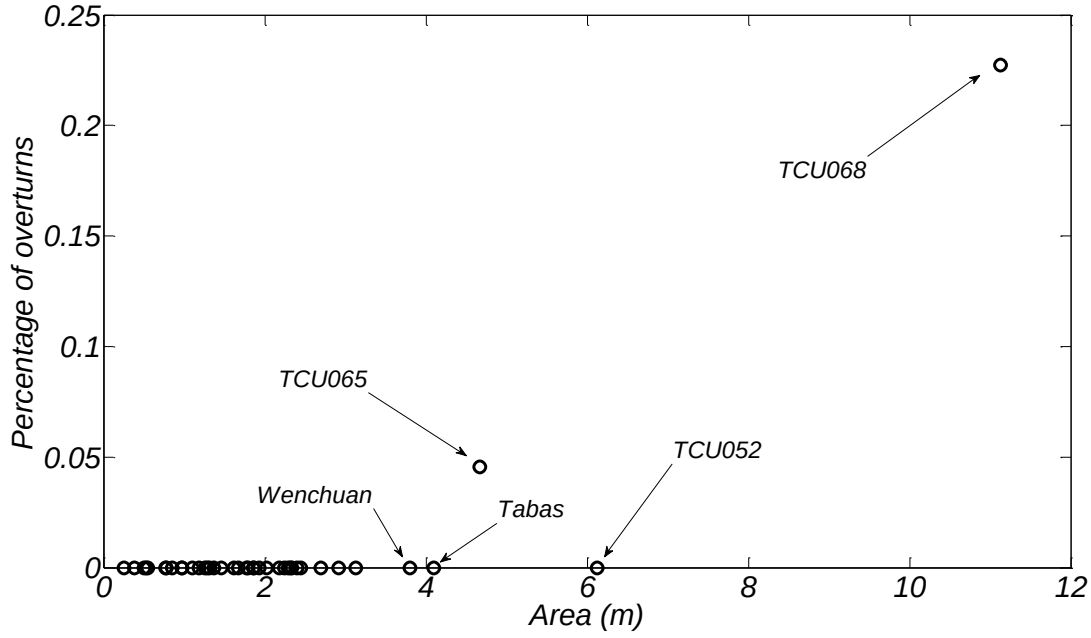

Figure 5.16. Percentage of overturns versus the area of the predominant pulse for the near-fault pulse-like ground motions.

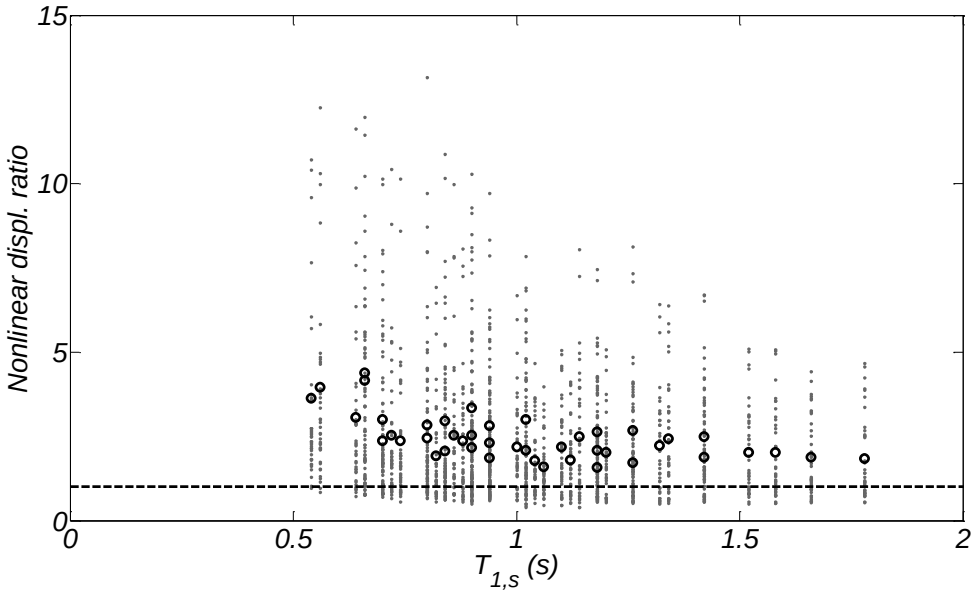

Figure 5.17. Scatter and mean values (in circles) of the nonlinear displacement ratio versus the secant period of the models, $T_{1,s}$, for the near-fault pulse-like ground motions.

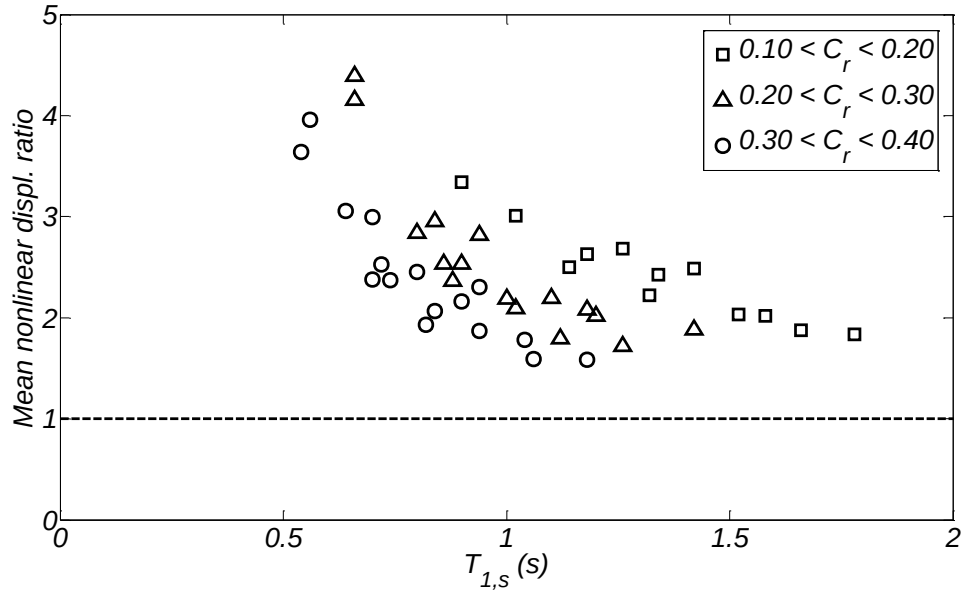

Figure 5.18. Mean nonlinear displacement ratio versus the secant period of the models, $T_{1,s}$, for the near-fault pulse-like ground motions and various ranges of base shear coefficient.

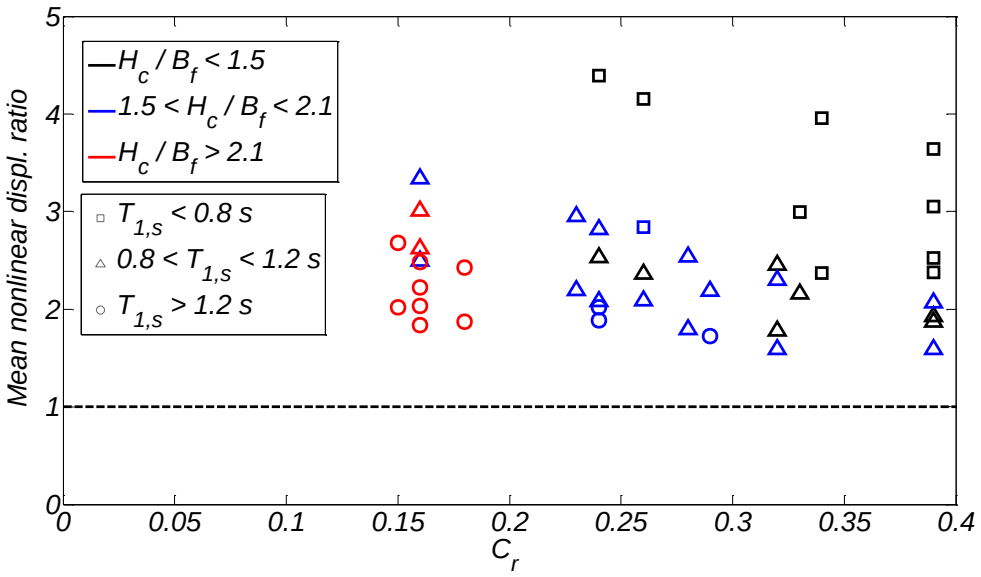

Figure 5.19. Mean nonlinear displacement ratio versus base shear coefficient of the models for the near-fault pulse-like ground motions and various ranges of fundamental periods and H_c / B_f ratios.

5.6 Conclusions

This section presented the three-dimensional seismic response of 44 bridge foundation-column-mass models subject to two sets of ground motions (40 motions per set). The first set included broadband ground motions that result in mean linear spectral demands similar to those expected for a M7 earthquake event at 10 km from the fault plane. The second set included near-fault pulse-like ground motions including these with the highest peak ground velocities and spectral demands at "long" periods that have ever been recorded. The parameters investigated are the bridge column height (6.1 m < H_c < 15.2 m), the foundation width (3 m < B_f < 9.1 m), the ratio of the initial rocking stiffness to the foundation moment capacity (K_{init}/M_r), and the weight of the superstructure (W_s). The peak nonlinear displacement response and the ratio of that to the corresponding linear spectral demand (nonlinear displacement ratio) were computed, as well as the cases of overturn. The following main conclusions were drawn:

1. No overturn was caused by the broadband ground motions and only 12 cases of overturn occurred by the near-fault pulse-like ground motions (out of a total of 1760 cases). The overturns were caused by only two motions, the TCU068 and the TCU065 records by the 1999 Chi-Chi earthquake in Taiwan. All models that overturned had a rocking shear coefficient of less than 0.17.
2. The mean nonlinear displacement for the near-fault pulse-type ground motions was ranged between 13 and 34 in. The corresponding mean drift ratios were between 2.2% and 7.0%. The nonlinear displacement ratios

increased rapidly for periods of less than 0.7 s and it was equal to about 2 for periods larger than 1.5 s.

3. For the broadband ground motions the mean nonlinear displacement of each model ranged between 4 and 14 in. In terms of drift ratio, the mean response was between 0.7% and 2.6%. The nonlinear displacement ratios ranged between 1.2 and 2.5 for the period range studied here. The nonlinear displacement ratios were about 1.5 for periods larger than 1.5 s.

Chapter 6: Conclusions

The objectives of this dissertation were to investigate the use of rocking foundations in bridges for enhanced seismic design and performance and the reduction of post-earthquake damage. The seismic response of bridge systems was studied numerically using three-dimensional nonlinear models, and bridge columns with rocking foundations and superstructure mass were studied both numerically and experimentally. The experimental part consisted of the shake-table testing of large scale bridge columns with shallow rocking foundations using physical modeling of the underlying soil. The numerical studies used three-dimensional models with Winkler springs. The proposed model was modified and validated for rocking shallow foundations designed with high factors of safety against vertical loads, using the date from the large scale shake-table test.

6.1 Numerical analyses of bridges with rocking foundations

The second chapter of this dissertation presented the numerical investigation of the seismic response of six reinforced concrete bridges. All bridges were 210 m long, linear, and had 5 spans. Three of the bridges analyzed were 17 m tall and three were 8 m tall. For each bridge height, three designs of columns and foundations were studied: (a) a conventional bridge designed according to Caltrans seismic design criteria that is expected to develop flexural plastic hinges in columns fixed to pile foundations and the foundation fixed to the ground; (b) columns designed to remain nominally elastic and fixed on rocking pile foundations; and (c) columns designed to remain nominally elastic and fixed to rocking shallow foundations.

The columns used in the bridges with rocking foundations were 2.5 m in diameter with a 3% longitudinal steel ratio, ρ_l; the fixed-base bridges had 1.8 m diameter columns with ρ_l = 2%. The pile cap of the rocking pile foundations had a volume 1.6 times that of the pile cap used in the fixed-base bridges. The columns of the bridges with rocking foundations used a pin connection between the column and the deck. In addition, the bridges with rocking foundations used 1.26 m diameter lead-plug rubber bearings at the abutments compared to 0.6 m diameter laminated rubber bearings used in the fixed-base bridges. Bridges RPF17 and RSF17 at 4% drift ratio in the transverse direction had 1.7 times the lateral strength of the fixed-base bridge. Bridges RPF8 and RSF8 at 4% drift ratio in the transverse direction had about 1.6 times the lateral strength of the fixed-base bridge. Three-dimensional nonlinear response history analyses were performed, using two components of horizontal excitation for a set of ground motions scaled to two seismic hazard levels with return periods of 975 [design earthquake (DE)] and 2475 years [maximum considered earthquake (MCE)], respectively. In one analysis case the fault-normal component of the motions was parallel to the transverse direction of the bridges (FNT case) and in the other case parallel to the longitudinal axis of the bridge (FNL case). Based on the results of the study the following conclusions are drawn:

1. The conventionally designed fixed-base bridges experienced significant inelastic deformations at both the DE and MCE levels of shaking. At the DE level of shaking the column drift ratio of bridges FB17 and FB8 was 2.81%

and 2.28%, respectively. The corresponding values at the MCE level of shaking were 4.89% and 3.60%, respectively. At the DE level of shaking the tension strain of the longitudinal reinforcement of the columns of bridges FB17 and FB8 reached 3.44% and 4.56%, respectively. The corresponding values at the MCE level of shaking were 5.30% and 6.60%, respectively. For this level of inelastic deformation, extensive spalling of the concrete and possibly extensive yielding of the transverse reinforcement and buckling of the longitudinal rebars should be expected. The residual drift ratio at the MCE level of shaking of bridges FB17 and FB8 was small and less than 0.15%. The 17 m tall fixed-base bridge experienced 0.26 m, and 0.42 m of displacement in the longitudinal direction at the DE and MCE levels of shaking, respectively. This level of displacement exceeds the 0.1 m of displacement of the expansion joints and resulted in failure of the backwall in the abutments and the approach slab. The displacements of the bearings at the abutments were 0.44 and 0.72 m at the DE and MCE levels of shaking, respectively, with the latter to possibly exceed the deformation capacity of the bearings.

2. Both the 17 m tall and 8 m tall bridges with rocking foundations resulted in nominally elastic response of the columns and the deck, while the post-tensioned strands remained elastic at both levels of shaking. Bridges RPF17 and RSF17 developed column drift ratios up to 0.83 times that of bridge FB17 in the FNT case. Bridges RPF8 and RSF8 developed drift ratios up to 1.4 times those of bridge FB8. The level of increase of nonlinear displacements for a bridge with columns on rocking foundations compared to that of a bridge designed to develop flexural plastic hinges in the columns should be expected to increase with decrease of structural period (for periods between 0.5 and 2 s). The residual column drift ratio of the bridges with rocking pile foundations was less than 0.07% and that of the bridges with rocking shallow foundations less than 0.17%. Inelastic response of the soil occurred at the ends of the rocking shallow foundations. For bridge RSF17 soil settlement reached 0.12 m, and 0.17 m (0.021 times the length of the foundation), respectively, at the DE and MCE level of shaking. The corresponding values for bridge RSF8 were 0.16 m and 0.23 m. The peak pile settlement of RPF was less than 40 mm at the MCE level of shaking. Bridges with rocking foundations developed displacements in the longitudinal direction which reached 0.49 m at the MCE level of shaking.
3. The use of two large LPRBs at each abutment of these bridges was very effective in enhancing stiffness and strength, providing hysteretic energy dissipation, and thus controlling the level of displacements these bridges experienced. Differences in the strength and stiffness of the abutments and the columns resulted in bending of the deck in the transverse direction which should be explicitly considered in the analysis and design to ensure that the deck remains nominally elastic and that the strands do not yield.
4. The bridges with rocking foundations experienced higher levels of column axial compression force increase, ΔP_c, than the fixed-base bridges. This increase is primarily due to vertical inertia effects and secondarily due to

framing effects between the columns, the deck, and the abutments. The columns on rocking pile foundations experience the highest ΔP_c. This is because sudden regain of stiffness upon contact of the pile cap to the piles excites significant vertical oscillation and vertical inertia effects. Independent of the type of design ΔP_c of the 8 m tall bridges was 2 to 2.4 times that of the corresponding 17 m tall bridges. For bridge RPF8, ΔP_c reached 1.57 and 1.80 at the DE and MCE levels of shaking, respectively. The corresponding values for axial force histories filtered at 5 Hz were 1.06 and 1.29 indicating that these axial force histories were rich in high frequencies ranging between 5 Hz and 10 Hz. The ΔP_c of the fixed-base and RSF bridges was dominated by frequencies lower than 5 Hz. This axial compression force increase should be explicitly considered in the design of the columns and the foundations.

6.2 Large scale shake-table test of bridge columns with rocking shallow foundations

The third chapter presented the response of two 460-mm-diameter columns fixed on 1.52-m-square rocking shallow foundations which were tested at the NEES@UCSD shake table. The specimens were placed inside a stiff soil confining box on top of 2.7 m of well-compacted clean sand with $D_r \approx 90\%$; the embedment depth of the foundations was 0.66 m. One specimen was aligned and the other was placed in a skewed configuration with respect to the uniaxial direction of shaking. The experimental program included three test days with different groundwater elevations and different backfill conditions around the sides of the foundations. Up to nine ground motions were used for each test day. Negligible pore pressures developed in the sand during shaking; differences in the response of the specimens between test days are solely attributed to the effect of the footing backfill conditions. Conditions considered were as follows: no ground water table with wet footing backfill soil, with 1.2 m ground water and almost dry backfill soil, and 0.6 m ground water below the foundations with weak concrete cast around the sides of the footings. The following conclusions are drawn:

1. The rocking foundations achieved response objectives very successfully. They accommodated earthquake-induced lateral displacements corresponding to drift ratios between 3.3% and 5.9% with no structural damage and minimal residual drift ratios (0.1% and 0.3%, respectively). These values of drift ratio are similar to those expected for the DE and MCE level of shaking at a near-fault site 3 km from the Hayward fault (Antonellis and Panagiotou 2014). Cosmetic structural damage developed in both columns after 18 different ground motions, 7 of which produced system drift demands greater than 10%.
2. Consistent with previous observations from centrifuge model tests (Gajan and Kutter 2008, Deng et al. 2012a), loose and dry cohesion-less backfill can fall under gaps appearing on the side of the footing during the

foundation rocking, potentially resulting in significant residual drifts. Residual drifts induced by this mechanism were small for peak drift ratios smaller than 6.9% but increased significantly for larger peak drift ratios. The residual drifts were small in Test Day 1, when the backfill soil was moist and did not slide as easily into the gap under the rocking foundation. Residual drifts were much larger on Day 2, when the backfill sand was relatively dry.

3. Casting of weak concrete around the footings for Test Day 3 was successful in minimizing material falling under the footing, which led to minimal residual drifts for peak drift ratios up to 5.9% and small residual drift ratios for peak drift ratios up to 10%. The moment capacity of the foundations backfilled with weak concrete was about 28% greater than the foundations with sand backfill, possibly due to interlocking of the footing and the weak concrete during large foundation rotations.
4. Sand falling under the foundation during the uplifting mechanism reduced settlements and enhanced energy dissipation; however, it also reduced the re-centering tendency. Sand falling under the edges of the rocking footing kept the edges of the footing in contact with the soil, which helped to maintain the rocking stiffness of embedded foundations. Without sand falling under the edges of the foundation, degradation of stiffness was apparent. The degradation of stiffness can be explained by the formation of a rounded soil-foundation interface during rocking; see Deng and Kutter (2012).
5. Vertical accelerations up to 0.75g (with 5 Hz predominant frequency) induced by the rocking mechanism were recorded in the Takatori at 100% motion that produced drift ratios more than 10%. For the Takatori at 50% motion, that produced footing rotations greater than 5%, the vertical accelerations were less than 0.3g. The cause of the vertical acceleration is the impact of the footing as the gap between the soil and footing closes during rocking. These accelerations cause a corresponding increase of the axial load of the columns, as well as oscillations in the moment resistance of the foundations.
6. The angular accelerations of the mass blocks imposed moment at the top of the columns that were up to 48% of the foundation design moment of the aligned specimen. Rotatory inertia effects in general increased with increase of peak drift ratio.

6.3 Modified modeling scheme for rocking shallow foundations

The fourth chapter presented a modified Winkler type based model for rocking foundations, based on the model proposed by Harden et al. (2009). The modified model used a uniaxial material with essentially zero tensile stiffness to properly model the foundation moment rotation behavior even under very large rotations. The main changes on the model are summarized below.

1. The length of the end zone regions are directly calculated based on the A/A_c ratios so that they are identical to the minimum contact lengths.

2. The ultimate capacity of the Winkler springs at the end zones is directly calculated based on the actual calculated soil capacity during the minimum contact area between the footing and the soil. This along with (i) ensures the accurate representation of the foundation moment capacity M_r.
3. The vertical stiffness of the springs in the end zone regions (and eventually the stiffness of the springs in the middle zone region too) are calibrated so that the secant rocking stiffness when 50% of the foundation moment, M_r, is equal to K_{init} as defined by Dent et al. (2014). The recommended value of $K_{init} = 300M_r$ provided excellent results against the large scale shake table tests.
4. The capacity and stiffness of the springs in the middle zones are artificially reduced for the cases of rocking foundations with large A/A_c ratios in order to accurately capture the settlement response. Although more research is required for providing recommendations for the Q_{ratio} and K_{ratio}, using the data from the large scale shake-table test a value of $Q_{ratio} = 2$ and $K_{ratio} = 5$ is proposed here.

Similarly to Harden et al. (2009), a uniform distribution of the damping coefficient along the width of the foundation is adopted here. The damping coefficient can be calculated for the elastic rocking case, using the secant period at the point where $0.5M_r$ is mobilized. The passive and frictional components are also modeled in a similar way with the original model. Finally, the extension to the 3D case is straightforward.

Using the modeling scheme which was summarized above, the numerical analyses of large scale shake table tests were performed for $Q_{ratio} = 2$ and $K_{ratio} = 5$ and 10. Both cases showed excellent agreement with the recorded response in terms of acceleration, foundation moment, foundation rotation, and drift ratio response. The agreement with the recorded settlements was in general good. The residual drifts were not captured correctly since this is an inherent drawback of Winkler spring models. Although the flow of sand under the uplifting side of the footing is not modeled by Winkler spring models, since rocking foundations should be detailed properly to prevent this phenomenon, there is no need for such modifications on the modeling scheme.

6.4 Three-dimensional demand model for bridge columns with rocking foundations

Finally, the fifth chapter presented the three-dimensional seismic response of 44 bridge foundation-column-mass models subject to two sets of ground motions (40 motions per set). The first set included broadband ground motions that result in mean linear spectral demands similar to those expected for a M7 earthquake event at 10 km from the fault plane. The second set included near-fault pulse-like ground motions including these with the highest peak ground velocities and spectral demands at "long" periods that have ever been recorded. The parameters investigated are the bridge column height (6.1 m < H_c < 15.2 m), the foundation width (3 m < B_f < 9.1 m), the ratio of the initial rocking stiffness to the foundation moment capacity (K_{init}/M_r), and the weight of the superstructure (W_s). The peak nonlinear displacement response and the ratio of that to the corresponding linear spectral demand (nonlinear displacement ratio) were computed, as well as the cases of overturn. The following main conclusions were drawn:

1. No overturn was caused by the broadband ground motions and only 12 cases of overturn occurred by the near-fault pulse-like ground motions (out of a total of 1760 cases). The overturns were caused by only two motions, the TCU068 and the TCU065 records by the 1999 Chi-Chi earthquake in Taiwan. All models that overturned had a rocking shear coefficient of less than 0.17.
2. The mean nonlinear displacement for the near-fault pulse-type ground motions was ranged between 13 and 34 in. The corresponding mean drift ratios were between 2.2% and 7.0%. The nonlinear displacement ratios increased rapidly for periods of less than 0.7 s and it was equal to about 2 for periods larger than 1.5 s.
3. For the broadband ground motions the mean nonlinear displacement of each model ranged between 4 and 14 in. In terms of drift ratio, the mean response was between 0.7% and 2.6%. The nonlinear displacement ratios ranged between 1.2 and 2.5 for the period range studied here. The nonlinear displacement ratios were about 1.5 for periods larger than 1.5 s.

References

Allmond, J., and Kutter, B. L. (2012). "Centrifuge testing of rocking foundations on saturated sands and unconnected piles: the fluid response." *GeoCongress*, ASCE, Reston, VA, 1760-1769.

Anastasopoulos, I., Gazetas, G., Loli, M., Apostolou, M., and Gerolymos, N. (2010). "Soil failure can be used for seismic protection of structures." *Bulletin of Earthquake Engineering*, Volume 8, 309-326.

Anastasopoulos, I., Loli, M., Georgarakos, T., and Drosos, V. (2013). "Shaking table testing or rocking-isolated bridge pier on sand." *Journal of Earthquake Engineering*, Volume 17, 1-32.

Anooshehpoor, A., Heaton, T. H., Shi, B. and Brune, J. M. (1999). "Estimates of the ground accelerations at Point Reyes station during the 1906 San Francisco earthquake." *Bulletin of the Seismological Society of America.* Volume 89(4): 845-853.

Antonellis, G., and Panagiotou, M. (2013a). "Seismic design and performance of bridges with columns on rocking foundations." Pacific Earthquake Engineering Research Center, PEER Report No. 2013/21, University of California, Berkeley, CA.

Antonellis, G., and Panagiotou, M. (2013b). "Large scale shake table tests of columns supported on rocking shallow foundations." <https://www.youtube.com/watch?v=LO9ffdJ258A>.

Antonellis, G., and Panagiotou, M. (2014). "Seismic response of bridges with rocking foundations compared to that of fixed-base bridges at a near-fault site." *Journal of Bridge Engineering*, ASCE, Volume 19(5), 04014007(2014).

Antonellis, G., Gavras, A. G., Panagiotou, M., Kutter, B. L., Guerrini, G., Sander, A., and Fox, P. J. (2015). "Shake table test of large-scale bridge columns supported on rocking shallow foundations." *Journal of Geotechnical and Geoenvironmental Engineering*, ASCE, Volume 141(5): 04015009.

Antonellis, G., Gavras, A. G., Panagiotou, M., Kutter, B. L., Sander, A., Guerrini, G., and Fox, P. J. (2014a). "Shake table test response of large-scale bridge columns supported on rocking shallow foundations." Proc 10th U.S. National Conference on Earthquake Engineering, Frontiers of Earthquake Engineering, July 21-24, Anchorage, Alaska.

Antonellis, G., Gavras, A. G., Panagiotou, M., Kutter, B. L., Guerrini, G., Sander A., Fox, P. J., Restrepo, R. I., Mahin, S. A. (2014b). "Shake-table test response of bridge columns supported on rocking shallow foundations." Department of Civil and Environmental Engineering, University of California at Berkeley, Berkeley, CA, Report No. UCB/SEMM-2014/07.

Apostolou, M., Gazetas, G., and Garini, E. (2007). "Seismic response of slender rigid structures with foundation uplift." *Soil Dynamis and Earthquake Engineering*, 27(7), 642-654.

Astaneh, A., Shen, J. and Cho, S. (1993). Seismic behavior and retrofit design of steel long span bridges.
Astaneh-Asl, H., and Roberts, J. (1996). "Seismic design, evaluation and retrofit of steel bridges." Proceedings of the 2nd US Seminar, San Francisco, USA.
Baker J.,Lin T., Shahi S., Jayaram N. (2011). "New ground motion selection procedures and selected motions for the PEER transportation research program." Pacific Earthquake Engineering Research Center, University of California, Berkeley CA.
Bartlett, P. E. (1976). *Foundation rocking on a clay soil*. Report No. 154, ME Thesis, University of Auckland, School of Engineering. Auckland, New Zealand.
Beck, J. L. and Skinner, R. I. (1974). "The seismic response of a reinforced concrete bridge pier designed to step." *Earthquake Engineering and Structural Dynamics.* Volume 2: 343-358.
Beck, J. L., and Skinner, R. I. (1974). "The seismic response of a reinforced concrete bridge pier designed to step." Earthquake Engineering and Structural Dynamics, Volume 2, 343-358.
Bolton, M. D. (1986). "The strength and dilatancy of sands." *Geotechnique,* Volume 36(1), 65-78.
Brinch Hansen, J. (1970). "A revised and extended formula for bearing capacity." *The Danish Geotechnical Institute Bulletin,* Volume 28.
California Department of Transportation (2010). Seismic Design Criteria version 1.6.
Chen, Y., Liao, W., Lee, C. and Wang, Y. (2006). "Seismic isolation of viaduct piers by means of a rocking mechanism." *Earthquake Engineering and Structural Dynamics.* Volume 35: 713-736.
Chopra, A. K. and Yim S. C. (1985). "Simplified earthquake analysis of structures with foundation uplift." *Journal of Structural Engineering.* Volume 111(4): 906-930.
Clough, R. W. and Huckelbridge, A. A. (1977). *Preliminary experimental study of seismic uplift of a steel frame.* Report No. UCB/EERC-77/22, Berkeley, CA.
Cormarck, L. G. (1988). "The design and construction of the major bridges on Mangaweka rail deviation." The Institution of Professional Engineers of New Zealand, Volume 15(1).
Cremer, C., Pecker, A. and Davenne, L. (2001). "Cyclic macro-element for soil-structure interaction: material and geometrical non-linearities." *International Journal for Numerical and Analytical Methods in Geomechanics.* Volume 25: 1257-1284.
Cremer, C., Pecker, A. and Davenne, L. (2002). "Modeling of nonlinear dynamic behavior of a shallow strip foundation with a macro-element." *Journal of Earthquake Engineering.* Volume 6(2): 175-211.
Deng, L., and Kutter, B. L. (2012). "Characterization of rocking shallow foundations using centrifuge model tests." *Earthquake Engineering and Structural Dynamics*, Volume 41, 1043-1060.
Deng, L., Kutter, B. L., and Kunnath, S. K. (2012a). "Centrifuge modeling of bridge systems designed for rocking foundations." *Journal of Geotechnical and Geoenvironmental Engineering*, Volume 138(3), 335-344.
Deng, L., Kutter, B. L., and Kunnath, S. K. (2012b). "Probabilistic seismic performance of rocking-foundation and hinging-column bridges." *Earthquake Spectra,* Volume 28(4), 1423-1446.

Deng, L., Kutter, B. L., and Kunnath, S. K. (2014). "Seismic design of rocking shallow foundations: displacement-based methodology." *Journal of Bridge Engineering*, ASCE, 10.1061(ASCE)/BE.1943-5592.0000616.
Dimitrakopoulos, E. G., and Giouvanidis, A. I. (2015). "Seismic response analysis of the planar rocking frame." *Journal of Engineering Mechanics*, ASCE, DOI: 10.1061/(ASCE)EM.1943-7889.0000939.
Dimitrakopoulos, E. G., and Paraskeva, T. S. (2015). "Dimensionless fragility curves for rocking response to near-fault excitations." *Earthquake Engineering and Structural Dynamics*, DOI:10.1002/eqe.2571.
Dowdell, D. J. and Hamersley, B. A. (2000). "Lion's gate bridge north approach – Seismic retrofit."
Espinoza, A., and Mahin, S. A. (2008). "Shaking table and analytical investigation of reinforced concrete bridge piers with foundations allowed to uplift during earthquakes." Report No. UCB/SEMM-08/03, Department of Civil and Environmental Engieering, University of California, Berkeley.
Faccioli, E., Paolucci, R. and Vivero, G. (2001). "Investigation of seismic soil-footing interaction by large scale cyclic tests and analytical models." In *Proc., 4th International Conference Recent Advances in Geotechnical Earthquake Engineering and Soil Dynamics. Special Presentation Lecture.* Paper No. SPL-05, March 26-31, San Diego, CA.
Fleming, K., Weltman, A., Randolph, M., and Elson, K. (2009). "Piling Engineering." third edition.
Fox, P. J., Sander, A. C., Elgamal, A., Greco, P., Isaacs, D., Stone, M., and Wong, S. (2014). "Large soil confinement box for seismic performance testing of geo-structures." *Geotechnical Testing Journal*, in press.
Gajan, S., and Kutter, B. L. (2008). "Capacity, settlement and energy dissipation of shallow footings subjected to rocking." *Journal of Geotechnical and Geoenvironmental Engineering*, Volume 134(8), 1129-1141.
Gajan, S., and Kutter, B. L. (2009). "Effects of moment-to-shear ratio on combined cyclic load-displacement behavior of shallow foundations from centrifuge experiments." *Journal of Geotechnical and Geoenvironmental Engineering*, Volume 135(8), 1044-1055.
Gajan, S., Hutchinson, T., Kutter, B. L., Raychowdhurry, P., Ugalde, J. A., Stewart, J. P. (2008). "Numerical models for analysis and performance-based design of shallow foundations subjected to seismic loading." Report No. 2007/04, University of California Berkeley, Pacific Earthquake Engineering Research Center, Berkeley, CA.
Gajan, S., Kutter, B. L., Phalen, J. D., Hutchinson, T.C., and Martin, G.R. (2005). "Centrifuge modeling of load-deformation behavior of rocking shallow foundations." Soil Dynamics and Earthquake Engineering, Volume 25, 773-783.
Gazetas, G. (1983). "Analysis of machine foundation vibrations: state of the art." *Soil Dynamics and Earthquake Engineering.*Volume 2(1): 2-42.
Gelagoti, F., Kourkoulis, R., Anastasopoulos, I., and Gazetas, G. (2012). "Rocking isolation of low-rise frame structures founded on isolation footings." *Earthquake Engineering and Structural Dynamics*, Volume 41, 1177-1197.
Georgiadis, M. and Butterfield, R. (1988). "Displacement of footings on sand under eccentric and inclined loads." *Canadian Geotechnical Journal.* Volume 25: 199-212.

Harden, C., and Hutchinson, T. (2009). "Beam-on-nonlinear-winkler-foundation modeling of shallow rocking-dominated footings." Earthquake Spectra, Volume 25(2), 277-300.
Highter, W. H., and Anders, J. C. (1985). "Dimensioning footings subjected to eccentric loads." *Journal of Geotechnical Engineering*, Volume 111(5), 659-665.
Housner, G. H. (1963). "The behavior of inverted pendulum structures during earthquakes." *Bulletin of the Seismological Society of America.* Volume 53(2): 403-417.
http://www.opensha.org/glossary-attenuationRelation-BOORE_ATKIN_2008
Ingham, T. J., Rodriguez, S., Nader, M. and Taucer, F. (1995). "Seismic retrofit of the golden gate bridge." In *Proc., 11th World Conference on Earthquake Engineering.* Paper No. 1396.
Ishiyama, Y. (1983). "Motions of rigid bodies and criteria for overturning by earthquake excitations." *Earthquake Engineering and Structural Dynamics.* Volume 10: 635-650.
Jeong, H. I., Sakai, J., and Mahin, S. A. (2008). "Shaking table tests and numerical investigation of self-centering reinforced concrete bridge columns." Pacific Earthquake Engineering Research Center, PEER Report No. 2008/6, Berkeley, CA.
Jones, M. H., Holloway, L. J., Toan, V. and Hinman, J. (1997). "Seismic retrofit of the 1927 carquinez bridge by a displacement capacity approach." In *Proc., 2nd National Seismic Conference on Bridges and Highways.* p. 445-456, Sacramento, CA.
Kelly, J. M., and Tsztoo, D. F. (1977). "Earthquake simulation testing of a stepping frame with energy-absorbing devices." University of California at Berkeley, Report No. UCB/EERC-77/17.
Kirkpatrick, P. (1927). "Seismic measurements by the overthrow of columns." *Bulletin of the Seismological Society of America.* Volume 17: 95-109.
Konstantinidis, D., and Makris, N. (2009). "Experimental and analytical studies on the response of freestanding laboratory equipment to earthquake shaking." *Earthquake Engineering and Structural Dynamics*, Volume 38: 827-848.
Kutter, B. L., Martin, G. R., Hutchinson, T., Harden, C., Gajan, S. and Phalen, J. (2006). *Workshop on modeling of nonlinear cyclic load-deformation behavior of shallow foundations.* Report No. 2005/14, University of California Berkeley, Pacific Earthquake Engineering Research Center, Berkeley, CA.
Loli, M., Knappett, J. A., Brown, M. J., Anastasopoulos, I., and Gazetas, G. (2014). "Centrifuge modeling of rocking-isolated RC bridge piers." *Journal of Earthquake Engineering and Structural Dynamics* (in press).
Lu, Y., and Panagiotou, M. (2014). "Characterization and representation of near-fault ground motions using cumulative pulse extraction with wavelet analysis." *Bulletin of the Seismological Society of America*, Volume 104: 410-426.
Makris, N. (2014). "The role of the rotational inertia on the seismic resistance of free-standing rocking columns and articulated frames." *Bulletin of the Seismological Society of America,* Volume 104(5): 2226-2239.
Makris, N. and Konstantinidis, D. (2003). "The rocking spectrum and the limitations of practical design methodologies." *Earthquake Engineering and Structural Dynamics.* Volume 32: 265-289.
Makris, N. and Roussos, Y. S. (2000). "Rocking response of rigid motions under near-source ground motions." *Géotechnique.* Volume 50(3): 243-262.

Makris, N. and Zhang, J. (2001). "Rocking response of free-standing blocks under cycloidal pulses." *Journal of Engineering Mechanics.* Volume 127(5): 473-483.
Makris, N., and Vasileiou, M. F. (2014). "Are some top-heavy structures more stable?" *Journal of Structural Engineering,* Volume140 (5): 06014001.
Meek, J. W. (1978). "Dynamics response of tipping core buildings." *Earthquake Engineering and Structural Dynamics.* Volume 6: 437-454.
Mergos, P. E., Kawashima, K. (2005). "Rocking isolation of a typical bridge pier on spread foundation." *Journal of Earthquake Engineering.* Volume 9(2): 395-414.
Meyerhof, G. G. (1963). "Some recent research on the bearing capacity of foundations." *Canadian Geotechnical Journal*, Volume 1, 16-26.
Milne, J. and Omori, F. (1893). "On the overturning and fracturing of brick columns by horizontal applied motion." *Seismological Journal of Japan*. Volume 17: 59-86.
Muto, K., Takahasi, R., Aida, I., Ando, N., Hisada, T., Nakagawa, K., Omemura, H. and Osawa, Y. (1960). "Nonlinear response analyzers and application to earthquake resistant design." In *Proc., 2nd World Conference on Earthquake Engineering.*Japan, Volume 2: 649-668.
Negro, P., Paolucci, R., Pedretti, S., and Faccioli, E. (2000). "Large scale soil-structure interaction experiments on sand under cyclic loading." Proc. 12th World Conference on Earthquake Engineering, Auckland, New Zealand.
OpenSees (2012). <http://opensees.berkeley.edu/>
Paolucci, R., di Prisco, C., Vecchiotti, M., Shirato, M. and Yilmaz, M. T. (2007). "Seismic behaviour of shallow foundations: large scale experiments vs. numerical modelling and implications for performance based design." In *Proc., 1st US-Italy Seismic Bridge Workshop, Pavia, Italy, April 19-20.*
Paolucci, R., Shirato, M., and Yilmaz, M. T. (2008). "Seismic behavior of shallow foundations: shaking table experiments vs numerical modeling." *Earthquake Engineering and Structural Dynamics*, 37, 577-595.
Pecker, A. (2006). "Enhanced seismic design of shallow foundations: example of the Rion-Antirion bridge." *4th Athenian Lecture on Geotechnical Engineering*, Hellenic Society of Soil Mechanics and Geotechnical Engineering, Athens, Greece.
Pecker, A. and Pender, M. J. (2000). "Earthquake resistant design of foundations: new construction."
Phan, V., Saiidi, M., Anderson, J., and Ghasemi, H (2007). "Near fault ground motion effect on reinforced concrete bridge columns." *Journal of Bridge Engineering*, ASCE, Volume 133(7), 982-989.
Pollino, M., and Bruneau, M. (2007). "Seismic retrofit of bridge steel truss piers using a controlled rocking approach." Journal of Bridge Engineering, ASCE, Volume 12(5), 600-610.
Priestley, M. J. N., Evison, R. J. and Carr, A. J. (1978). "Seismic response of structures free to rock on their foundations." *Bulletin of the New Zealand National Society for Earthquake Engineering.* Volume 11(3): 141-150.
Priestley, M. J. N., Seible, F., and Calvi, G. M. (1996). "Seismic design and retrofit of bridges."
Psycharis, I. N. and Jennings, P. C. (1983). Rocking of slender rigid bodies allowed to uplift. *Earthquake Engineering and Structural Dynamics.* Volume 11: 57-76.

Rutenberg, A., Jennings, P. C. and Housner, G. H. (1982). "The response of veterans hospital building 41 in the San Fernando earthquake." *Earthquake Engineering and Structural Dynamics.* Volume 10: 359-379.
Saiidi, M., Gopalakrishnan, B., Siddharthan, R. (2002). "Shake table studies of effects of foundation flexibility on seismic demand in substandard bridge piers." *ACI 5fth International Conference, Special Publication,* American Concrete Institute, Detroit, 553-569.
Sakellaraki, D., and Kawashima, K. (2006). "Effectiveness of seismic rocking isolation of bridges based on shake table test." *First European Conference on Earthquake Engineering and Seismology*, Paper No. 364, Geneva, Switzerland.
Salgado, R. (2008). "The engineering of foundations." *Mc-Graw-Hill Companies, Inc.*, New York, NY, 413-439.
Sander A.C., Fox, P. J., and Elgamal, A. (2014). "Full-scale seismic test of MSE retaining wall at UCSD" American Society of Civil Engineers, *Proceedings: Geo-Congress (ASCE)*, Atlanta, GA.
Schoettler M. J., Restrepo, J. I., Guerrini, G., Duck, D. E., and Carrea, F. (2012). "A full-scale single-column bridge bent tested by shake-table excitation." http://nees.org/resources/6868, University of Nevada, Center for Civil Engineering Earthquake Research, Department of Civil Engineering.
Shi, B., Anooshehpoor, A., Zeng, Y. and Brune, J. (1996). "Rocking and overturning of precariously balanced rocks by earthquakes." *Bulletin of the Seismological Society of America.* Volume 86(5): 1364-1371.
Shirato, M., Kouno, T., Asai, R., Nakani, N., Fukui, J., and Paolucci, R. (2008). "Large-scale experiments on nonlinear behavior of shallow foundations subjected to strong earthquakes." *Soils and Foundations*, Volume 48(5), 673-692.
Spanos, P. D. and Koh, A. (1984). "Rocking of rigid blocks due to harmonic shaking." *Journal of Engineering Mechanics.* Volume 110(11): 1627-1642.
Tso, W. K. and Wong, C. M. (1989). "Steady state rocking response of rigid blocks part 1: analysis." *Earthquake Engineering and Structural Dynamics.* Volume 18: 89-106.
Ugalde, J. A., Kutter, B. L., Jeremić, B. (2010). "*Rocking response of bridges on shallow foundations.*" Report No. 2010/101, University of California Berkeley, Pacific Earthquake Engineering Research Center, Berkeley, CA.
Veletzos, M., and Restrepo, J. I. (2011). "Development of seismic design quidelines for segmental construction." University of California at San Diego, La Jolla, CA, Report no. SSRP-10/02,357-384.
Vesic, A. S. (1973). "Analysis of ultimate loads of shallow foundations." *Journal of the Soil Mechanics and Foundations Division*, Volume 99(SM1), 45-73.
Wiebe, L. and Christopoulos, C. (2010). "Characterizing acceleration spikes due to stiffness changes in nonlinear systems." *Earthquake Engineering and Structural Dynamics*, Volume 39: 1653-1670.
Wiesing, P. R. (1979). "*Foundation rocking on sand*." Report No. 203, ME Thesis, University of Auckland, School of Engineering. Auckland, New Zealand.
Wolf, J.P. (1976). "Soil-structure interaction with separation of base mat from soil (lifting-off)." *Nuclear Engineering and Design*, Volume 38, 357-384.